Analysis of Magnetohydrodynamic (MHD) Activity Using Electron Cyclotron Emission (ECE) Diagnostics on Alcator C-Mod Tokamak

by
Yongkyoon In
B.S., Nuclear Engineering, Seoul National University, Korea (1990)
M.S., Nuclear Engineering, Seoul National University, Korea (1995)

Submitted to the Nuclear Engineering Department
in partial fulfillment of the requirements for the degree of
Doctor of Philosophy in Applied Plasma Physics
at the
MASSACHUSETTS INSTITUTE OF TECHNOLOGY
July 2000

Author .....
.....
Nuclear Engineering Department
July 6, 2000

Certified by.....
.....
Ian H. Hutchinson
Professor, Nuclear Engineering Department
Thesis Supervisor

Certified by.....
.....
Amanda E. Hubbard
Research Scientist, Plasma Science and Fusion Center
Thesis Supervisor

Certified by.....
.....
Jeffrey P. Freidberg
Professor, Nuclear Engineering Department
Thesis Reader

Accepted by .....
Professor Sow-Hsin Chen
Chairman, Department Committee on Graduate Students

Analysis of Magnetohydrodynamic (MHD) Activity Using Electron Cyclotron Emission (ECE) Diagnostics on Alcator C-Mod Tokamak

by

Yongkyoon In

Submitted to the Nuclear Engineering Department
on July 6, 2000, in partial fulfillment of the
requirements for the degree of
Doctor of Philosophy in Applied Plasma Physics

Abstract

Magnetohydrodynamic (MHD) activity has been analyzed primarily using electron cyclotron emission (ECE) diagnostics on Alcator C-Mod tokamak. The main results are that i) two MHD instabilities have been identified during current ramp-up discharges (resistive 'multiple' tearing mode and ideal interchange mode) and ii) a new approach to diagnose edge localized modes (ELMs) using ECE diagnostics was explored. Both MHD modes were accompanied by hollow pressure and current profiles. The associated q-profiles were also hollow with $q_0 \gg 1$, where q_0 is the safety factor on the magnetic axis. In both cases, the electron temperature fluctuations observed on ECE diagnostics agreed reasonably well with the perturbed pressure fluctuations predicted in a resistive linear stability code (MARS). For the resistive 'multiple' tearing mode, the MHD fluctuations were peaked near the outer q=3 rational surface but had several other resonant layers, which affected the plasma globally. The predicted growth time was ~0.44 msec, which is within the typical range of tearing mode evolution times. For the ideal interchange mode, the MHD fluctuations were highly localized near the inner q=5 rational surface. According to ideal MHD stability theory, the $q = 5$ surface was found to be ideally unstable because of the reversed pressure gradient ($dp/dr > 0$) and $q > 1$ with moderate shear. When kinetic effects were added, the ideally unstable mode was finite ion Larmor radius (FLR) stabilized. However, considering that 1) electrons are collisional, 2) ions are collisionless, and 3) the thermal ion transit frequency is comparable to the ion diamagnetic drift frequency, ion Landau damping was found to be strong enough to drive a kinetic Mercier instability. As a result, a FLR modified kinetic Mercier instability has been identified, possibly for the first time since the Mercier criterion was formulated forty years ago.

During 'Type III' ELMs, rather unusual signal changes were observed on two ECE diagnostics; signal drops of second harmonic X-mode on one diagnostic and signal spikes of fundamental harmonic O-mode on another. These were explained in

terms of refraction effects and found to be useful to infer the associated geometrical dimensions. For this investigation, a new ray tracing code, which can accommodate poloidal variations, has been developed. As a result, an ELM has been modeled successfully as a poloidally elongated density loss. Observations are consistent with the following dimensions; radial width of the affected region (Δr) $\sim$ 1 - 3 cm, poloidal elongation $\sim$1.5 (equivalent to a poloidal wave number k_θ= 2.1 rad cm^{-1}), minimum density $0.5\times10^{20}m^{-3}$ at the midplane $\approx$1cm inside the last closed flux surface (LCFS). This knowledge helps to assess the influence of the particle loss on the main plasma. Considering that ELMs challenge present diagnostic capabilities in terms of spatiotemporal resolution, such indirect measurement opens the door to improved physical understanding of ELMs. In particular, it is the first to reveal the poloidal structure of an ELM.

Thesis Supervisor: Ian H. Hutchinson
Title: Professor, Nuclear Engineering Department

Thesis Supervisor: Amanda E. Hubbard
Title: Research Scientist, Plasma Science and Fusion Center

To three graduate students in Korea who passed away in 1999
without tasting their academic goals
during an unexpected accident in the SNU laboratory
where I started to learn of plasma physics

Acknowledgments

Trust in the Lord with all your heart and lean not on your own understanding; in all your ways acknowledge him and he will make your paths straight.
(Proverbs 3:5-6)

Without giving thanks to God, I cannot say a word to express my gratitude to all the good people I have met because I believe He introduced them to me. Five years ago, when I arrived in Boston, I knew few people. However, through His help, I have met numerous helpers until I am now about to graduate. In particular, I would like to thank God for meeting Amanda Hubbard, who has been my friendly advisor since I started working in C-Mod project in late 1995. I am very thankful to her for encouraging me to see important things as an experimentalist and reading my clumsy manuscripts carefully without a complaint. Not only officially but also personally she has been supportive to me all the time. I want to thank Professor Ian Hutchinson for helping me to navigate the realm of 'plasma physics', by exercising his exceptional physical intuition and understanding quite often. Especially, the limitations regarding refraction effects in Chapter 6 became vivid to me through his critiques. For the MHD stability calculations in Chapter 4 and 5, I would like to express special gratitude to Jesus Ramos. He helped me to not only get the stability results by running the MARS code but also appreciate the 'beauty and beast' of the MHD theory. When it comes to the kinetic theory in Chapter 5, I would not have imagined including the theoretical works in my thesis without meeting Jim Hastie. Jim has been a wonderful mentor for guiding me to comprehend theoretical plasma physics easily, as well as for providing kinetic theory supports. I included his quasi 1-D calculation results in order to compare the MARS predictions and obtained the numerical results related to ion Landau damping in collaboration with him. In addition, I thank Professor Freidberg for encouraging me to see a big picture for years and reading my thesis.

I have earned great help from Steve Wolfe, who taught me how to run the EFIT

program and gave me sharp but constructive comments. I wish to thank Earl Marmar for helping me find the density profiles from visible bremsstrahlung, Martin Greenwald for useful discussion regarding ELMs, Joe Snipes for helping me to construct a mode number analysis program, Jim Irby for running inversion programs of some current ramp-up cases, John Rice for answering the questions about toroidal rotation, Brian LaBombard for comments about the paritcle loss estimation during Type III ELMs, Gary Taylor for providing me with GPC2 data, Arnold Kritz and Paul Bonoli for helping me to resuscitate the TORAY code in VAX environment and Professor Miklos Porkolab for encouraging me to pursue MHD studies of reversed shear plasmas. In addition, I am very grateful to Rejean Boivin for generously allowing me to use CHARGE almost exclusively, which enabled me to get ray tracing results faster than what they would have taken otherwise. For core MHD activity which I had in mind in the past but did not include in this thesis, Catherine and Rejean helped me to keep track of such interesting MHD activity. For the maintenance of ECE diagnostics, I wish to thank Frank Shefton who has provided technical supports all the time. From a prayer meeting organized by Rick Murray, I had privilege of praying together with Sam Pierson and Andy Pfeiffer during lunch hours almost once a week.

Although Professor Kiehyung Chung, who is a 'father' of experimental plasma physics in my motherland (Korea), did not give me direct help for this thesis, he has been a role model as a scholar. In particular, the remembrance of his passion for research and education was a momentum to me to be diligent in my studies.

From all the C-Mod graduate students and staffs, I have earned great help mentally and physically from time to time. Especially, I enjoyed the conversations with Peter O'shea, Rob Nachtrieb, Sanjay Gangadhara, Yijun Lin, Maxim Umansky, Taekyun Chung, Alex Mazurenko, Chris Boswell, Thomas Sunn Pedersen, Antonio Bruno, Dimitrios Pappas, Eric Nelson-Melby, Peter Catto, John Heard, Ned Eisner and Romik Chatterjee. In addition, I would like to thank all my Christian friends in First Korean Church in Cambridge for praying together and praising the Lord every week.

Since my parents, Choonmu and Hainam, have prayed for me all the time, I believe

I have been guided by the Lord. With the help of my three brothers, Byunghyun, Daekyun and Byungha, I understood the concept of being together within love, as the Bible tells me. I am also grateful to my families-in-law (Youngkeum, Kilsaeng and Sungja, Sookyung, Iljoo and Soyoung) for cheering me up occasionally. My little daughter, Grace Misong In, has been a wonderful entertainer for her Daddy.

Finally, I could never have finished this thesis without knowing that my wife, Heekyung, was always praying for me with her love.

Contents

1 Introduction **29**

1.1 Fusion 29

1.2 Alcator C-Mod 30

1.2.1 Heating Schemes 32

1.2.2 ECE diagnostics 32

1.2.3 Other diagnostics 33

1.3 Scope of the thesis 33

1.3.1 MHD activity in tokamaks 33

1.3.2 Outline of the thesis 35

2 ECE Diagnostics **37**

2.1 ECE principles 37

2.1.1 Radiation from gyrating charged particles 39

2.1.2 Plasma waves in magnetized plasmas 40

2.1.3 Propagation in the optically thick plasma 44

2.1.4 Temperature measurement using ECE in tokamaks 45

2.2 ECE diagnostics in Alcator C-Mod 48

2.2.1 Michelson Interferometer 49

2.2.2 Radiometers 51

2.2.3 Grating Polychromators 51

3 Magnetohydrodynamics (MHD) theory **55**

3.1 Ideal MHD 56

3.1.1 Equilibrium . . . 57
3.1.2 Stability . . . 60
3.2 Resistive instability . . . 65

4 Resistive modes during current ramp discharges **67**
4.1 MHD activity during current ramp-up . . . 68
4.1.1 Types of MHD activity observed during current ramp-up . . . 70
4.1.2 Kinetic EFIT and ECE positions during current ramp . . . 74
4.2 Resistive "multiple" tearing mode in reversed shear plasmas . . . 77
4.2.1 Experimental Observation . . . 78
4.2.2 Stability and interpretation . . . 83
4.3 Resistive interchange mode . . . 90
4.3.1 Characteristics of resistive interchange modes . . . 92

5 Identification of Mercier instabilities **95**
5.1 Introduction . . . 95
5.2 Observation of localized MHD fluctuations . . . 97
5.3 Theoretical interpretation . . . 105
5.3.1 Equilibrium . . . 105
5.3.2 MHD stability theory . . . 105
5.3.3 The effect of finite ion Larmor radius (FLR) stabilization . . . 113
5.3.4 Kinetic theory of Mercier modes and the effect of ion Landau damping . . . 115
5.3.5 Frequency comparison . . . 116
5.4 Discussion and Conclusions . . . 119

6 Edge localized modes (ELMs) and their inferred geometrical dimensions **121**
6.1 Edge localized modes (ELMs) . . . 123
6.1.1 Classifications . . . 123
6.1.2 ELMs in Alcator C-Mod . . . 125

6.2 Refraction effects during ELMs 130
6.2.1 Ray tracing code 130
6.2.2 Refracted ray trajectories 134
6.3 Inferred dimensions 155
6.3.1 Interpretation of signal changes 164
6.3.2 Comparison with theoretical predictions 167
6.4 Results and discussion 168

7 Conclusions and future work **171**

List of Figures

1.1 Alcator C-Mod cross section with typical magnetic flux surfaces. The surface of the in-vessel is covered with molybdenum tiles, unlike in other tokamaks whose in-vessel surfaces are usually covered with reinforced carbon graphite tiles. 31

2.1 Gyrating electron (ion) trajectory drifting along magnetic field (**B**) . 38

2.2 ECE harmonics, cutoffs and resonance frequencies 43

2.3 Optical depth surface and contour plots. Assuming R=0.89 m and $2\Omega/2\pi$=226 GHz (i.e. the outermost channel of GPC (Ch 9)), the density and temperature can become so low that the optical depth could be in the 'optically grey' region for both L and H modes. In this case, the analysis based on an optically thick plasma tends to underestimate the electron temperature. 47

2.4 ECE Diagnostics in Alcator C-Mod 50

2.5 Electron temperature profiles from Michelson interferometer, GPC, GPC2 and Thomson Scattering diagnostics. Since the first three diagnostics are cross-calibrated, such good agreement is typical. The Thomson scattering data was closest available to the above time, but it was taken 18 msec earlier. Overall, the electron temperatures show good agreement among the four diagnostics. 53

3.1 Orthogonal(R, ϕ, z) and non-orthogonal(ψ, θ, ϕ) coordinate definitions in toroidal geometry. Toroidal angle ϕ rotates in the counterclockwise direction from the top (i.e. into the paper). Using the right-handedness convention, poloidal angle θ rotates in the clockwise direction in the poloidal cross section (ie. downward arrow on the paper). Often, the directions of both the ϕ and θ coordinates are reversed without loss of generality. 58

4.1 Top: MHD occurrences vs current ramp-up rate ($\Delta I_p/\Delta t$). Region A (low $\Delta I_p/\Delta t$) and Region C (high $\Delta I_p/\Delta t$) are equally stable (i.e. no MHD dominated). In Region B (moderate $\Delta I_p/\Delta t$), it seems to be fair to say that lower $\Delta I_p/\Delta t$ ($\leq$ 5.1 MA/s) is slightly more unstable than higher $\Delta I_p/\Delta t$. Overall, faster current ramp-up rates did not show any tendency to lead to more frequent MHD occurrences. Bottom: Percentage of MHD occurrences vs current ramp-up rate. 69

4.2 Typical current ramp discharge without MHD activity. The T_e profile is monotonic at all times. 71

4.3 Classifications of various MHD events during current ramp discharge. Note that there is no more MHD after 180 msec, when T_e profile becomes monotonic. During the global MHD, the signal looks "sawtooth-like", but there are no inverted sawtooth-like signals on edge channels. In fact, the plasma was nearly terminated. 72

4.4 Electron temperature (T_e) profiles based on Figure 4.3. 73

4.5 Components for total magnetic field changes 75

4.6 GPC position differences of kinetic ($*$) and routine ($\diamond$) EFITs. In this example, an equilibrium with hollow q-profile has been reconstructed using kinetic EFIT, on which each channel ($*$) of GPC has been located. Hence, the locations ($\diamond$) based on routine EFIT (with monotonic q-profile ($q_0 \sim 1$)) might have been miscalculated. Especially, such shifts as 3$\sim$8 mm for some inner channels are not insignificant. 76

4.7 MHD activity during reversed magnetic shear plasma. Note that the electron temperatures of the two innermost channels are lower than the third channel (i.e. a hollow temperature profile). 79

4.8 Toroidal mode number determination for resistive multiple tearing mode: n=1. 80

4.9 Enlarged view of the MHD activity observed on GPC and magnetics of Fig. 4.7 near t=108 msec. In particular, observe that the T_e fluctuations on Channel 6 are the biggest and that the oscillation frequency ($3 \sim 4$ kHz) is the same as that of the magnetics. 81

4.10 At t=0.108 sec considered here, Channel 6, which is located at R=80 $\sim$ 81 cm ($\rho \sim 0.62$), shows the biggest fluctuations. Also, note that the fluctuations of Channel 6 evolve, peak near t=0.11 sec and then the biggest fluctuations move outward into Channel 7 ($\rho \sim 0.72$) at t=0.120 sec. 82

4.11 Pressure profiles: Solid curve - from EFIT reconstruction; Dashed curve - calculated from T_e of GPC and n_e inferred from visible Bremsstrahlung; Dash-dot curve - 2 $\times(n_e T_e)$, based on T_e of GPC and n_e from TCI-inversion using routinely calculated EFIT reconstruction. 84

4.12 q-profile at t=108 msec. Note that the outer q=3 rational surface is located at R$\sim$ 83.5 cm ($\rho \sim 0.73$), which is close to $(\Delta T)_{max}$. 85

4.13 n=1 resistive "multiple" tearing mode. Note that resonant layers are observed not only at the outer $q = 3$ surface, but also at the inner $q = 3$ and at the $q = 4$ rational surfaces, which characterizes the "multiple" tearing mode. For the solid thick q-profile curve, $S_0 = 1.67\times10^7, \gamma\tau_A \sim 1.8 \times 10^{-4}$, where γ is the growth rate $[sec^{-1}]$ and τ_A is Alfvén time $\sim 8 \times 10^{-8}$ sec. When all the components are summed up, the total predicted pressure fluctuations (δp) are delineated with the dash-dot curve. This can be compared with the temperature fluctuations (ΔT_e) at t=0.108 sec. Theory and experiment results match each other. The other two cases, whose q-profiles are shown in thick short and long dashed curves respectively, also predicted almost the same fluctuations. 86

4.14 Sensitivity of the reconstructed equilibrium in terms of q_0. Near q_0=4.4 is the most likely, whose q-profile corresponds to the thick solid curve of Figure 4.13. Region I invokes typical sawteeth, whose q_0 is ≤ 1, while Region II is more likely to occur during the current ramp-up discharge without sawteeth. 88

4.15 Perturbed radial magnetic flux defined as $\Delta b \equiv \frac{d\Phi}{d\theta d\phi} = [\nabla\psi \cdot (\nabla\theta \times \nabla\phi)]^{-1}\tilde{\mathbf{B}}\cdot\nabla\psi$. The sum of the Fourier components giving the perturbed magnetic flux at θ =0 is delineated with the dash-dot curve. 89

4.16 n=1 resistive interchange mode. Near the inner q=4 inner rational surface, the fluctuations are highly localized. Each symbol represents a poloidal mode component. The dash dot curve shows the predicted total pressure fluctuations (δp). With $S_0 = 1.67\times10^7, \gamma\tau_A \sim 4.9\times10^{-4}$, where γ is the growth rate$[sec^{-1}]$, τ_A is Alfvén time $\sim 8 \times 10^{-8}$ sec. . 91

4.17 Growth rates vs resistivity. The Alcator C-Mod case is encircled. Although the resistive interchange mode was not observed in experiments, it has been predicted to be unstable. The dashed and solid lines are the theoretical growth rates of the resistive interchange and multiple tearing mode respectively. As resistive interchange mode theory predicts, the growth rate is proportional to $\eta^{1/3} \propto S_0^{-1/3}$. The resistive multiple tearing mode evolves in proportion to $\eta^{3/5} \propto S_0^{-3/5}$, which similarly agrees with the theoretical prediction for resistive single tearing modes. 93

5.1 MHD activity during current ramp discharge. Near t=115 msec, highly localized MHD fluctuations are observed on the second channel and then sawtooth-like crashes follow later. 98

5.2 Highly localized MHD on the innermost four GPC channels. Note that the MHD is extraordinarily localized on the second channel and that the temperature profile was hollow; near t=115 msec, T_e(Ch 1)=0.61 $< T_e$(Ch 2)= 0.77 $< T_e$(Ch 3)=0.88 $> T_e$(Ch 4)=0.78 in keV units. See also the electron temperature profile in Figure 5.6. Each shaded area represents the time bin for comparison with magnetics; 'before', 'during' and 'after' this fluctuation. 99

5.3 Fourier-transformed fluctuation amplitudes at $\sim$ 3 kHz of the combined dataset of GPC and GPC2. The amplitudes are normalized with respect to the maximum Fourier-transformed GPC fluctuation amplitude. The amplitudes during the localized MHD are significantly above those before and after the event. Later, comparison with the MARS results will show that the fluctuations were due to an ideal interchange mode. 100

5.4 Fourier-transformed magnetic signals before, during and after the localized MHD. The coherent frequency near 3.2 kHz is dominant during the event. These time bins are as defined in Figure 5.2. 101

5.5 Toroidal mode number determination. In the 1999 run campaign, the magnetics were upgraded. From the new fast magnetics, the toroidal mode number was clearly identified as $n = 1$. In the lab frame, it was found to be rotating in the ion diamagnetic direction. 103

5.6 Electron temperature (T_e), density (n_e), pressure (p_e) and total pressure ($p = p_i + p_e$) profiles. Note that electron temperature is hollow, while the density is weakly decreasing. In addition, the total pressure is also hollow. Each circle represents one of the combined locations of GPC and GPC2. The dashed rectangle represents the location of the localized MHD activity from the combined data set. 104

5.7 Safety factor and pressure profiles. The asterisks ($*$) represent pressures as input to EFIT reconstruction, while the solid curve is the EFIT output. Note the inner $q = 5$ surface is located in the inverted pressure gradient region ($dp/dr > 0$). 106

5.8 Sensitivity of the reconstructed equilibrium in terms of q_0. Near q_0=5.5 was the only error-free zone. The lower q_0 zone showed an error related to $\beta_p + l_i$, while the higher q_0 zone had an error related to β_p. Here, β_p is the poloidal β and l_i is the internal inductance of the plasma. In the lower q_0 zone with the error, a 'triple hump' current density profile has been reconstructed, which is very unlikely. 107

5.9 Growth rates vs resistivity using the MARS code. The Alcator C-Mod case is circled. As the resistivity decreases, the growth rates become independent of it, which is characteristic of an ideal MHD mode. The dashed and solid lines are the theoretical growth rates of the resistive interchange and multiple tearing mode respectively. Thus, the ideal interchange mode was predicted to have higher growth rate than the multiple tearing mode. 108

5.10 $n = 1$ ideal interchange mode. Near the inner $q = 5$ rational surface, the fluctuations are highly localized. Each symbol represents a poloidal mode component. The dash-dot curve delineates the predicted total pressure fluctuations (δp). With $S_0 = 1.25 \times 10^7, \gamma_{cmod}\tau_A \sim 1.2 \times 10^{-3}$, where γ is the growth rate$[sec^{-1}]$ and τ_A is the Alfvén time $\sim 8 \times 10^{-8}$ sec. 110

5.11 When a hollow pressure profile exists in the core, the good and bad curvatures are reversed relative to the normal (monotonically decreasing) pressure profile. The thick curves represent conventionally good curvature regions on the flux averaged surfaces for $(q^2 - 1) > 0$. . . . 111

5.12 Eigenfunction based on a quasi 1-D model. The comparison with Figure 5.10 reveals the quasi 1-D model applicability. 113

5.13 Growth rates, $\frac{\gamma}{\omega_{*i}}$. The solid curve is the predicted growth rates from solving Equation 5.10. It is based on all the contributions from ideal MHD stability, FLR effect and ion Landau damping dissipation, while the dashed and dash-dot curves result from ideal MHD with and without FLR stabilization effects. Note that any unstable mode (which may be driven by either resistivity or ion viscosity) can evolve without being hindered between the ideal boundary ($\delta W \equiv 0$) and the FLR stability boundary. 117

5.14 Predicted frequency (ω/ω_{*i}) in the reference frame of the $\mathbf{E} \times \mathbf{B}$ drift. 118

6.1 Peeling mode model contour plot. This figure was imported from the H-mode studies of the ASDEX group (Ref. [90]). 124

6.2 Signal drops on the 2nd harmonic X-mode GPC at each ELM, while signal increases on the fundamental harmonic O-mode radiometer. On the ion saturation current of divertor probe, similar spikes are observed. The magnetics show the toroidal mode number (n) is as high as 14. . 126

6.3 Fractional changes of GPC during Type III ELMy bursts. Overall, 10 $\sim$ 50 % fractional changes were observed. In particular, the changes (26 and 44 %) of Ch 5 and Ch 7 are referenced to check whether a model is appropriate or not. 128

6.4 Density profiles based on measurements and cutoff conditions. TCI-inverted and Thomson scattering density profiles are from measurements. On the other hand, the GPC and radiometer cutoff density profiles are derived from the density cutoff conditions associated with the second harmonic of X-mode and the fundamental harmonic of O-mode respectively. Near the separatrix, two radiometer channels are noted for the signal spikes, which implies that the local density should be lower than their corresponding cutoff densities ($\approx 1.5 \times 10^{20} m^{-3}$). 129

6.5 Resonance layer benchmarked with TORAY. The positions at the resonance layer (R=81.3 cm) agree well between two calculations. The bent trajectory of TORAY reflects the fact that thermal effects are considered for power absorption, while the straight trajectory of the new code is based on cold plasma approximation only. 132

6.6 Density cutoff benchmarked with TORAY. Both the ray trajectories agree well. Near R=82.9 cm, the cutoff occurred and the ray trajectories reflected back. 133

6.7 Density profiles at the midplane 134

6.8 Density models near the midplane. The reference case (a)) has a typical monotonic density profile. Model b), c) and d) have been made to describe the ELMy phenomena. As we shall see later, the model d) turns out to be the most likely. 135

6.9 Definitions of key parameters. The schematic density profile (a-a′) shows the local density height (i.e. n_{trough}) and all the other definitions are self-explanatory in this figure. 138

6.10 Refractive index profiles at the midplane 139

6.11 Schematic diagram of the ray trajectory in vacuum collection optics using OPTICA. The distance between two elliptic mirrors is $2f$=5.4 m, and each optical component is scaled down from the real experimental setup. 140

6.12 Collectible angles vs height in vacuum collection optics. The upper and lower limits of the angles are found using OPTICA. Near z = 15 mm, the lower limit becomes zero. 141

6.13 Ray trajectories of Channel 5 and 7, whose resonance layer are at R =0.804 m and 0.852 m respectively. Note all the rays are near the midplane. These are the reference cases. 144

6.14 Ray trajectories of Channel 5 and 7. Due to density hump, the ray trajectories are bent. 7.4 and 49.5 % signal changes respectively are estimated using Gaussian weighting, while 4.5 and 26.6 % signal changes are estimated using constant weighting. 145

6.15 Ray trajectories of Channel 5 and 7. Due to the poloidally localized density dip, the ray trajectories are refracted drastically. 16.0 and 45.2 % signal changes respectively are estimated using Gaussian weighting, while 10.7 and 33.5 % signal changes are estimated using constant weighting. 147

6.16 Ray trajectories of Channel 5 and 7. Due to the density dip without a bank at larger radii, the ray trajectories are bent enough to be consistent with the experimental observation. 23.2 and 41.8 % signal changes respectively are estimated using Gaussian weighting, while 21.3 and 39.1 % signal changes are estimated using constant weighting. 148

6.17 Comparison with ψ, T_e and n_e. The big circle represents the valid region for mapping each physical parameter. For example, the temperature of point 'a' is mapped onto that of point 'b'. However, if a ray reaches a point outside the big circle, the associated temperature may cause some error but it gives negligible contribution. For example, the resonance layer ($R \sim$0.852 m) for Channel 7 is located within the valid region, while part of the resonance layer ($R \sim$ 0.804 m) for Channel 5 near the edge may contribute to some small errors. 149

6.18 Etendue (AΩ) calculation. 151

6.19 Weighting function ($w_j = w_j(z)$). In practice, the vignetting at the edge of the ECE collection optics aperture requires weighting factors, as shown in the dashed curve. Two extreme cases (Gaussian and constant weighting) were considered in these calculations. In fact, the signal change estimation is weakly dependent on the shape of weighting factors. 152

6.20 Fractional changes of T_e vs poloidal hump elongation. Horizontal lines represent the experimentally observed fractional changes of Ch 5 and Ch 7 of GPC respectively. The estimated signal changes of $\kappa_{hump} = 1.0$ are the closest to the experimentally observed changes. 153

6.21 Fractional changes of T_e vs poloidal dip elongation. Horizontal lines represent the experimentally observed fractional changes of Ch 5 and Ch 7 of GPC respectively. The estimated signal changes of $\kappa_{dip} = 1.0$ are the closest to the experimentally observed changes. 154

6.22 Fractional signal changes vs n_{trough}^{ELM} of a density perturbation model (dipped without edge bank case). Horizontal lines represent the experimentally observed fractional changes of Ch 5 and Ch 7 of GPC respectively. As the minimum density of an ELM model increases, the fractional T_e changes of Ch 5 decrease almost linearly but those of Ch 7 are not reduced much up to the O-mode radiometer cutoff density. On the other hand, as the n_{trough}^{ELM} increases further, the fractional changes of Ch 5 become negligible, while those of Ch 7 decrease nonlinearly down to insignificant levels. As a result, $0.5\times10^{20}m^{-3}$ was found to be the most likely local density at R = 0.89 m. 157

6.23 Ambiguity of refraction effects. The deviated angle at R=R1 based on a refractive index Curve A will be the same as that at R=R2 based on Curve B, as calculated in Equation 6.8. 159

6.24 Enlarged view of the refractive index contour plot for edge parameter definitions. δz is $\kappa_{dip}\delta R$, which provides the poloidal wave number k_θ is $2\pi/\lambda_\theta = 2\pi/(2\delta R\kappa_{dip})$. 160

6.25 Fractional changes of T_e vs poloidal dip elongation in the dip without edge density bank model. Horizontal lines represent the experimentally observed fractional changes of Ch 5 and Ch 7 of GPC respectively. The fractional changes of Ch 5 are sensitive to the elongation, which varies linearly down to $\kappa_{dip} = 2.0$. In contrast, the changes of Ch 7 are insensitive for $\kappa_{dip} \leq 1.5$ and then drops rapidly, as κ_{dip} increases. As a result, κ_{dip}= 1.5 was found to be the closest to the experimental observations. 161

6.26 Time traces of GPC and magnetics near the ELM event. On GPC, there is no precursor, but during the ELM event, the signal drops almost linearly and recovers within 20 μsec in this case. On magnetics, there are coherent precursors at 160$\sim$200 kHz, which disappear in the midst of the ELM. The phases between toroidally adjacent coils change rapidly and the associated toroidal mode number is n$\sim$ 14. 165

6.27 Fractional signal changes vs poloidal rotation angle of an ELM density perturbation model (dipped without edge bank case). Horizontal lines represent the experimentally observed fractional changes of Ch 5 and Ch 7 of GPC respectively. As the poloidal rotation angle increases, the signal changes of both Ch 5 and Ch 7 decrease nearly linearly. Here, the poloidal rotation angle is defined in Figure 6.9. The 6 degree is almost equivalent to 2.0 cm poloidal displacement of an ELM position. 166

List of Tables

1.1 Alcator C-Mod parameters. 32

3.1 Classification of ideal MHD tokamak instabilities 65

5.1 Characteristic frequencies 115

6.1 Signal changes of each model 155

Chapter 1

Introduction

Fusion as an inexhaustible energy resource has been sought for more than a half century [1]. Although the research did not start from peaceful applications, the ultimate goal of realizing a commercially feasible fusion reactor has been pursued in various countries. In spite of the past enormous progresses in understanding such fusion plasmas, we still need to go further. Entering the 21st century, we are now facing financially challenging obstacles, as well as scientifically unsolved issues. One of the biggest concerns is whether such a costly project as ITER (International Thermonuclear Experimental Reactor) can be sponsored by the governments of the countries involved. Nevertheless, since fusion reactors have huge potential to solve the energy crises our next generations will meet, fusion research is a sort of 'crusade' activity for the future of human-beings.

1.1 Fusion

The basic fusion concept is similar to that of fission in that we are trying to take advantage of the binding energy differences among nucleons during each reaction. However, fusion energy is released when light nuclei, such as deuterium (D_1^2) and tritium (T_1^3), are fused into a heavy nucleus, while fission energy is generated when a heavy nucleus(eg. U^{235}) is split into light nuclei.

Nowadays, there are two main streams of research regarding fusion reactors. One

is to exploit 'inertially confined plasmas', where centrally focussed laser beams can ablate shells of a pellet directly and the recoil momenta of the exploding shells can push in and implode the inner fuels, which creates a fusion reaction with high density and temperature plasmas. Since any asymmetry of the laser beams that impinge onto the the fuel metal surface triggers Rayleigh-Taylor instability, an indirect method called "Hohlraum" is considered as an alternative because it can heat the shell surface uniformly. In a "Hohlraum", a high-Z metal, such as gold, is used for generating Bremsstrahlung radiation, which will heat up the surface material of a fuel and lead it into implosion. *NIF* (National Ignition Facility) is based on such an inertially confined plasma.

The other main research stream makes use of 'magnetically confined plasmas', where the particles are confined by virtue of magnetic fields. Although an open-end mirror machine was used for this type of plasma, it has been almost abandoned for further hot plasma research. Closed-end (toroidal) devices, such as the Tokamak[1] and Stellerator, dominate magnetically confined plasma research. The tokamak has been regarded one of the most promising candidates for realizing a self-sustaining burning plasma, which will be essential for a commercially viable fusion reactor.

1.2 Alcator C-Mod

In MIT, there were two predecessors to the Alcator[2] C-Mod tokamak, which has been operational since 1994, named Alcator A and C. All three devices are noted for their high magnetic field. The main physical parameters of Alcator C-Mod (See Figure 1.1) are given in Table 1.1.

The inner chamber surface of Alcator C-Mod is covered with tiles of Molybdenum, which is a refractory material. For removing the impurities, a toroidal divertor is installed. In short, Alcator C-Mod is a *compact*, *high field*, *divertor* tokamak.

[1] In Russian, toroidal chamber with magnetic coil
[2] In Latin, high field torus

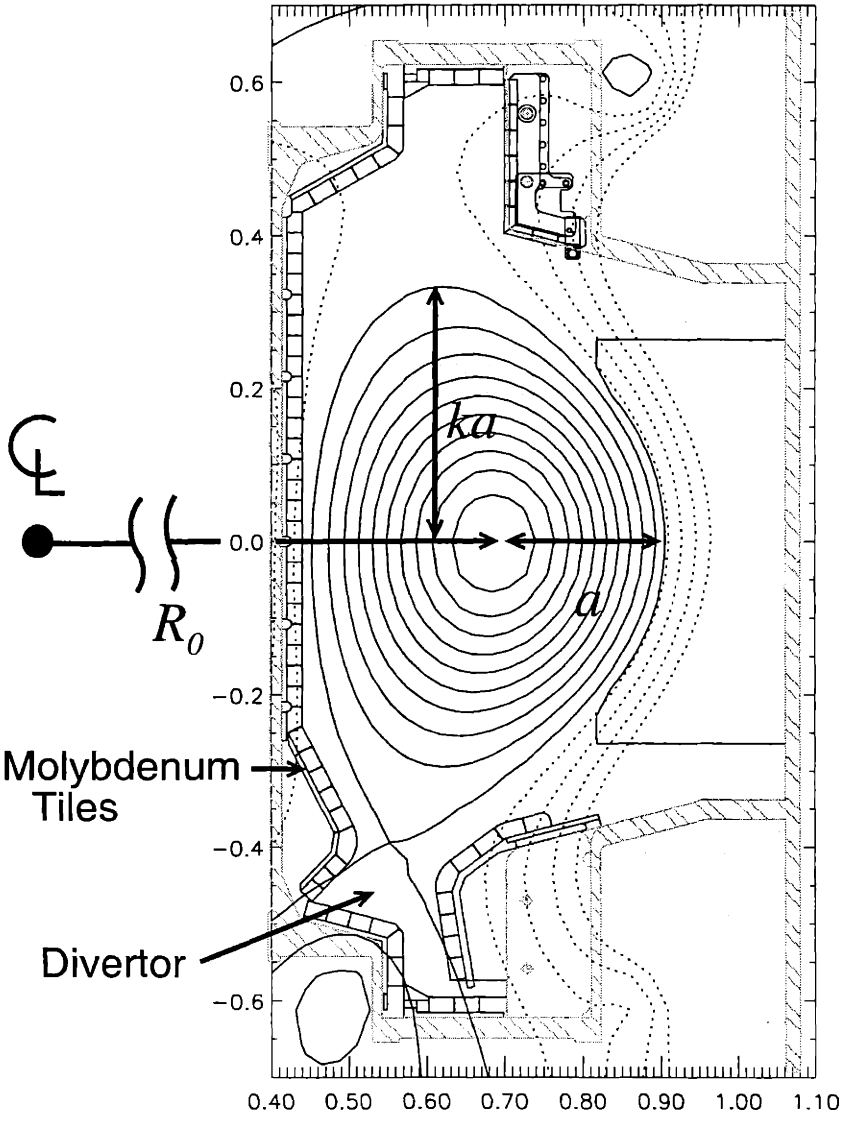

Figure 1.1: Alcator C-Mod cross section with typical magnetic flux surfaces. The surface of the in-vessel is covered with molybdenum tiles, unlike in other tokamaks whose in-vessel surfaces are usually covered with reinforced carbon graphite tiles.

Parameter	Notation	Achieved (Max.) Value	
Major Radius	R_0	0.67	m
Minor Radius	a	0.22	m
Magnetic Field	B_T	8 (9)	T
Plasma Current	I_p	1.5 (3)	MA
Electron Density	n_e	$\leq 1.1 \times 10^{21}$	m^{-3}
Electron Temperature	T_e	≤ 6	keV
Auxiliary Heating	P_{RF}	3.5 (8)	MW
Elongation	κ	0.95 – 1.85	

Table 1.1: Alcator C-Mod parameters.

1.2.1 Heating Schemes

There are two schemes to heat up the plasmas in Alcator C-Mod. The first is "Ohmic" heating, which utilizes the plasma resistivity to generate 'Joule' heat ($\propto \eta j^2$, where η: resistivity, j: current density). The other is called "auxiliary" heating, which adds more power to the ohmically heated plasmas. Currently, ICRF (Ion Cyclotron Resonance Frequency) heating system is the only "auxiliary" heating scheme in C-Mod. It uses two double-strap antennas (4 MW at 80 MHz) and, as of Oct 1999, a compact four-strap antenna which occupies only one port (4 MW tunable at 40~80 MHz). In other tokamaks, such as JT-60U, JET, DIII-D and TFTR, there are other auxiliary heating schemes, such as NBI (neutral beam injection) heating systems.

1.2.2 ECE diagnostics

There are several electron temperature (T_e) measurement diagnostics in Alcator C-Mod. For the bulk plasma, there are 5 electron cyclotron emission (ECE) diagnostics; a Michelson interferometer [2], two grating polychromators (9 and 19 channels respectively) [3, 4], and two radiometers (8 and 32 channels respectively) [5]. Since most of the magnetohydrodynamic (MHD) instabilities discussed in this thesis were observed using the ECE diagnostics, a rather detailed discussion of ECE principles and diagnostics will be given in Chapter 2.

1.2.3 Other diagnostics

In addition to the ECE diagnostics, the electron temperature(T_e) is measured by Thomson Scattering, which also provides electron density (n_e) in the core. Recently, the edge Thomson Scattering system [6] has been installed and commissioned. For electron density (n_e), a two-color interferometer (TCI) [7], visible Bremsstrahlung diagnostic arrays [8, 9] (so called 'Z-meter'), a reflectometer [10, 11] and edge Langmuir probes [12] are used. For the ion temperature (T_i), there are two diagnostics we can rely on; a neutron production rate detector [13] and high resolution X-ray spectrometers [14]. T_i is inferred from the neutron production rates based on an assumed profile, while it is directly measured from high-Z impurity X-ray line emission by the latter diagnostic. Depending on the wavelengths concerned, there are other spectroscopic measurements, such as soft X-ray tomography, high resolution edge X-ray diagnostics [15], and visible imaging systems. In addition, a Phase Contrast Imaging (PCI) [16] system provides coherent fluctuation wavevector and frequency information.

1.3 Scope of the thesis

1.3.1 MHD activity in tokamaks

Considering that the ultimate goal of fusion research is to build a commercial fusion reactor, steady state operation is regarded as indispensable. The so-called 'advanced tokamak scenarios' are based on such a steady state, high performance plasma [17]. One of the most promising candidates is 'reversed magnetic shear plasma' because it has so many favorable features in terms of confinement, stability and self-sustaining bootstrap current [18]. Here, reversed shear means that a current profile is hollow, instead of the typically monotonic profile. In fact, many experiments have since verified such high performance plasmas in various tokamaks [19, 20, 21]. However, in recent C-Mod reversed shear experiments [22, 23], we observed some global MHD activity, which affected the whole plasma. Sometimes, the MHD influences are so

serious as to nearly terminate the plasmas. In this regard, we cannot expect to obtain high performance reversed shear plasmas without circumventing such unfavorable MHD activity. Thus, the understanding of the MHD modes needs to be pursued and it has been a primary interest of the author.

In recent fusion research, high confinement time mode (H-mode) [24] plasmas have been one of the most extensively studied themes. During H-mode plasmas, the energy confinement time (τ_E) improves by a factor of greater than 2, in comparison with low confinement time mode (L-mode), through edge transport barrier formation, which is often described as edge 'pedestal'. However, a so-called ELM-free H-mode has better particle confinement time (τ_p) as well, which will lead to an impurity accumulation and eventually destroy the H-mode. On the other hand, there are other promising H-mode regimes for future tokamaks which may resolve such unfavorable impurity accumulation problems; enhanced D_α (EDA) H-modes and edge localized modes (ELMs).

Unlike other tokamaks, Alcator C-Mod has not encountered large "Type I" ELMs yet, but enters a new regime, called EDA H-mode. The absence of Type I ELMs in Alcator C-Mod is perhaps due to limited input power, while the uniqueness of EDA may arise partly from high shaping capability. EDA H-modes are characterized by high energy confinement time and low particle confinement time, which permits sustainment of the high performance plasmas without suffering impurity accumulations [25]. Meanwhile, ELMs are characterized by rapid radial particle losses in the low-field side, which helps to release accumulated impurities in a self-regulatory way. Both H-mode regimes are also accompanied by some MHD activity. For EDA H-modes, there are so called 'fast edge modes' [26], which do not have apparent adverse effects but are under detailed study using reflectometry and PCI.

For ELMs, there are few appropriate diagnostics to resolve the spatiotemporal characteristics, given their rapidly changing localized ballooning features. Although the temporal issue can be mitigated by increasing sampling frequencies of diagnostics, the spatial extent of ELMs is still challenging. In particular, the local perturbations due to smaller "Type III" ELMs are very difficult to directly measure, although they

would be desirable in the view of controlling ELMs. All the edge parameters (e.g. pedestal position, width and height and perhaps poloidal gyroradius) are critical for determining the quality of high performance plasmas. The dimensions of the ELMs are thus important to indicate the features of the pedestal and its instability. In this regard, this thesis may help to open the door to improved physical understanding of ELMy bursts.

1.3.2 Outline of the thesis

The contents of each chapter are outlined briefly here.

- **Chapter 2:** Electron cyclotron emission (ECE) principles are reviewed with emphasis on the diagnostic issues in tokamak applications. The ECE diagnostic systems on Alcator C-Mod are described.

- **Chapter 3:** Summarizes magnetohydrodynamic (MHD) theory, emphasizing the ideal MHD model which provides physical understanding of instability sources and their classifications. In addition, resistive modes are introduced and the characteristic times of MHD activity are discussed.

- **Chapter 4:** Analyzes MHD activity during current ramp up in terms of resistive modes. In particular, a resistive "multiple" tearing mode has been identified during reversed magnetic shear plasmas. A resistive interchange mode during low β plasma has also been predicted.

- **Chapter 5:** Identifies the ideal interchange mode for the first time in tokamak experiments. Based on ideal MHD theory, it was predicted to be unstable, while the inclusion of finite ion Larmor radius (FLR) stabilized the mode. As the thermal ion transit frequency (ω_{ti}) was comparable to ion diamagnetic drift frequency (ω_{*i}), the dissipation of ion Landau damping was found to be strong enough to drive a kinetic Mercier instability.

- **Chapter 6:** Infers the geometrical dimensions of edge localized modes (ELMs). These have been inferred from refracted ECE signals. For this analysis, a ray tracing code has been developed and used to find ECE ray trajectories. Based on an edge density model, the ray trajectories are found to be refracted enough to get reduced signals, as was found in the experimental observations, which allows us to infer the ELMy geometry. This indirect method to measure the ELMy dimensions is the first approach to obtain reasonable values.

- **Chapter 7:** Summarizes all the above chapters and discusses future work.

In brief, the key results of this thesis are that i) the MHD activity during reversed shear plasmas has been analyzed, which led to an identification of resistive "multiple" tearing modes and prediction of resistive interchange modes [23]; ii) the first identification of ideal interchange mode is discussed in detail, including the kinetic effects [27]; and iii) the ELMy dimensions have been inferred for the first time using refraction effects.

Chapter 2

ECE Diagnostics

Electron cyclotron emission (ECE) will be reviewed with respect to the radiated power density, associated electromagnetic waves and propagation, and its diagnostic application in tokamaks. Since the purposes of this chapter are to review important principles and to unify the notations and concepts which are used in the following chapters, the reader is referred for a more detailed treatment to excellent articles [28, 29] and textbooks [30, 31, 32].

2.1 ECE principles

ECE is used for measuring electron temperatures in magnetized plasmas. The basic idea stems from the fact that any charged particles emit cyclotron radiation during their gyrating motions in the externally applied magnetic field. As shown in Figure 2.1, suppose that there is an external magnetic field along the z axis, $\mathbf{B}=B_0\hat{\mathbf{z}}$, and that we take the angle to be θ between an emission wavevector $\mathbf{k}$ and magnetic field $\mathbf{B}$. Without loss of generality, we can define $\mathbf{k} = k\sin\theta\hat{\mathbf{x}} + k\cos\theta\hat{\mathbf{z}}$.

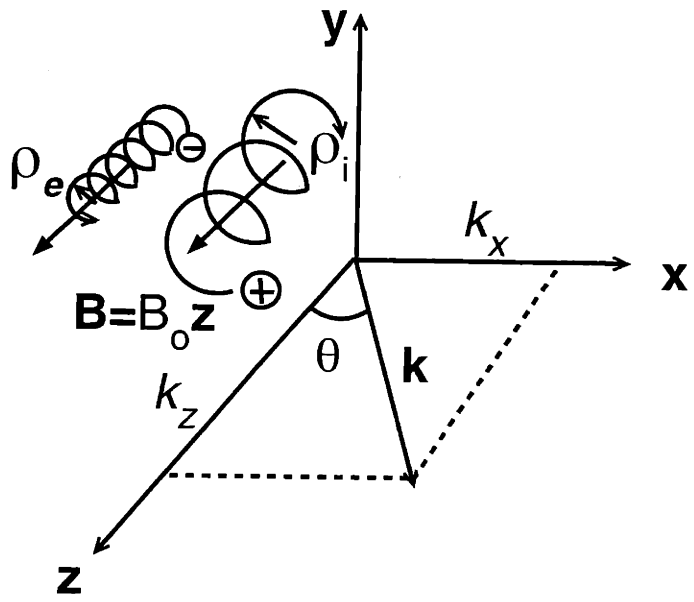

Figure 2.1: **Gyrating electron (ion) trajectory drifting along magnetic field (B).**
Note that the electron gyroradius (ρ_e) is smaller than the ion gyroradius (ρ_i), given the same temperature. The parallel component ($k_{\|}$) of the wavevector ($\mathbf{k}$) is k_z, while the perpendicular component ($k_{\perp}$) is k_x.

2.1.1 Radiation from gyrating charged particles

According to the Schott-Trubnikov formula [33], the radiated power of a particle per unit frequency per unit solid angle observed in a lab frame is given by

$$\frac{d^2P}{d\omega d\Omega_s} = \frac{e^2\omega^2}{8\pi^2\epsilon_0 c}\sum_{m=1}^{\infty}\left[\left(\frac{cos\theta-\beta_{\|}}{sin\theta}\right)^2 J_m^2(\xi)+\beta_{\perp}^2 J'^2_m(\xi)\right]\frac{\delta\left(\left[1-\beta_{\|}cos\theta\right]\omega-m\omega_c\right)}{1-\beta_{\|}cos\theta}$$

where $\beta=\frac{\mathbf{v}}{c}, \xi=\frac{\omega}{\omega_c}\beta_{\perp}\sin\theta$, c is the speed of light. (2.1)

Since we want to know the rate of energy loss from an assembly of particles, the total power loss from any volume element is obtained by multiplying Eq. 2.1 by (1 - $\beta_{\|}\cos\theta$) and integrating the expression by $fd^3\mathbf{x}d^3\mathbf{v}$ [31].

When the plasma density is sufficiently tenuous ($\omega_p/\omega_c \ll 1$), the preceding free space treatment is appropriate. Then, we may assume that the electrons are completely uncorrelated so that the total emissivity is obtained by integrating all the intensities from each electron. Thus, the plasma emissivity $j(\omega,\theta)$, which is the rate of emission of radiant energy from the plasma per unit volume per unit angular frequency per unit solid angle $[W/(m^3\cdot Sr\cdot s^{-1})]$, can be obtained in a form:

$$j(\omega,\theta)=c^3\int\frac{d^2P}{d\omega d\Omega_s}(1-\beta_{\|}cos\theta)f(\beta_{\perp},\beta_{\|})2\pi\beta_{\perp}d\beta_{\perp}\beta_{\|}. \quad (2.2)$$

For a nonrelativistic ($\beta \ll 1$) Maxwellian plasma, the frequency integrated emissivity (j_m: m-th harmonic emissivity at $\omega_m = m\Omega$) can be calculated directly and is given by:

$$j_m=\frac{e^2\omega_m^2 n_e}{8\pi^2\epsilon_0 c}\frac{m^{2m-1}}{(m-1)!}(\sin\theta)^{2(m-1)}(\cos^2\theta+1)\left(\frac{T}{2m_e c^2}\right)^m. \quad (2.3)$$

The distribution of emissivity is expressed in terms of a shape function $\phi(\omega-\omega_m)$, which is defined as

$$j_m(\omega)=j_m\phi(\omega-\omega_m), \quad \int\phi(\omega)d\omega=1 \quad (2.4)$$

2.1.2 Plasma waves in magnetized plasmas

Wave equation From Maxwell's relations, the electromagnetic waves in magnetized plasmas can be described as follows;

$$\nabla \times (\nabla \times \mathbf{E}) = -\left[\mu_0 \frac{\partial \mathbf{j}}{\partial t} + \frac{1}{c^2}\frac{\partial^2 \mathbf{E}}{\partial t^2}\right] \tag{2.5}$$

In general, the current density $\mathbf{j}$ can be represented in terms of electric field $\mathbf{E}$ and the conductivity tensor $\overleftrightarrow{\sigma}$:

$$\mathbf{j} = \overleftrightarrow{\sigma} \cdot \mathbf{E} \tag{2.6}$$

Now, if we take Fourier-Laplace transformations on Eq. 2.5, the ∇ is replaced with $i\mathbf{k}$ and the $\frac{\partial}{\partial t}$ with $-i\omega$. After some vector manipulations, we may introduce the refractive index vector as $\mathbf{N} = \frac{c\mathbf{k}}{\omega}$ and the wave equation becomes

$$\mathbf{N}(\mathbf{N} \cdot \mathbf{E}) - N^2\mathbf{E} + \overleftrightarrow{\epsilon} \cdot \mathbf{E} = 0 \tag{2.7}$$

where $\overleftrightarrow{\epsilon}$ is the dielectric tensor ($\equiv 1 + \overleftrightarrow{\chi} = 1 + \frac{\overleftrightarrow{\sigma}}{-i\omega\epsilon_0}$). Similarly, if we assume that all the oscillating wave quantities are proportional to $\exp[i(\mathbf{k} \cdot \mathbf{r} - \omega t)]$ with complex $\mathbf{k}$ and real ω, like plane waves, we may obtain the same final wave equation as Eq. 2.7. Considering $\mathbf{N} = N_x\hat{\mathbf{x}} + N_z\hat{\mathbf{z}}$, the wave equation can be written in a matrix form $\overleftrightarrow{D} \cdot \mathbf{E} = 0$;

$$\begin{bmatrix} -N_z^2 + \epsilon_{xx} & \epsilon_{xy} & N_xN_z + \epsilon_{xz} \\ \epsilon_{yx} & -N^2 - \epsilon_{yy} & \epsilon_{yz} \\ N_zN_x + \epsilon_{zx} & \epsilon_{zy} & -N_x^2 + \epsilon_{zz} \end{bmatrix} \begin{bmatrix} E_x \\ E_y \\ E_z \end{bmatrix} = 0. \tag{2.8}$$

where N_x and N_z can be replaced with $N_\perp$ and $N_\parallel$ respectively without loss of generality. To get a non-trivial solution, the determinant of the coefficients should be zero.

$$\|\overleftrightarrow{D}\| = 0, \tag{2.9}$$

where $\overleftrightarrow{D}$ is the dispersion tensor.

Cold plasma approximation Supposing that there is a tenuous plasma with no thermal motions ($T_{i(e)}$=0) , the equation of motion for species j is

$$m_j \frac{\partial \mathbf{v_j}}{\partial t} = q_j(\mathbf{E} + \mathbf{v_j} \times \mathbf{B}). \tag{2.10}$$

The velocity components can be solved in terms of $\mathbf{E}$;

$$\begin{aligned} v_{xj} &= \frac{q_j}{m_j}\left(\frac{i\omega E_x - \Omega_j E_y}{\omega^2 - \Omega_j^2}\right) \\ v_{yj} &= \frac{q_j}{m_j}\left(\frac{\Omega_j E_x + i\omega E_y}{\omega^2 - \Omega_j^2}\right) \\ v_{zj} &= \frac{q_j}{m_j}\frac{iE_z}{\omega} \end{aligned} \tag{2.11}$$

where $\Omega_j = \frac{q_j B_0}{m_j}$ is the cyclotron frequency . Using Eq. 2.6 and Eq. 2.12 with $\mathbf{j} = \sum_j (nq\mathbf{v})_j$, the conductivity tensor ($\overleftrightarrow{\sigma}$) can be found as

$$\overleftrightarrow{\sigma} = \begin{bmatrix} \sigma_{xx} & \sigma_{xy} & 0 \\ \sigma_{yx} & \sigma_{yy} & 0 \\ 0 & 0 & \sigma_{zz} \end{bmatrix} \tag{2.12}$$

where $\sigma_{xx} = \sigma_{yy} = \sum_j \frac{q_j^2 n_j}{m_j} \frac{i\omega}{\omega^2 - \Omega_j^2}$, $\sigma_{xy} = -\sigma_{yx} = -\sum_j \frac{q_j^2 n_j}{m_j} \frac{\Omega_j}{\omega^2 - \Omega_j^2}$, $\sigma_{zz} = \sum_j \frac{q_j^2 n_j}{m_j} \frac{i}{\omega}$.
Since the relationship between the dielectric tensor ($\overleftrightarrow{\epsilon}$) and the susceptibility ($\overleftrightarrow{\chi}$) (or conductivity ($\overleftrightarrow{\sigma}$)) tensor is $\overleftrightarrow{\epsilon} \equiv 1 + \overleftrightarrow{\chi} = 1 + \frac{\overleftrightarrow{\sigma}}{-i\omega\epsilon_0}$, the dielectric tensor ($\overleftrightarrow{\epsilon}$) becomes

$$\overleftrightarrow{\epsilon} = \begin{bmatrix} \epsilon_{xx} & \epsilon_{xy} & 0 \\ \epsilon_{yx} & \epsilon_{yy} & 0 \\ 0 & 0 & \epsilon_{zz} \end{bmatrix} = \begin{bmatrix} S & -iD & 0 \\ iD & S & 0 \\ 0 & 0 & P \end{bmatrix} \tag{2.13}$$

where S, D, and P are Stix parameters [32] as follows;
Introducing R and L as

$$R \equiv 1 - \sum_j \frac{\omega_{p_j}^2}{\omega^2}\left(\frac{\omega}{\omega + \Omega_j}\right) \tag{2.14}$$

$$L \equiv 1 - \sum_j \frac{\omega_{p_j}^2}{\omega^2} \left(\frac{\omega}{\omega - \Omega_j} \right)$$

S, D, and P are expressed as

$$\begin{aligned} S &\equiv \frac{R+L}{2} = 1 - \sum_j \frac{\omega_{p_j}^2}{\omega^2 - \Omega_j^2} \\ D &\equiv \frac{R-L}{2} = \sum_j \frac{\Omega_j}{\omega} \frac{\omega_{pj}^2}{\omega^2 - \Omega_j^2} \\ P &\equiv 1 - \sum_j \frac{\omega_{p_j}^2}{\omega^2} \end{aligned} \tag{2.15}$$

where $\omega_{pj}^2 \equiv \frac{q_j^2 n_j}{\epsilon_0 m_j}$ is the plasma frequency.

Based on the Stix parameters and Eq. 2.8, the dispersion tensor ($\overleftrightarrow{D}$) can be expressed in the form

$$\overleftrightarrow{D} = \begin{bmatrix} -N^2\cos^2\theta + S & -iD & N^2\sin\theta\cos\theta \\ iD & -N^2 + S & 0 \\ N^2\sin\theta\cos\theta & 0 & -N^2\sin^2\theta + P \end{bmatrix}. \tag{2.16}$$

Thus, the dispersion relation becomes a quadratic in terms of N^2 as follows;

$$AN^4 + BN^2 + C = 0 \tag{2.17}$$

where $A = S\sin^2\theta + P\cos^2\theta$, $B = RL\sin^2\theta + PS(1+\cos^2\theta)$, $C = PRL$.

This can be rewritten in another form

$$\tan^2\theta = \frac{-P(N^2 - R)(N^2 - L)}{(SN^2 - RL)(N^2 - P)} \tag{2.18}$$

Thus, the parallel (θ=0) and perpendicular ($\theta = \frac{\pi}{2}$) propagation dispersion relations are

Parallel($\|$) : $P = 0, \quad N^2 = R(\mathrm{R-wave}), \quad N^2 = L(\mathrm{L-wave})$

$$\textbf{Perpendicular}(\perp) \quad : \quad N^2 = \frac{RL}{S}(\mathrm{X-wave}), \quad N^2 = P(\mathrm{O-wave}) \tag{2.19}$$

When N^2 goes to 0 and ∞, it reaches cutoff and resonance respectively. Such cutoff and resonance conditions determine important singular points in wave propagations. In particular, the perpendicular wave (X and O mode) propagation, cutoff and resonances are critical to understanding tokamak ECE diagnostics principles. For

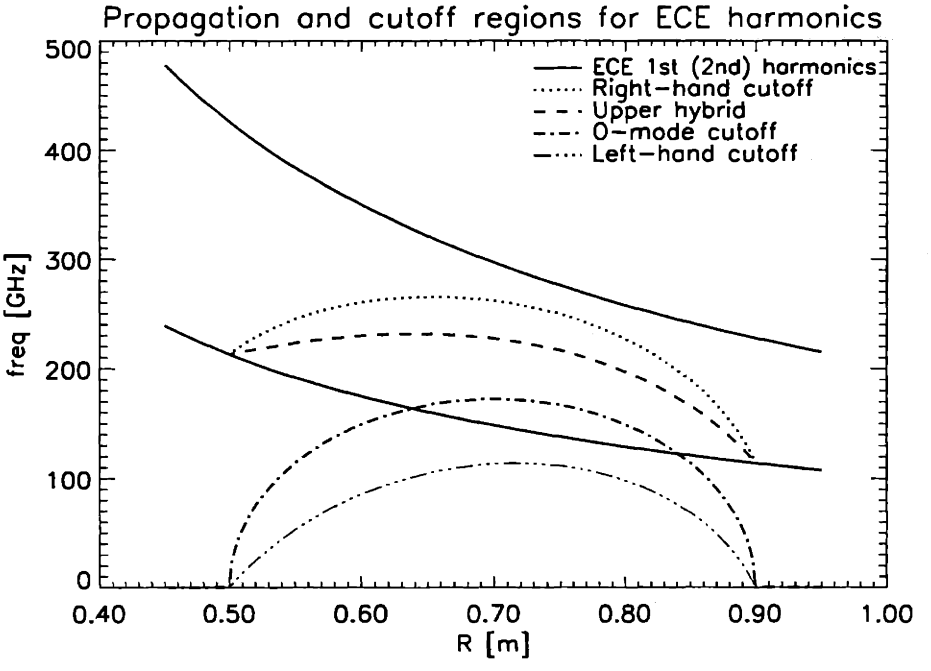

Figure 2.2: **ECE harmonics, cutoffs and resonance frequencies**
Based on monotonic density ($\propto [1-(\frac{r}{a})^2]$) and magnetic field ($B = \frac{B_0 R}{R_0}$) profile, the associated frequencies are shown. B_0=5.3 T and n_0=3.66 $\times 10^{20} m^{-3}$ are assumed.

O-mode, the cutoff frequency is the same as the plasma frequency (ω_p). For X-mode, there are two cutoffs ($\omega_{R(L)}$: Right (left) hand cutoff) and one resonance frequency (ω_{UH}: upper hybrid resonance frequency).

Here,

$$\begin{aligned} \omega_{R(L)} &= \frac{1}{2}\Omega_{ce}\left[\pm 1 + \left(1 + 4\frac{\omega_p^2}{\Omega_{ce}^2}\right)^{1/2}\right] \\ \omega_{UH} &= \sqrt{\Omega_{ce}^2 + \omega_{pe}^2}. \end{aligned} \tag{2.20}$$

Figure 2.2 shows the ECE harmonic frequencies ($m\Omega_{ce}$), cutoffs ($\omega_{R(L)}$), and upper hybrid frequency (ω_{UH}) in a typical (i.e. monotonic density profile) C-Mod plasma.

2.1.3 Propagation in the optically thick plasma

Radiation Transport In general, the radiation intensity can be calculated by considering the emissivity as a source and absorptivity as a sink, which can be described as follows;

$$\frac{dI}{ds} = j(\omega) - \alpha(\omega)I \tag{2.21}$$

where I is the radiation intensity $[W/(m^2 \cdot Sr \cdot s^{-1})]$, s is the path length, $j(\omega)$ is the emissivity, and $\alpha(\omega)$ is the fractional rate of absorption of radiation per unit path length. Thus, the radiation intensity from point 1 to point 2 can be determined by

$$I(s_2) = I(s_1)e^{-\tau_{21}} + (j/\alpha)\left[1 - e^{-\tau_{21}}\right] \tag{2.22}$$

where τ is the "optical depth" given by: $\tau(s) \equiv \int^s \alpha(\omega)ds, \quad \tau_{21} \equiv \tau_2 - \tau_1$.
When $\tau_{21} \gg 1$, the Eq. 2.22 becomes

$$I_{\tau \gg 1} = j/\alpha. \tag{2.23}$$

In this limit, we call the plasma "optically thick".

Blackbody Radiation If any body is perfectly absorbing and radiating in thermodynamic equilibrium, it emits a so called "blackbody" intensity

$$I(\omega) = B(\omega) = \frac{\hbar\omega^3}{8\pi^3c^2}\frac{1}{\exp[\frac{\hbar\omega}{T}] - 1} \tag{2.24}$$

where $\hbar$: Planck's constant$(=\frac{h}{2\pi})$.
For low frequency $\hbar\omega \ll T$, the intensity becomes

$$B(\omega) = \frac{\omega^2 T}{8\pi^3c^2}. \tag{2.25}$$

In the optically thick plasma, the above equation should be the same as Eq. 2.23 (Kirchhoff's law); that is

$$B(\omega) = \frac{j}{\alpha}. \tag{2.26}$$

Here the absorption coefficient (α) for the mth harmonic can be found as [29, 31]

$$\alpha_m \equiv \frac{\pi}{2c}\omega_{pe}^2 \frac{m^{2m-1}}{(m-1)!}(sin\theta)^{2(m-1)}(cos^2\theta + 1)\left(\frac{T}{2m_e c^2}\right)^{m-1}. \tag{2.27}$$

2.1.4 Temperature measurement using ECE in tokamaks

Considering a tokamak plasma whose properties vary slowly in space ($\lambda \ll L$), the WKBJ approximation ("eikonal" or "geometrical optics") is very useful [31]. For the mth harmonic near a specific cyclotron resonance frequency (ω_0), the optical depth is calculated as follows;

$$\begin{aligned} \tau_m &\equiv \int \alpha_m(\omega) ds = \int \alpha_m(\omega) \left|\frac{d(m\Omega)}{ds}\right|^{-1} d(m\Omega) \\ &= \alpha_m \left|\frac{d\Omega}{ds}\right|^{-1} \int \phi(\omega_0 - m\Omega) d\Omega \\ &= \frac{\alpha_m}{m\,|d\Omega/ds|} = \frac{R\alpha_m}{m\Omega} \end{aligned} \tag{2.28}$$

where ϕ is defined in Eq. 2.4 so that $\int \phi(\omega_0 - m\Omega)d\Omega = 1/m$ (assuming ϕ is narrow at the resonance layer), and R$\equiv \Omega/|d\Omega/ds|$. In a tokamak, the major radius gives the **B** scale length.

Assuming no radiation incident on the plasma from outside, the single wave polarization intensity can be calculated based on Eq. 2.22 and it becomes

$$I(\omega_0) = \frac{{\omega_0}^2 T(s)}{8\pi^3 c^2}(1 - e^{-\tau_m}) \tag{2.29}$$

where ω_0: resonant frequency at only one position and harmonic. In particular, when the optical depth is much larger than 1 ($\tau_m \gg 1$), Eq. 2.29 becomes the blackbody intensity formula (Eq. 2.25) and we are able to measure the electron temperature (T_e)

by inverting the formula;

$$T_e = I(\omega_0 = m\Omega) \cdot \frac{8\pi^3 c^2}{(m\Omega)^2} \tag{2.30}$$

Only O-mode first harmonic and X-mode 2nd harmonic are useful for standard ECE temperature measurements because of their 'optically thick' characteristics under typical tokamak core conditions, while other harmonics can be used in principle but need to be scrutinized due to insufficient optical depths. Since τ is typically greater than 10 in most C-Mod plasmas, we can take advantage of the linear relationship of Eq. 2.30 between electron temperature (T_e) and collected signal intensity (I) almost all the time. However, if the density and temperatures are low, the optical depths should be investigated. That is because the optical depths of the first and second harmonics of the O-mode and X-mode are dependent on $n_e T_e$. For example, the optical depth of the second harmonic X-mode is

$$\tau^X_{m=2} \approx \frac{\pi R}{\Omega c} \frac{n_e e^2}{m_e \epsilon_0} \frac{T_e}{m_e c^2}. \tag{2.31}$$

Figure 2.3 shows the surface and contour plots of the optical depth depending on density and temperature at R=0.89 m and $2\Omega/2\pi$=226 GHz. Near the plasma edge conditions of both L and H-modes, the optical depth is in the optically 'grey' region, so the previous analysis based on the 'optically thick' plasmas underestimates the temperature.

Another important requirement in using ECE diagnostics in tokamak is to remove harmonic overlap. A mth harmonic at R can be overlapped with a $(m-1)$th harmonic at higher field, as well as with a $(m+1)$th harmonic at lower field. For example, near major radius R, the second harmonic frequency becomes the same as the first harmonic at R/2 and so does the third harmonic at 3/2R. When this occurs, the ECE diagnostic is not radially localized. Only in the overlap-free region is there a one-to-one mapping among frequency, magnetic field and location. That is, if the frequency is defined, the corresponding magnetic field strength is found and then the emission location is determined on the basis of a reconstructed equilibrium. The overlap-free

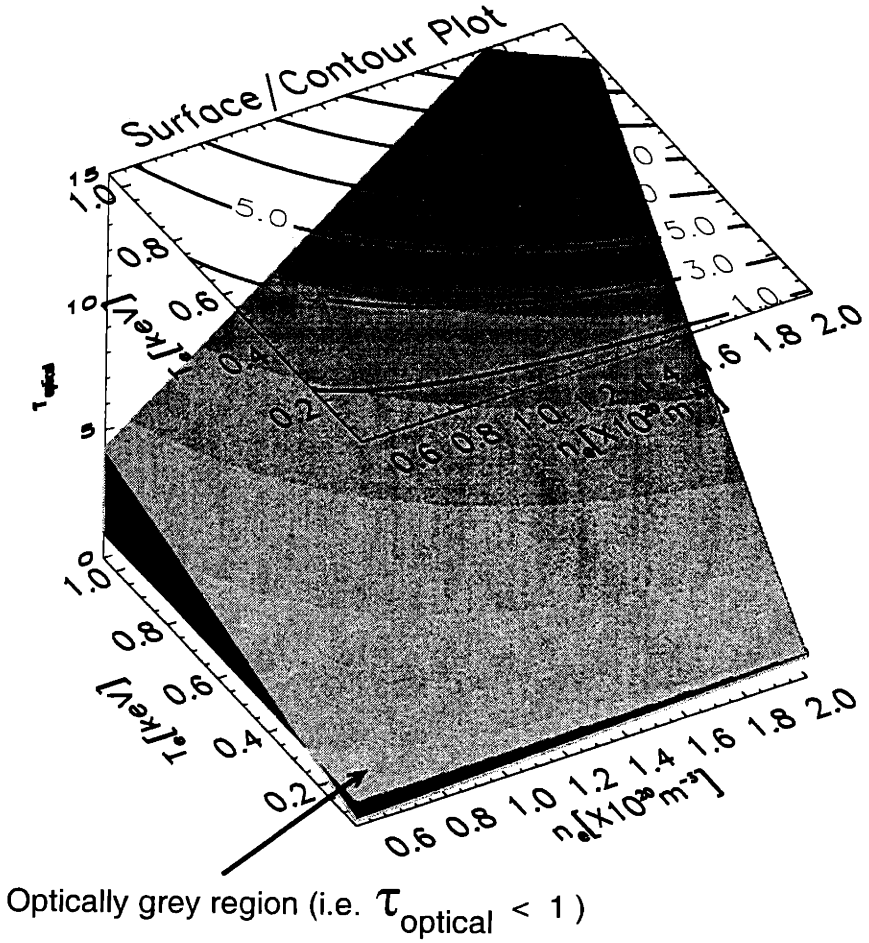

Figure 2.3: Optical depth surface and contour plots. Assuming R=0.89 m and $2\Omega/2\pi$=226 GHz (i.e. the outermost channel of GPC (Ch 9)), the density and temperature can become so low that the optical depth could be in the 'optically grey' region for both L and H modes. In this case, the analysis based on an optically thick plasma tends to underestimate the electron temperature.

region can be found by satisfying the following condition;

"The frequency concerned ($\Omega_m(R)$) should be i) larger than the highest $(m-1)th$ harmonic ($\Omega_{m-1}(R_0-a)$) at the high field side and ii) smaller than the lowest $(m+1)th$ harmonic ($\Omega_{m+1}(R_0+a)$) at the low field side."

$$[\frac{(m-1)}{R_0-a} < \frac{m}{R} < \frac{m+1}{R_0+a}] \times (\frac{qB_0R_0}{m_e}) \tag{2.32}$$

So, $(R_0+a)\frac{m}{m+1} < R < (R_0+a)\frac{m}{m-1}$ shows the overlap-free region. For m=2, 60 $\sim$ 90 cm is the overlap-free range in C-Mod. Since $R_0 \approx 0.67$ m and the LCFS is generally less than 90 cm, the overlap issue of the first and second harmonics is not a problem and all of the outer half of the profile can be measured. For m=1, all the plasma radii belong to the overlap-free region (44 cm to ∞).

2.2 ECE diagnostics in Alcator C-Mod

As shown Figure 2.4, Alcator C-Mod is equipped with various ECE diagnostics. Except for the newly installed 32 channel radiometer located at F-port, all the ECE diagnostics have the same upstream 'quasioptical' beamline located at H-port. Here, "quasioptical" means that the dimensions of some optical components can be comparable to the wavelengths of the radiation concerned ($\leq$ 3 mm), which requires careful use of the geometrical assumption. The upstream part of the beamline between the tokamak and the beamsplitter is composed of two elliptical focusing mirrors (f = 2.7 m, where f is the focal length) and three aluminum polished flat mirrors. The beamline optics image a point on the magnetic axis of the tokamak to an aperture at the entrance to the Michelson interferometer, and has a total length of $4f$=10.8 m. The size of aperture can vary but it has been optimized to be a 3 cm $\times$ 5 cm rectangle. The wider length of the aperture is oriented toroidally to maximize the ECE signal throughput, while the narrower length is used to limit the view near the midplane poloidally (a wide poloidal view tends to underestimate the temperatures because the same ECE frequency can also originate from colder regions off the midplane).

Thus, the emission from a narrow strip region near the midplane is well focused and collected on ECE diagnostics. At the entrance to the Michelson interferometer, there is a beamsplitter which separates X-mode and O-mode. One split beam, which is now purely O-mode, goes to the fundamental O-mode radiometer, while the other, which is purely X-mode, is further split between the Michelson interferometer, GPC and GPC2. The downstream part between the Michelson interferometer and GPC is made up of acrylic tube as a low-loss dielectric waveguide. The whole beamline is under vacuum to eliminate any water vapor absorption lines within the frequency range concerned.

2.2.1 Michelson Interferometer

A Michelson interferometer [34] is used to measure the frequency spectrum of ECE from the interference of two split beams, when one beam has variable path length. This instrument has a polarization selector and a beamsplitter to divide radiation between the moving and fixed mirrors. Unlike a conventional simple Michelson interferometer, this polarizing Michelson interferometer shows the minimum signal at a zero path difference between two split beams. The frequency upper limit is set by $c/4\delta x$, where c is the speed of light and δx is the sampling interval of the moving mirror. Since the sampling interval is 50 μm in C-Mod Michelson interferometer, the highest frequency in principle can be up to 1500 GHz. However, the practical upper limit is determined by the InSb detector efficiency, whose performance deteriorates beyond 700 GHz. The interference pattern of the two beams is Fourier-transformed to provide the frequency spectrum. Strictly speaking, it is the Fourier-transformation of the difference of the interferogram signal and its average. This instrument has been designed to provide the whole frequency spectrum (normally up to 3rd harmonic) between 100 and 1000 GHz and can obtain the temperature profile quite robustly at all toroidal fields ($\sim$ 3 to 9 T).

Considering the optical depth and higher cutoff density, the 2nd harmonic X-mode emission is preferred for electron temperature measurement. The temporal resolution (typically $\geq$ 15 msec) is limited by the frequency of mirror movement and inferior

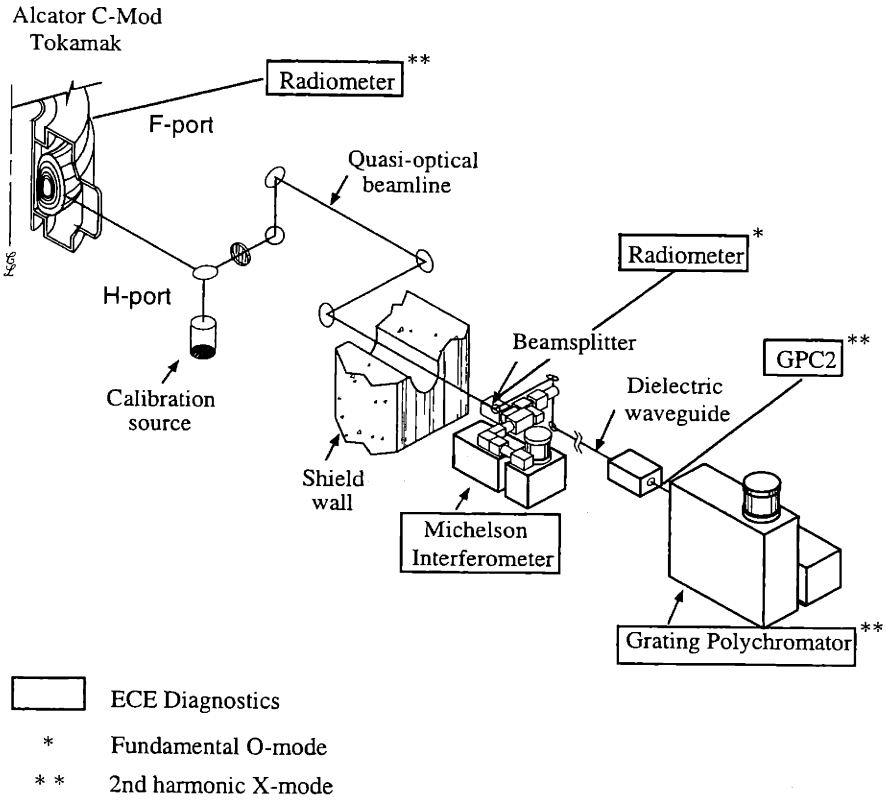

Figure 2.4: **ECE Diagnostics in Alcator C-Mod**
Four ECE diagnostics are located at H-port; Michelson interferometer (X-mode), Radiometer (fundamental O-mode), GPC (2nd harmonic ($2\Omega_{ce}$) X-mode) and GPC2 (from PPPL), while a newly installed 32 channel radiometer (2nd harmonic X-mode) is at F-port.

to other ECE diagnostics, while the spatial resolution ($\sim$ 1 cm) is comparable. The Michelson interferometer is absolutely calibrated with an in-situ black-body source. The other ECE diagnostics, whose absolute calibration is more difficult due to lower signal throughput on each channel, are cross-calibrated with the Michelson interferometer. Detailed information specific to the C-Mod Michelson interferometer can be found in Hsu's thesis [2].

2.2.2 Radiometers

In collaboration with other institutions (Auburn Univ. and Univ. of Texas), the fundamental O-mode heterodyne radiometer (110 GHz $\sim$ 128 GHz) was installed and operated from late 1997 through early 1999. The radiometer was an excellent ECE diagnostic in terms of high spatiotemporal resolutions ($\delta R \sim$ 2 to 5 mm, $\delta t \sim$2 μsec), but its use was limited to measuring the electron temperatures in low density (mostly ohmic) plasmas because the O-mode cutoff condition ($\omega = \omega_p$) is exceeded during most H-modes (See Figure 2.2).

In addition, a newly installed 32 channel 2nd harmonic X-mode radiometer [5] provided by the same groups has been operational since early 1999. This new ECE system has the capability to measure both the radial temperature profile ($T_e(R)$ at $B_T \sim$ 5 T) and in principle core temperature fluctuations ($\tilde{T_e}$), although these fluctuations have not yet been observed.

2.2.3 Grating Polychromators

Since 1994, a grating polychromator (GPC) has been a key instrument for measuring electron temperatures in C-Mod campaigns, along with the Michelson interferometer. Its moderately high resolution ($\Delta R \sim$ 9 mm FWHM, $\delta t \sim 1\mu$sec) has allowed us to observe coherent temperature fluctuations, as well as the temperature profiles, reliably. It can measure an ECE frequency range of 150 $\sim$ 600 GHz and the spacing between channels is approximately 2 cm.

The basic function of the grating is to disperse the incident beam depending on

the wavelengths. The frequency received by each detector channel is determined by the grating ruling period and incident beam angle. The grating ruling is of the same order of magnitude as the associated wavelengths and the gratings need to be changed when there is a big change in terms of operating magnetic field strength (e.g. 5.4 T $\rightarrow$ 8 T). However, for smaller changes (e.g. 5.4 T $\rightarrow$ 5.0 T), changing the incident angle without changing gratings is sufficient to reposition the ECE locations. The detectors are Indium Antimonide (InSb) bolometers. To filter out high frequency signal contamination, 15 kHz low pass filters are installed and used for routine operations sampled at 20 kHz. In some cases, the low pass filters are bypassed and the bandwidths can be increased up to 250 kHz for fast fluctuation studies. However, the signal-to-noise (S/N) ratios for the fast fluctuations are sometimes as poor as $\sim$1 because there is no appropriate filtering.

For a grating polychromator, it is necessary to consider a so-called 'order overlap' issue. In general, the first order diffracted signals are used, while the zeroth signals are reflected. However, when there are higher order grating harmonics (eg. 2nd, 3rd etc) which may reach the same detector as the first order signal, an overlap problem occurs. For example, at a GPC detector which is assigned for a first order second harmonic at R, a second order signal may also be collected, whose frequency is twice the first order signal frequency. This frequency may correspond to emission from a different radius and ECE harmonic and, without proper filtering, will contaminate the first order signal. To eliminate this, a low pass filter is installed at the entrance to the GPC, as shown in Figure 2.4. The small box between the Michelson interferometer and GPC2 represents a polarization rotator, which adjusts the polarization of the beam before it hits the rulings of the grating. The GPC diagnostic was installed by O'Shea, and further details can be found in his thesis [3].

In addition, a collaboration with PPPL enabled us to add another 19 channel polychromator (GPC2) [4] in late 1998. The combined ECE systems have the capability to measure the electron temperatures over more than half of the plasma radially. Figure 2.5 shows a typical example of the electron temperatures measured from the Michelson interferometer, GPC and GPC2, as well as core Thomson scat-

tering. Unlike GPC, GPC2 is designed to sample the data at slow ($\sim$ 5 kHz) and

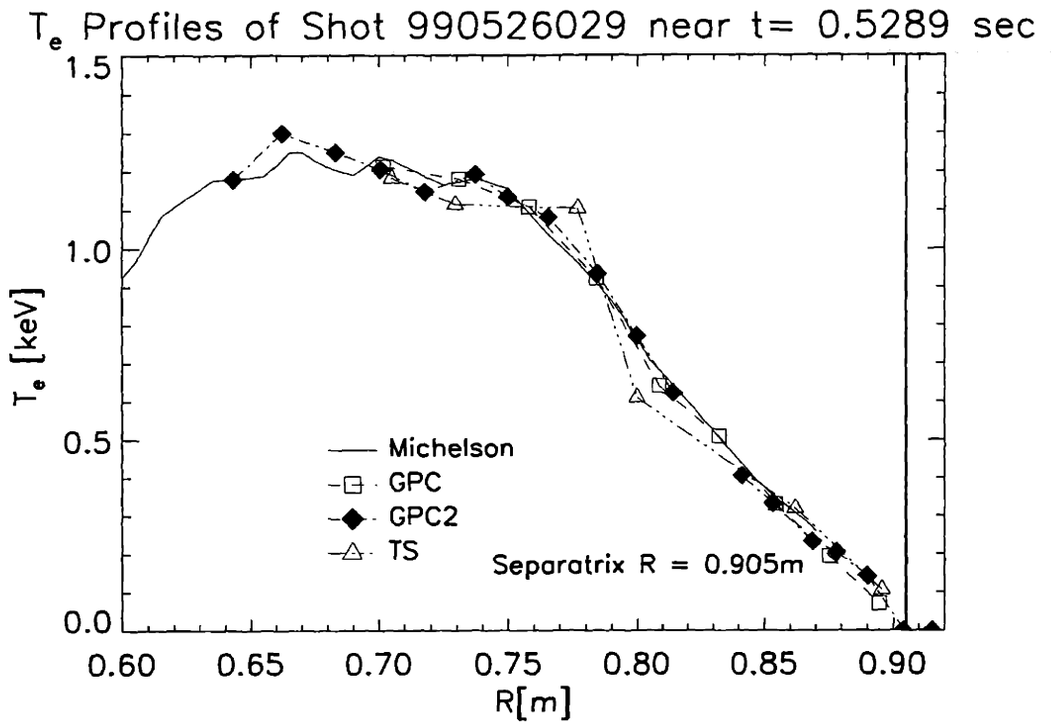

Figure 2.5: Electron temperature profiles from Michelson interferometer, GPC, GPC2 and Thomson Scattering diagnostics. Since the first three diagnostics are cross-calibrated, such good agreement is typical. The Thomson scattering data was closest available to the above time, but it was taken 18 msec earlier. Overall, the electron temperatures show good agreement among the four diagnostics.

fast ($\sim$ 50 kHz) frequencies simultaneously. The slow channels are usually used for temperature profiles and the fast ones for temperature fluctuations. As a result, if the fluctuation frequency is above the Nyquist frequency (2.5 kHz) of the slow channel, it can be observed only on the fast channels of GPC2. However, the S/N ratios of the fast GPC2 channels are rather poor, compared with those of GPC. To circumvent the poor signal-to-noise ratio problem, Fourier-transformed signals are compared because these show coherent fluctuations more clearly than the raw signals.

Chapter 3

Magnetohydrodynamics (MHD) theory

MHD theory provides a single fluid description of long wavelength, low-frequency, macroscopic plasma behavior. The governing equations for MHD theories are Maxwell's equations, mass, momentum and energy conservation equations and ohm's law. When we take $\eta \rightarrow 0$, such a model is called 'ideal' MHD theory, while when $\eta \neq 0$, it is called 'resistive' MHD theory.

In general, kinetic effects are not considered in conventional MHD theory not only because they complicate the procedures of analysis but also because most of the important macroscopic MHD phenomena have been successfully described without including the kinetic effects in the past. Nevertheless, there is some work [35] which combines kinetic theories, which were originally developed in transport physics, with the conventional MHD theory.

The purpose of this chapter is to review important MHD theories associated with the ideal and resistive modes which will be important for the next two chapters. Although the main focus is on a brief review of the ideal MHD theory, some of the resistive instabilities are also introduced.

3.1 Ideal MHD

Ideal MHD theory has been reviewed excellently by Freidberg [36], and readers are referred to his book for a more detailed discussion. For ideal MHD theory, the governing equations are derived from the Maxwell-Boltzmann equation;

$$\frac{\partial f_j}{\partial t} + \mathbf{u}\cdot\nabla f_j + \frac{q_j}{m_j}(\mathbf{E}+\mathbf{u}\times\mathbf{B})\cdot\nabla_u f_j = \left(\frac{\partial f_j}{\partial t}\right)_c. \tag{3.1}$$

Here $f_j \equiv f_j(\mathbf{x},\mathbf{v},t)$ is a distribution function for species j. Braginskii [37] showed complete derivation for fluid moments of species j from the general kinetic model. After deriving mass, momentum and energy conservation equations for electron and ion species, we may obtain a single fluid model from the two-fluid equations. Assuming no dissipation (ν=0) and isotropic plasma, the ideal MHD model[1] can be described as a single fluid in the following equations ;

continuity equation

$$\frac{\partial \rho}{\partial t} + \nabla\cdot\rho\mathbf{v} = 0 \tag{3.2}$$

equation of motion

$$\rho\frac{d\mathbf{v}}{dt} = \mathbf{j}\times\mathbf{B} - \nabla p \tag{3.3}$$

equation of state

$$\frac{d}{dt}\left(\frac{p}{\rho^\gamma}\right) = 0 \tag{3.4}$$

Ohm's law

$$\mathbf{E}+\mathbf{v}\times\mathbf{B} = \begin{cases} 0 & : \text{ ideal MHD} \\ \eta\mathbf{j} & : \text{ resistive MHD} \end{cases} \tag{3.5}$$

Faraday's law

$$\nabla\times\mathbf{E} = -\frac{\partial\mathbf{B}}{\partial t} \tag{3.6}$$

Ampere's law

$$\nabla\times\mathbf{B} = \mu_0\mathbf{j} \tag{3.7}$$

$$\nabla\cdot\mathbf{B} = 0. \tag{3.8}$$

[1]Valid for slow variations in space ($a \gg \lambda \gg r_{L_e}, r_{L_i}, \lambda_d$) and in time ($\omega \ll \Omega_{e(i)}, \omega_{pe(i)}$).

As a note, each conservation law[2] can be rewritten in a simpler form;

$$\frac{\partial}{\partial t}(density) + \nabla \cdot (flux) = 0. \tag{3.9}$$

3.1.1 Equilibrium

Most MHD studies of plasmas deal with magnetostatics, rather than dynamics, mainly because the conducting fluids are slowly varying under strong magnetic field. For a tokamak equilibrium, we also consider magnetostatic configurations. Thus, we may neglect the LHS of Eqn. 3.3 and it becomes

$$\nabla p = \mathbf{j} \times \mathbf{B}. \tag{3.10}$$

As a result, $\mathbf{B} \cdot \nabla p = \mathbf{j} \cdot \nabla p$=0, so that p is constant along $\mathbf{B}$ and $\mathbf{j}$. For the tokamak geometry shown in Figure 3.1, we may define the non-orthogonal[3] coordinates of (ψ, θ, ϕ). Thus, we may take $p = p(\psi)$ with $\mathbf{B} \cdot \nabla\psi$=0 where $\nabla p = \frac{dp}{d\psi}\nabla\psi$. Since $\mathbf{B}$[4] has both toroidal and poloidal components, we may define

$$\mathbf{B} = \mathbf{B_T} + \mathbf{B_P} = F(\psi)\nabla\phi + \nabla\phi \times \nabla\psi \tag{3.11}$$

where $F(\psi) = RB_T$ and ψ is the poloidal flux function (= -$R\hat{\phi} \cdot \mathbf{A}$). Considering axisymmetric ($\frac{\partial}{\partial\phi} = 0$) geometry, we get $\nabla \cdot \mathbf{B_T} = \frac{1}{R}\frac{\partial B_T}{\partial\phi}$=0. This requires $\nabla \cdot \mathbf{B_P}$=0 where $\mathbf{B_P} = \nabla \times \mathbf{A}$ and $\nabla \cdot \mathbf{A}$=0. Thus, the poloidal magnetic field $\mathbf{B_P}$ becomes

$$\mathbf{B_P} = -\left[\frac{\partial}{\partial z}(\hat{\phi} \cdot \mathbf{A})\right]\hat{R} + \left[\frac{1}{R}(R\hat{\phi} \cdot \mathbf{A})\right]\hat{z} \tag{3.12}$$

---

[2]For the mass conservation law, $\frac{\partial\rho}{\partial t} + \nabla \cdot \rho\mathbf{v} = 0$, where ρ is particle density and $\rho\mathbf{v}$ the particle flux.

[3]$\nabla\phi \cdot \nabla\psi = \nabla\phi \cdot \nabla\theta$=0, but $\nabla\psi \cdot \nabla\theta \neq 0$

[4]$\mathbf{B}\times\nabla\psi$=F$\mathbf{B}$ - $B^2R^2\nabla\phi$, $|\nabla\phi| = 1/R$ and $\hat{\phi} = R\nabla\phi$

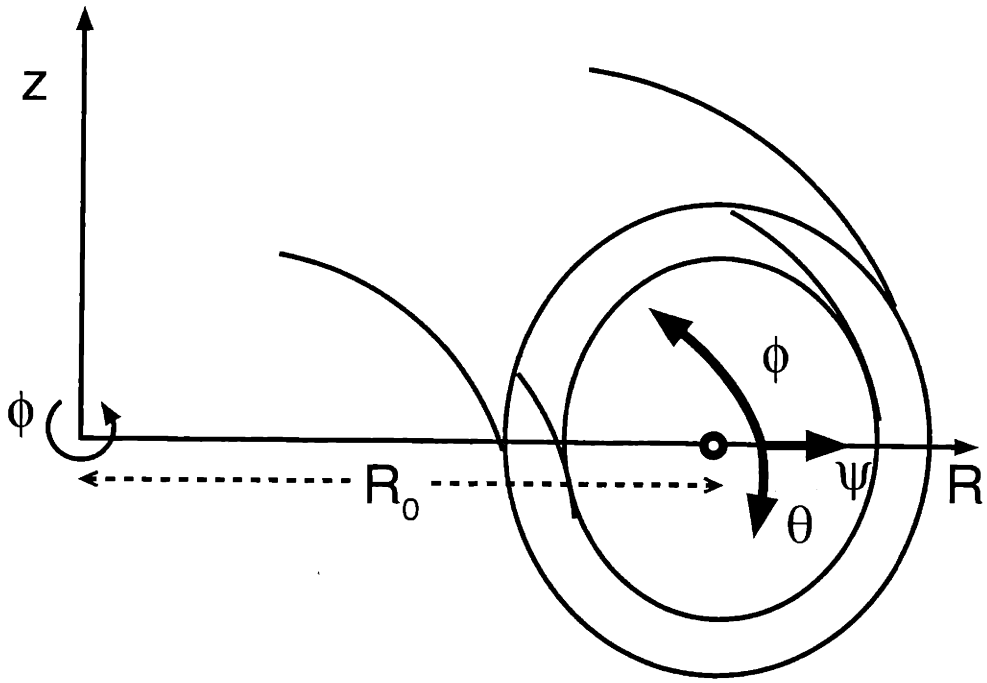

Figure 3.1: Orthogonal(R, ϕ, z) and non-orthogonal(ψ, θ, ϕ) coordinate definitions in toroidal geometry. Toroidal angle ϕ rotates in the counterclockwise direction from the top (i.e. into the paper). Using the right-handedness convention, poloidal angle θ rotates in the clockwise direction in the poloidal cross section (ie. downward arrow on the paper). Often, the directions of both the ϕ and θ coordinates are reversed without loss of generality.

Grad-Shafranov Equation

Using the above definitions and relations, we can derive the well-known Grad-Shafranov equation from Ampere's law. First, as the current density ($\mathbf{j}$) can be decomposed into components perpendicular and parallel to the magnetic field ($\mathbf{B}$), we may write it in the following form;

$$\mathbf{j} = \mathbf{j}_\perp + \mathbf{j}_\parallel \tag{3.13}$$

where $\mathbf{j}_\perp = \dfrac{\mathbf{B} \times \nabla p}{B^2} = \dfrac{1}{B^2}\dfrac{dp}{d\psi}\mathbf{B} \times \nabla\psi$ and $\mathbf{j}_\parallel = \dfrac{j_\parallel}{B}\mathbf{B}$.
After vector manipulations (as in page 57), the current density becomes

$$\mathbf{j} = -R^2\frac{dp}{d\psi}\nabla\phi - \frac{1}{\mu_0}\frac{dF}{d\psi}\mathbf{B} \tag{3.14}$$

When we take a dot-product of Ampere's law (Eqn. 3.7) with $\nabla\phi$, the RHS becomes

$$\nabla\phi \cdot (\mu_0\mathbf{j}) = -\mu_0\frac{dp}{d\psi} - \frac{dF}{d\psi}\frac{F}{R^2} \tag{3.15}$$

and the LHS becomes

$$\begin{aligned} \nabla\phi \cdot (\nabla \times \mathbf{B}) &= \nabla \cdot (\mathbf{B} \times \nabla\phi) \\ &= \nabla \cdot [|\nabla\phi|^2 \nabla\psi] \\ &= \nabla \cdot (\frac{1}{R^2}\nabla\psi) \end{aligned} \tag{3.16}$$

As a result, the Grad-Shafranov equation becomes

$$\Delta^*\psi = -\mu_0 R^2\frac{dp}{d\psi} - F\frac{dF}{d\psi} \tag{3.17}$$

where $\Delta^*\psi \equiv R^2\nabla \cdot (\dfrac{1}{R^2}\nabla\psi) = R\dfrac{\partial}{\partial R}\dfrac{1}{R}\dfrac{\partial\psi}{\partial R} + \dfrac{\partial^2\psi}{\partial z^2}$. In addition, B_R and B_z can be found in terms of cylindrical coordinates;

$$B_R = -\frac{1}{R}\frac{\partial\psi}{\partial z}, \qquad B_z = \frac{1}{R}\frac{\partial\psi}{\partial R}. \tag{3.18}$$

The Grad-Shafranov equation needs to be solved for further physical analysis because most plasma parameters are described in terms of ψ coordinates. For this purpose, the EFIT[38] program is used as a reconstruction program in Alcator C-Mod. It is run routinely for all C-Mod discharges on a 20 msec time base to provide not only the reconstructed flux surface but also various physical quantities on the basis of experimental data, primarily magnetics. In special cases, EFIT can be run manually with additional constraints of pressure (p) and/or current density(j) or on a faster time base.

3.1.2 Stability

Once we have established an equilibrium, we need to determine whether the equilibrium is stable or unstable. If the plasma is perturbed from its state, the resulting perturbing forces either push the plasma back to the original equilibrium (stable) or diverge to an escalating fluctuation (unstable). Generally, an ideal MHD instability is so critical and disastrous that it must be avoided. Most ideal MHD studies are based on linear stability analysis, which is often adequate for practical situations. The key features associated with the linear stability theory will be reviewed here.
Assuming that Q represents any quantity of interest, it can be linearized as

$$\mathbf{Q}(\mathbf{x},t) = \mathbf{Q_0}(\mathbf{x}) + \mathbf{Q_1}(\mathbf{x},t) \tag{3.19}$$

where $\mathbf{Q_0}(\mathbf{x})$ is the equilibrium value and $|\mathbf{Q_0}| \gg |\mathbf{Q_1}|$. $\mathbf{Q_1}(\mathbf{x},t)$ can be written as

$$\mathbf{Q_1}(\mathbf{x},t) = \mathbf{Q_1}(\mathbf{x}) \exp(-\imath\omega t). \tag{3.20}$$

Thus, the imaginary part of the eigenfrequency $\omega = \omega_R + \imath\gamma$ determines the stability:

$$Im(\omega) = \gamma \begin{cases} > 0 & : \text{ unstable} \\ < 0 & : \text{ stable} \end{cases} \tag{3.21}$$

So far, nonlinear analysis has not been done as much, mainly because it is much more complicated than linear analysis. However, nonlinear analysis needs to be employed for some MHD instabilities which have not been explained in the framework of linear stability theory.

Ideal Stability

When we linearize the ideal MHD equations [page 56] by introducing a linear displacement vector $\boldsymbol{\xi}(\mathbf{x},t)$ such that $\dfrac{\partial \boldsymbol{\xi}}{\partial t} = \mathbf{v_1}$, the first order linearized MHD equations are

$$\left.\begin{aligned} \rho_1 &= -\nabla\cdot(\rho_0\boldsymbol{\xi}) \\ p_1 &= -\boldsymbol{\xi}\cdot\nabla p_0 - \gamma p_0 \nabla\cdot\boldsymbol{\xi} \\ \mathbf{B_1} &= \nabla\times(\boldsymbol{\xi}\times\mathbf{B_0}) \\ \mathbf{j_1} &= \frac{1}{\mu_0}\nabla\times\mathbf{B_1} \\ &= \frac{1}{\mu_0}\nabla\times[\nabla\times(\boldsymbol{\xi}\times\mathbf{B_0})]\,. \end{aligned}\right\} \tag{3.22}$$

Thus, the momentum equation becomes

$$\begin{aligned} \rho_0\frac{\partial^2\boldsymbol{\xi}}{\partial t^2} &= \frac{1}{\mu_0}\{\nabla\times[\nabla\times(\boldsymbol{\xi}\times\mathbf{B_0})]\}\times\mathbf{B_0} + \frac{1}{\mu_0}(\nabla\times\mathbf{B_0})\times[\nabla\times(\boldsymbol{\xi}\times\mathbf{B_0})] \\ &\quad +\nabla(\boldsymbol{\xi}\cdot\nabla p_0 + \gamma p_0\nabla\cdot\boldsymbol{\xi}) \\ &\equiv F(\boldsymbol{\xi}) \end{aligned} \tag{3.23}$$

where $\mathbf{F}(\boldsymbol{\xi})$ is the linear force operator. Considering the self-adjointness[5] of the $\mathbf{F}(\boldsymbol{\xi})$ operator, the second order perturbed potential energy $W_2[\boldsymbol{\xi}]$ is given by

$$W_2[\boldsymbol{\xi}] = -\frac{1}{2}\int_p d^3\mathbf{x}\boldsymbol{\xi}\cdot\mathbf{F}(\boldsymbol{\xi}) \tag{3.24}$$

Normal mode formulation Supposing that $\boldsymbol{\xi}_n(\mathbf{x})$ is an eigenfunction of the operator $-\dfrac{1}{\rho_0}\mathbf{F}$, we may take advantage of the self-adjointness of the operator, whose

[5]For self-adjointness, $<\boldsymbol{\eta}|\mathbf{F}\boldsymbol{\xi}> = <\mathbf{F}\boldsymbol{\eta}|\boldsymbol{\xi}>$. Here $<\mathbf{A}|\mathbf{B}>$ represents the inner product of the two vectors, $\mathbf{A}$ and $\mathbf{B}$.

eigenfunctions are orthogonal and eigenvalues ω_n^2 are real.

$$-\frac{1}{\rho_0}\mathbf{F}[\boldsymbol{\xi}_\mathbf{n}(\mathbf{x})] = \omega_n^2 \boldsymbol{\xi}_\mathbf{n}(\mathbf{x}) \tag{3.25}$$

Thus, if $\omega_n^2 > 0$, the mode is stable, while if $\omega_n^2 < 0$, unstable. Such a condition is necessary for stability but it is not sufficient because the set of eigenfunctions $\{\boldsymbol{\xi}_n\}$ does not span the whole space of physically allowable motions. This formulation is called the 'normal mode' approach.

Variational Formulation The dot product of Eqn 3.23 with $\boldsymbol{\xi}^*$ and its integration over the plasma volume yields the variational form of the normal mode equation;

$$\omega_n^2 = \frac{W_2[\boldsymbol{\xi}_n]}{N_2[\boldsymbol{\xi}_n]} \tag{3.26}$$

where $N_2[\boldsymbol{\xi}_n] = \frac{1}{2}\int_p d_\mathbf{x}^2 \rho_0 |\boldsymbol{\xi}_n(\mathbf{x})|^2$ is the functional associated with kinetic energy. This variational formulation is equivalent to the normal mode approach because of the self-adjointness of $\mathbf{F}$. In fact, if we define a functional as $\Omega^2[\boldsymbol{\xi}] = \frac{W_2[\boldsymbol{\xi}]}{N_2[\boldsymbol{\xi}]}$, the eigenvalues of ω_n^2 are the extrema [6] of Ω^2 and its extremizing functions are the corresponding eigenfunctions $\boldsymbol{\xi}_n$.

Energy Principle Based on the fact that the energy is conserved in the ideal MHD model, the sign of $W_2[\boldsymbol{\xi}]$ determines the stability of a system according to the 'energy principle'. That is, if the minimum value of the potential energy for all allowable displacements is positive, the plasma is stable. If it is negative for any displacement, it is unstable. This stability criterion is more powerful than the normal mode approach because there is no need to calculate the normal mode eigenfrequencies. However, direct application of this energy principle to a system with a vacuum region is not trivial mainly because $\boldsymbol{\xi}$ is not defined in the vacuum region, whose contribution to $\mathbf{F}$ is implicit. This difficulty can be circumvented by applying the energy principle

[6] $\frac{\delta\Omega^2}{\delta\xi}|_{\xi = \xi_n} = 0$ at extrema

up to the plasma surface and considering the vacuum region explicitly. Now, the potential energy of a system is composed of three parts; plasma, surface and vacuum contributions

$$W_2[\boldsymbol{\xi}] = W_{2P}[\boldsymbol{\xi}] + W_{2S}[\boldsymbol{\xi}] + W_{2V}[\boldsymbol{\xi}] \tag{3.27}$$

where

$$\begin{aligned} W_{2P}[\boldsymbol{\xi}] &= \frac{1}{2}\int_P d^3\mathbf{x}\left\{\frac{1}{\mu_0}|\mathbf{B_1}|^2 + \gamma p_0(\nabla\cdot\boldsymbol{\xi})^2 + \boldsymbol{\xi}_\perp\cdot(\mathbf{B_1}\times\mathbf{j_0})\right. \\ &\quad \left.+(\boldsymbol{\xi}_\perp\cdot\nabla p_0)(\nabla\cdot\boldsymbol{\xi}_\perp)\right\} \end{aligned} \tag{3.28}$$

$$W_{2S}[\boldsymbol{\xi}] = \frac{1}{2}\int_S d\mathbf{S}(\boldsymbol{\xi}\cdot\hat{\mathbf{n_0}})^2[\hat{\mathbf{n_0}}\cdot\nabla(\frac{B_{0V}^2}{2\mu_0} - \frac{B_0^2}{2\mu_0} - p_0)] \tag{3.29}$$

$$W_{2V}[\boldsymbol{\xi}] = \int_V d^3\mathbf{x}\frac{B_{1V}^2}{2\mu_0}. \tag{3.30}$$

This is referred to as the "extended form of the energy principle". A noticeable difference of the extended form is that only the normal components (i.e. $\boldsymbol{\xi}_\perp$) to the magnetic field remain to be considered except for the compressional term. When the plasma volume integral $W_{2P}[\boldsymbol{\xi}]$ (Eqn. 3.28) [7] is expressed in a more physically intuitive form, each contribution can be recognized rather easily as either stabilizing

[7] Let $\mathbf{B_1} = \mathbf{B_{1\parallel}} + \mathbf{B_{1\perp}}$ and $\mathbf{j_1} = \mathbf{j_{1\parallel}} + \mathbf{j_{1\perp}}$, so $|\mathbf{B_1}|^2 = |\mathbf{B_{1\perp}}|^2 + |\mathbf{B_{1\parallel}}|^2$.
From the third term of Eqn. 3.28, $\boldsymbol{\xi}_\perp\cdot(\mathbf{B_1}\times\mathbf{j_0}) = \boldsymbol{\xi}_\perp\cdot(\mathbf{B_{1\parallel}}\times\mathbf{j_{0\perp}} + \mathbf{B_{1\perp}}\times\mathbf{j_{0\parallel}})$.
Meanwhile, $\mathbf{B_{1\parallel}} = [\frac{\mu_0}{B_0^2}(\boldsymbol{\xi}_\perp\cdot\nabla p_0) - (\nabla\cdot\boldsymbol{\xi}_\perp) - 2(\boldsymbol{\xi}_\perp\cdot\boldsymbol{\kappa})]\mathbf{B_0}$ where $\boldsymbol{\kappa} \equiv (\frac{\mathbf{B_0}}{B_0}\cdot\nabla)(\frac{\mathbf{B_0}}{B_0})$: curvature vector.
As $\boldsymbol{\xi}_\perp\cdot(\mathbf{B_{1\parallel}}\times\mathbf{j_{0\perp}}) = -(\boldsymbol{\xi}_\perp\cdot\nabla p_0)\left[\frac{\mu_0}{B_0^2}(\boldsymbol{\xi}_\perp\cdot\nabla p_0) - (\nabla\cdot\boldsymbol{\xi}_\perp) - 2(\boldsymbol{\xi}_\perp\cdot\boldsymbol{\kappa})\right]$, the parallel component of the first term, the perpendicular current contribution of the third term and the last term from Eqn. 3.28 can be rewritten as

$$\begin{aligned} &\frac{1}{\mu_0}|\mathbf{B_{1\parallel}}|^2 + \boldsymbol{\xi}_\perp\cdot(\mathbf{B_{1\parallel}}\times\mathbf{j_{0\perp}}) + (\boldsymbol{\xi}_\perp\cdot\nabla p_0)(\nabla\cdot\boldsymbol{\xi}_\perp) \\ = &\frac{B_0^2}{\mu_0}[(\nabla\cdot\boldsymbol{\xi}_\perp) + 2(\boldsymbol{\xi}_\perp\cdot\boldsymbol{\kappa})]^2 - 2(\boldsymbol{\xi}_\perp\cdot\nabla p_0)(\boldsymbol{\xi}_\perp\cdot\boldsymbol{\kappa}) \end{aligned}$$

Hence, the intuitively apprehensible form (Eqn. 3.31) is obtained.

or destabilizing.

$$W_{2P}[\boldsymbol{\xi}] = \frac{1}{2}\int_P d^3\mathbf{x}\left\{ \overbrace{\frac{1}{\mu_0}|\mathbf{B}_{1\perp}|^2}^{\text{Shear Alfven (magnetic field bending)}} + \overbrace{\frac{B_0^2}{\mu_0}[(\nabla\cdot\boldsymbol{\xi}_\perp)+2(\boldsymbol{\xi}_\perp\cdot\boldsymbol{\kappa})]^2}^{\text{Compressional Alfven (magnetic compression)}} + \overbrace{\gamma p_0(\nabla\cdot\boldsymbol{\xi})^2}^{\text{Sound wave (fluid compression)}} \right.$$

$$\left. \underbrace{-2(\boldsymbol{\xi}_\perp\cdot\nabla p_0)(\boldsymbol{\xi}_\perp\cdot\boldsymbol{\kappa})}_{\substack{\nabla p \text{ instability} \\ \text{(ballooning, interchange)}}} + \underbrace{\boldsymbol{\xi}_\perp\cdot(\mathbf{B}_{1\perp}\times\mathbf{j}_{0\parallel})}_{\substack{j_\parallel \text{ instability} \\ \text{(kink)}}} \right\} \tag{3.31}$$

where $\parallel$ and $\perp$ are the parallel and perpendicular components to the magnetic field respectively and the curvature vector κ is defined as in the footnote of rewriting the plasma volume integral $W_{2P}[\boldsymbol{\xi}]$. The first three terms (shear Alfvén, compressional Alfvén, sound wave) are positive, so they are stabilizing. The sign of the fourth term is determined by the direction of ∇p with respect to the curvature vector $\boldsymbol{\kappa}$, while the last term can also be negative due to $j_\parallel$. Thus, we can clearly see that there are two types of instability in terms of sources, 'pressure-driven' and 'current-driven' modes. Typically, ballooning and interchange modes are classified as the pressure-driven types, while kink modes are current-driven. For the pressure-driven interchange modes, whether the so called 'good curvature (∇p_0 and κ are antiparallel)' region is bigger than the 'bad curvature ((∇p_0 and κ parallel)' region or not determines the stability. However, when the β increases, such a globally-averaged quantity is no longer sufficient, and a local stability condition becomes important. When the plasma is unstable, MHD activity is localized in the low field side, which is the 'bad curvature' region. This is the so called 'ballooning' mode. For the current-driven modes, the MHD fluctuations move in and out at an unstable flux surface continuously, which appears as "kinking" in experimental observations. When resistivity is involved in this mechanism, the mode becomes a 'tearing' mode. For marginal cases, it can also be called a 'resistive kink'.

In summary, the ideal MHD tokamak instabilities can be classified, as shown in Table 3.1.

Mode number	$n = 0$	$n = 1$	$n = 2, 3, \cdots$	n $\gg 1$
low β	internally stable but externally axisymmetric mode	current-driven kink interchange mode	generally stable, if $n = 1$ stable and $n \gg 1$ stable	interchange mode
high β		current and pressure-driven kink-ballooning		ballooning mode

Table 3.1: Classification of ideal MHD tokamak instabilities

3.2 Resistive instability

Considering a finite resistivity $\eta \neq 0$ in Ohm's law (Eqn 3.5), the ideal MHD equations in Section 3.1 may be modified for resistive stability studies. Hence, the perturbed linearized Ohm's law becomes

$$\begin{aligned} \frac{\partial \mathbf{B_1}}{\partial t} &= \nabla \times (\mathbf{v_1} \times \mathbf{B_0}) - \frac{\eta}{\mu_0}\{\nabla \times (\nabla \times \mathbf{B_1})\} \\ &= \nabla \times (\mathbf{v_1} \times \mathbf{B_0}) + \frac{\eta}{\mu_0}\nabla^2 \mathbf{B_1}. \end{aligned} \tag{3.32}$$

The second term of the RHS of Eqn 3.32 contains the finite resistivity of the plasma and allows us to investigate the resistive instabilities. From a physical point of view, it represents the diffusion of magnetic field lines through plasma and its characteristic time is the so-called 'resistive diffusion time', τ_R ($\equiv \frac{\mu_0 a^2}{\eta}$). The shortest characteristic time in the plasma is of the order of the 'Alfvén time', τ_A ($\equiv \frac{R}{v_A}$, where $v_A = \frac{B_0}{\sqrt{\mu\rho}}$), while the longest time is of the order of τ_R. Thus, the Lundquist Number (or magnetic Reynolds number) $S_0 (\equiv \frac{\tau_R}{\tau_A})$ is used for characterizing the plasma. For typical tokamak plasmas, S_0 is on the order of 10^6 to 10^8, so the resistive diffusion time and the Alfvén time are well separated. As a rule of thumb, a typical MHD characteristic time is on the order of the geometric mean of τ_R and τ_A and an ideal MHD characteristic time is faster than that of resistive MHD. For typical C-Mod conditions ($T_e \sim 2$ keV, $n_e \sim 1.0 \times 10^{20} m^{-3}$, and B_0=5.4 T), τ_R is 5.6 sec, $\tau_A \approx 0.8 \times 10^{-8}$ sec and a typical MHD characteristic time is 0.2 msec.

To distinguish the resistive instabilities from ideal MHD, the MHD modes are called resistive ballooning, resistive interchange, resistive kink, and tearing modes etc. Since

the general expressions regarding the resistive MHD model need mathematically intensive procedures, the reader is referred for detailed information to the references [36, 39, 40, 41, 42, 43, 44, 45]. However, in the next chapter, detailed descriptions of a few resistive modes will be given in order to compare experimental observations with theoretical predictions.

Chapter 4

Resistive modes during current ramp discharges

In general, the resistive MHD solutions with non-zero η do not converge to the solutions of ideal MHD, as η goes to 0 [46]. This is because the resistive MHD equations, which have higher order terms proportional to the resistivity, require more boundary conditions than ideal MHD equations. Compared to ideal MHD constraints, such higher order terms of resistive MHD equations relax imposed constraints and allow for certain motions which are not possible when η=0. Meanwhile, the analysis of the resistive MHD is heavily dependent on ideal MHD solutions. For example, when we think of a 'magnetic island' which is located in a non-ideal layer, the ideal MHD solutions outside the layer are used for determining the Δ'[1].

Without exception in stability analysis, ideal instability is checked first. Then, if nothing is unstable in terms of the ideal MHD stability, we continue to investigate whether the system is stable with respect to the resistive MHD instability. As mentioned in the previous chapter, most of the stability criteria are based on linear analysis. Thus, even if a system is stable in both terms of ideal and resistive linear analyses, it can be unstable when nonlinear terms are considered. Therefore, linear analysis always has its limitations for determining MHD stability.

[1]This is defined as $\Delta' \equiv (\frac{\psi'}{\psi})|_{r_s-w/2}^{r_s+w/2}$, where r_s and w are the location and width of a magnetic island respectively. In classical theory, it is unstable, if $\Delta' > 0$.

In this chapter, the general MHD activity observed during current ramp discharges will be described. Some detailed analyses will then be presented regarding two types of $n = 1$ resistive modes; **resistive "multiple" tearing mode and resistive interchange mode**. The former has been identified during reversed shear experiments. Since reversed shear plasma is considered as an advanced operation scenario [17], the identification of the resistive "multiple" tearing mode warns us of its potential adverse effect which should not be neglected in terms of plasma performance. The interchange mode was predicted theoretically long time ago [45], while the experimental observation was made in DIII-D group recently [47]. However, the resistive interchange mode in DIII-D was reported to be due to high β. In contrast, the prediction of a resistive interchange mode in Alcator C-Mod was made during current ramp-up, when β is low. The instability mechanism has been clearly explained to be due to inverted pressure gradient with $q > 1$, not to high β.

4.1 MHD activity during current ramp-up

During current ramp-up, a reversed magnetic configuration is usually created because the current diffusion time τ_R [page. 65] is much longer than the plasma current rise time. In other words, the skin currents which are formed at the plasma edge initially are not permeated into the core. Moreover, if the plasma is heated up by early auxiliary heating, it retards the current diffusion because τ_R increases proportionally to $T_e^{3/2}$ [2]. In this case, the reversed shear plasma with auxiliary heating can be maintained longer than without additional heating. This explains a fundamental idea of how to obtain a reversed shear plasma through early ICRF launching during C-Mod current ramp [22, 23]. Regarding the current ramp-up rate, many people had thought that faster current rise would be more likely to be unstable. However, based on almost 400 shots from December 1997 through January 1998 in C-Mod runs, there was no correlation between current ramp-up rates and MHD events, as shown in Figure 4.1. MHD activity was rarely observed in the lower and higher current

[2] $\tau_R \propto \eta^{-1} \propto T_e^{3/2}$

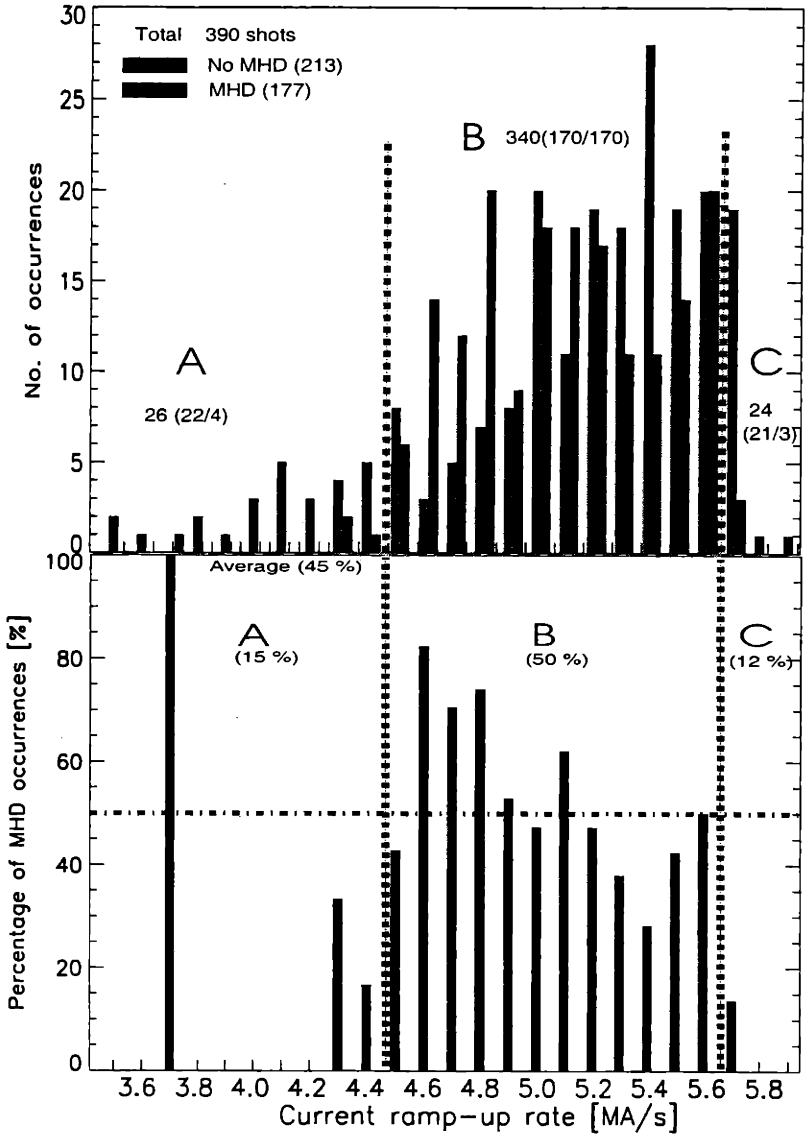

Figure 4.1: Top: MHD occurrences vs current ramp-up rate ($\Delta I_p/\Delta t$). Region A (low $\Delta I_p/\Delta t$) and Region C (high $\Delta I_p/\Delta t$) are equally stable (i.e. no MHD dominated). In Region B (moderate $\Delta I_p/\Delta t$), it seems to be fair to say that lower $\Delta I_p/\Delta t$ (≤ 5.1 MA/s) is slightly more unstable than higher $\Delta I_p/\Delta t$. Overall, faster current ramp-up rates did not show any tendency to lead to more frequent MHD occurrences. Bottom: Percentage of MHD occurrences vs current ramp-up rate.

ramp-up rates (Region A and C), while it occurred in about half the discharges with the moderate current ramp-up rates (Region B). Considering that a typical current ramp-up rate of C-Mod is 5.0 MA/s, detailed analysis shows that slightly lower ramp-up rates are, if anything, slightly more likely to have MHD events than higher ones in the typical range of current ramp-up rates (eg. Region B), which contradicts the previous perception. Interestingly, when electron temperature profile was hollow, MHD activity seemed to occur easily in the core, compared with the case of monotonic T_e profile. The comparison of Figures 4.2 and 4.3 is a good example. The five time-traces from the top in both figures are electron temperatures of GPC innermost channels and the other traces are from other diagnostics. In Figure 4.2, no MHD activity is observed on the ECE core channels and T_e profile is monotonic during the current ramp discharge, although monotonic T_e profile is not sufficient for stability. Meanwhile, in Figure 4.3, various MHD events are shown on the T_e traces and we can clearly see all the T_e profiles are hollow [See Figure 4.4] during the otherwise similar current ramp discharge. In fact, for the dataset with 5.0 MA/s, there were 3 shots which had hollow temperature profiles and all of them showed MHD fluctuations in the core, while the rest of the shots had monotonic temperature profiles, in which half of them showed MHD activity that is located mostly at the edge. This observation suggests that nonmonotonic temperature (or pressure) may play a significant role in core MHD instabilities during current ramp-up.

4.1.1 Types of MHD activity observed during current ramp-up

As mentioned earlier, various MHD events occurred during non-monotonic T_e profile stages. Figure 4.4 shows the T_e profiles corresponding to each MHD event in Figure 4.3, as well as to a monotonic case. Clearly, until the T_e profile becomes monotonic, the current ramp-up discharge with hollow T_e profile is accompanied by various MHD events.

Based on Figure 4.3, three types of MHD events may be distinguished phenomeno-

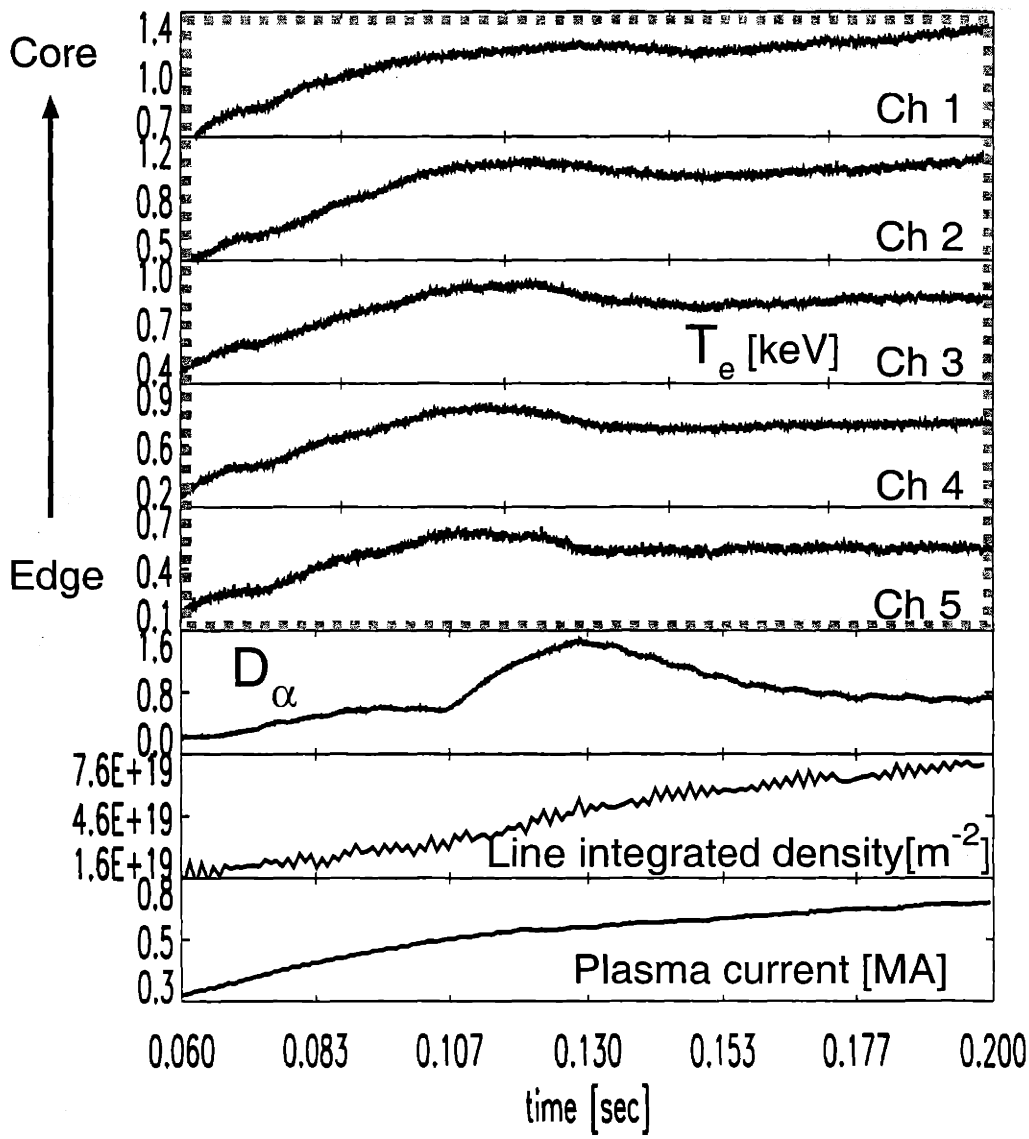

Figure 4.2: Typical current ramp discharge without MHD activity. The T_e profile is monotonic at all times.

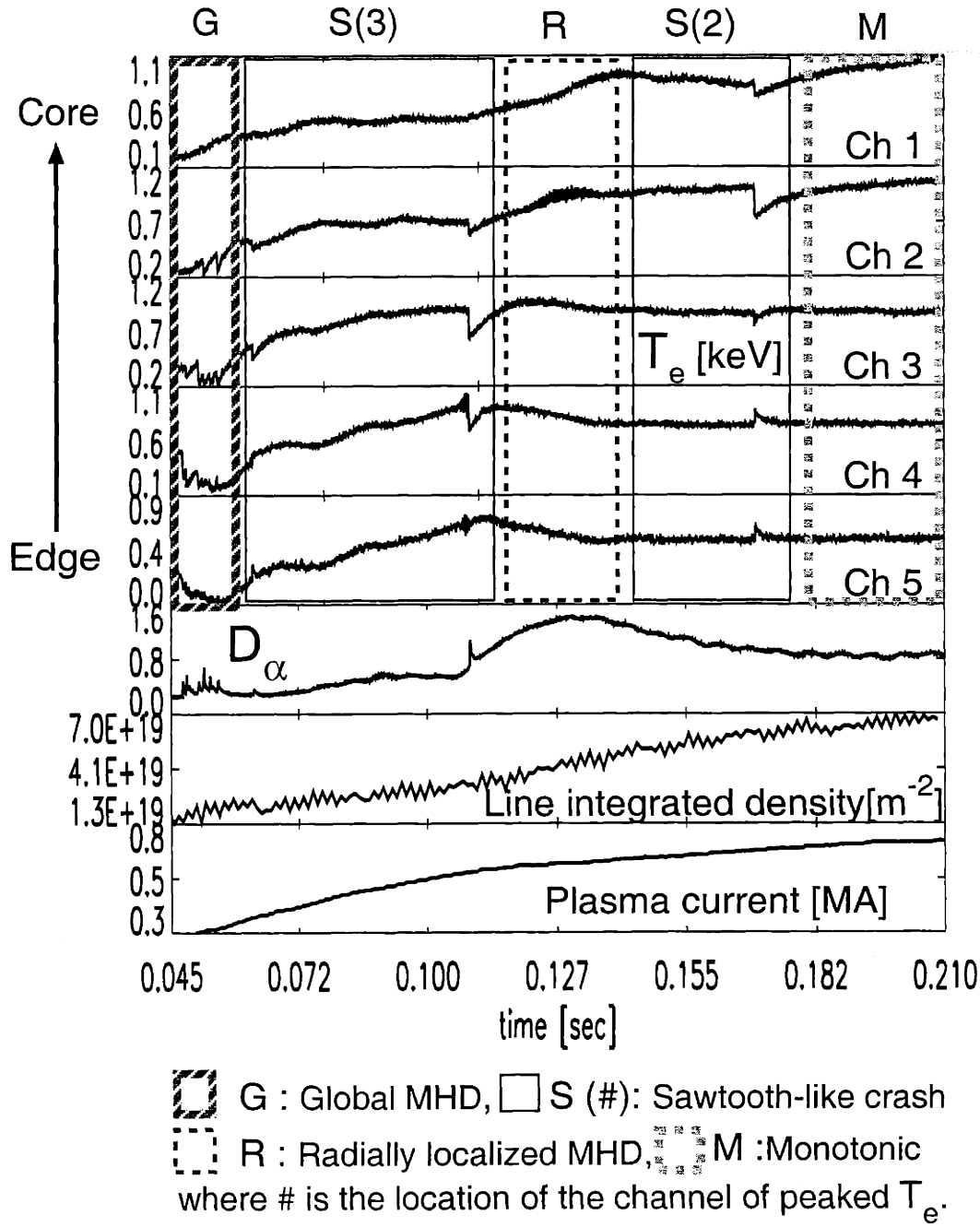

Figure 4.3: Classifications of various MHD events during current ramp discharge. Note that there is no more MHD after 180 msec, when T_e profile becomes monotonic. During the global MHD, the signal looks "sawtooth-like", but there are no inverted sawtooth-like signals on edge channels. In fact, the plasma was nearly terminated.

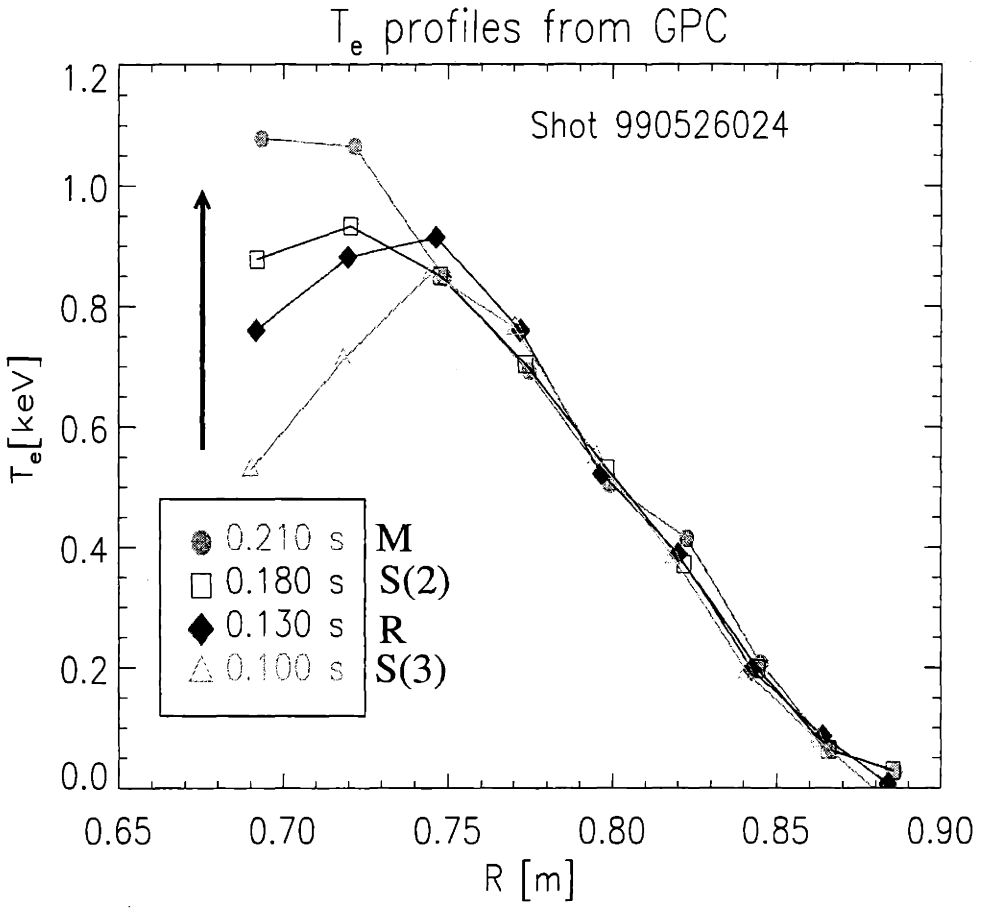

Figure 4.4: Electron temperature (T_e) profiles based on Figure 4.3.

logically; global MHD (G), sawtooth-like crash (S), localized MHD (R) [3]. Regarding the global MHD (G), nearly the whole plasma was perturbed, but did not go to a disruption. Sometimes such global MHD activity sinusoidally evolves, saturates and then decays. In the next section, this type of global mode will be analyzed in detail and is shown to be a **resistive "multiple" tearing mode**. The sawtooth-like crash (S), it is not a typical sawtooth whose q_0 is ≤ 1. In most C-Mod plasmas, sawtooth crashes occur later than 250 msec. Thus, the sawtooth-like crashes, which occurred earlier than 200 msec, are of different origin, because $q_0 > 1$. Unfortunately, there is no model to explain this phenomenon and it is not a focus of this chapter. However, there are some relevant theories which may provide important insights [48]. Lastly, the localized MHD (R) activity is an infrequently observed MHD event in C-Mod, probably because it is so highly localized that present diagnostic resolutions are challenged. It has been explained well in terms of **ideal interchange mode**, which will be discussed in the next chapter. The observations will also be compared with the resistive interchange mode, which had been predicted to be unstable for some other plasmas [23].

4.1.2 Kinetic EFIT and ECE positions during current ramp

Before describing further analysis of the current ramp-up MHD activity, an EFIT-related issue should be mentioned. The routine EFIT, which is run automatically every 20 msec, does not provide reliable information during current ramp stages. This is because the q_0 in routine EFIT is always fixed near 1, which is true for most steady tokamak plasmas but is not for current ramp plasmas whose q_0 is much higher than 1. Thus, all the equilibria during the current ramp discharges need to be found individually with an adjusted q_0 constraint in EFIT (eg. 4 or 5, rather than 1). The so called "kinetic EFIT" accommodates not only the q_0 adjustment but also additional constraints (eg. pressure). Thus, all the equilibria which are discussed here are based on the kinetic EFIT, unless otherwise specified. Hence, the positions of ECE diagnostics also need to be found based on the kinetic EFIT runs. In general, the total

[3]For convenience, no MHD activity period with monotonic T_e profile has been labeled with "M".

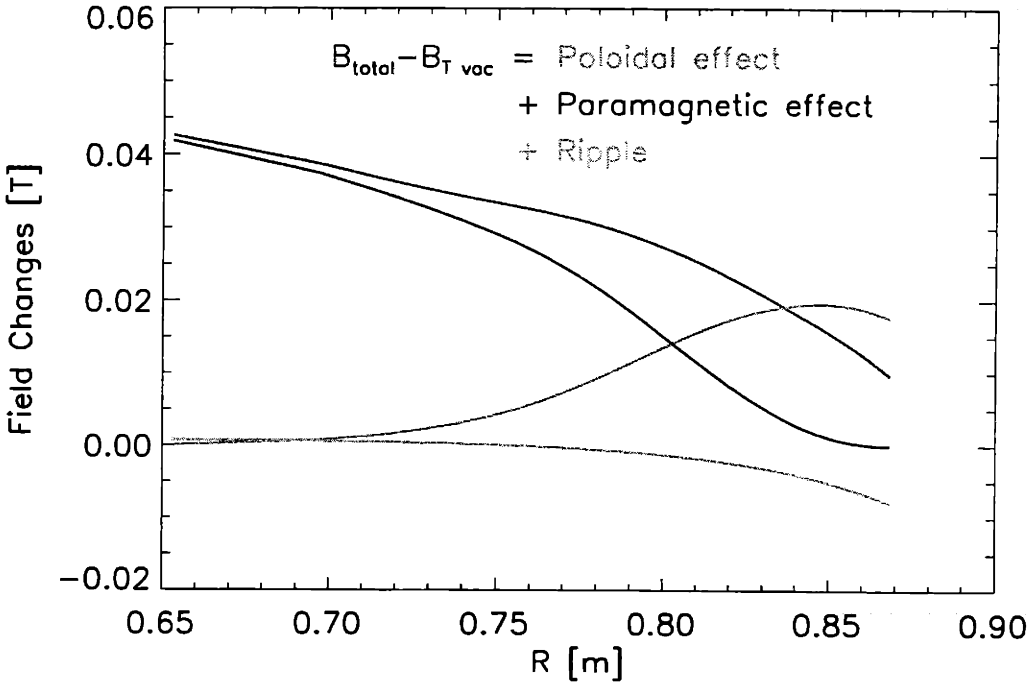

Figure 4.5: Components for total magnetic field changes

magnetic field B_{total} is composed of four physically meaningful contributions [4] shown in Figure 4.5; toroidal field (B_T), poloidal field (B_P), diamagnetic (or paramagnetic) effects, and ripple effects.

Since the toroidal and poloidal flux functions (F and ψ) are obtained based on the EFIT reconstruction, the use of kinetic EFIT, instead of routine EFIT, affects the ECE position determination (recall that the electron cyclotron frequency is dependent on the total magnetic field [See page. 41]). For the exact ECE positions during current

[4]Compared with vacuum toroidal magnetic field B_{Tvac}, the total magnetic field B_{total} is calculated by

$$\begin{aligned} B_{total} - B_{Tvac} &= \{(B^*_{total} + B_{ripple}) - B_T\} + (B_T - B_{Tvac}) \\ &= (B^*_{total} - B_T) + (B_T - B_{Tvac}) + B_{ripple} \\ &= \underbrace{(\sqrt{B_T^2 + B_P^2} - B_T)}_{\text{poloidal effect}} + \underbrace{(B_T - B_{Tvac})}_{\substack{\text{paramagnetic} \\ \text{(or diamagnetic) effect}}} + B_{ripple} \end{aligned}$$

where B^*_{total} is the total magnetic field without ripple effect.
The ripple field B_{ripple} consideration is necessary because the outer spacing between two adjacent toroidal magnets is much larger than the inner spacing in tokamaks. Thus, there are slight field changes major-radially.

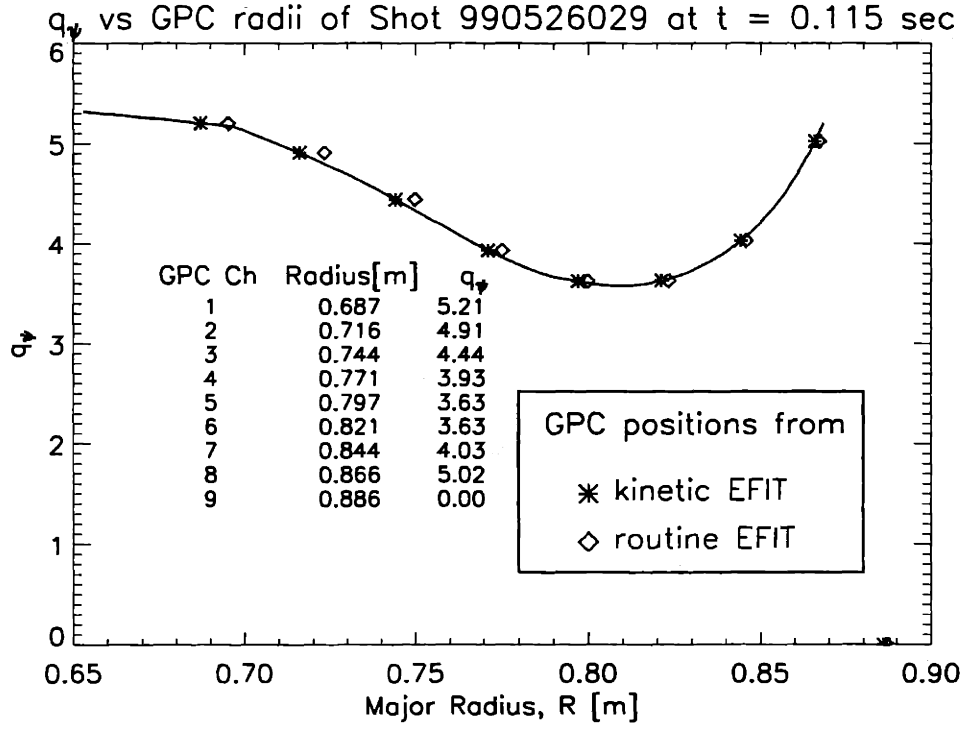

Figure 4.6: GPC position differences of kinetic ($*$) and routine ($\diamond$) EFITs. In this example, an equilibrium with hollow q-profile has been reconstructed using kinetic EFIT, on which each channel ($*$) of GPC has been located. Hence, the locations ($\diamond$) based on routine EFIT (with monotonic q-profile ($q_0 \sim 1$)) might have been miscalculated. Especially, such shifts as 3$\sim$8 mm for some inner channels are not insignificant.

ramp stages, $3 \sim 8$ mm inward shifts are usually found based on a kinetic EFIT which produces a hollow q-profile, compared with the counterparts based on a routine EFIT whose q-profile is monotonic (See Figure 4.6). Considering that the spatial resolution of the GPC diagnostic is ~ 9 mm, such shifts cannot be neglected.

4.2 Resistive "multiple" tearing mode in reversed shear plasmas

Reversed magnetic shear profiles are predicted to have better performance [18] in terms of confinement, stability and self-sustaining bootstrap currents. Many experiments have since verified such predictions in various tokamaks [19, 20, 21]. In particular, in the negative central magnetic shear (NCS) region, the plasma shows excellent stability to the $n = \infty$ ideal MHD ballooning mode [49]. However, when reversed magnetic shear plasmas are accompanied by MHD fluctuations, plasma performance is reduced. Understanding the characteristics of the MHD activity associated with reversed magnetic shear plasmas is required prior to adopting reversed magnetic shear operation as an advanced tokamak operation scenario [17, 50].

A resistive MHD mode specific to reversed magnetic shear plasmas is a resistive double tearing mode, which can be destabilized when a pair of rational surfaces with the same q are close to each other. Since it is a global mode, it can be observed in experiments rather easily. For a single tearing mode [40, 43, 44], in a classical tearing theory, $\Delta' > 0$ is an unstable condition with magnetic island width (w) centered at r=r_s [See page. 67]. In a neoclassical theory, even negative Δ' can be unstable in that transport and polarization terms should be also considered [51]. On the other hand, for a double tearing mode [52, 53, 54, 55, 56], we do not have a similarly simple analytic criterion.

4.2.1 Experimental Observation

To achieve high performance reversed magnetic shear plasmas in Alcator C-Mod [22, 23], ICRF heating is added to early ohmic plasmas as its auxiliary power, unlike most other tokamaks whose main power source is neutral beam injection (NBI). As mentioned above, the additional heating raises the plasma temperature T_e and so the current diffusion is retarded further as the total input power goes up (Recall that τ_R is proportional to $T_e^{3/2}$). Thus, the early ICRF heating helps to maintain the reversed magnetic shear profile which has already been formed. A typical current ramp-up rate in Alcator C-Mod is 5.0 MA/sec up to 0.1 sec. During the reversed magnetic shear experiment discussed here, the current ramp-up rate was initially 5.1 MA/sec and then was reduced to 1.5 MA/sec until the target current I_p=0.8 MA was reached. As shown in Figure 4.7, there were short trips during the very early ICRF heating phase, probably due to poor coupling to the plasma. The power was not more than 1.5 MW during the period of the MHD activity, which was observed not only on magnetics, but also on GPC with the same coherent frequencies ($3 \sim 4$ kHz).

As of 1998, for fluctuation studies in Alcator C-Mod, there were four sets of toroidally displaced magnetic field pickup coils located on outboard limiters. Two sets are composed of 7 coils and the others of 4 coils. In addition, there are some inboard coils which are located closer to the plasma, which are useful for determining poloidal mode numbers. After Fourier-transforming the magnetic signals, we can use the phase differences in either toroidal or poloidal direction in order to determine mode numbers. Usually, the toroidal mode number (n) is determined unambiguously, while the poloidal mode number (m) determination is challenging unless the plasma is circular. In fact, the toroidal mode numbers of all the MHD activities on magnetics within this time period were identified as $n = 1$, as shown in Figure 4.8. As the plasma was nearly circular ($\kappa \sim 1.14$) during the current ramp-up, their poloidal mode numbers (m) could be determined to decrease from 7 to 5 until the big MHD fluctuations were observed on Channel 6 of GPC ($R \sim 0.8$ m) around $t = 0.11$ sec (See Figure 4.9). Figure 4.10 shows the evolution of fluctuations ($\Delta T \equiv (T_{max} - T_{min})/2$)

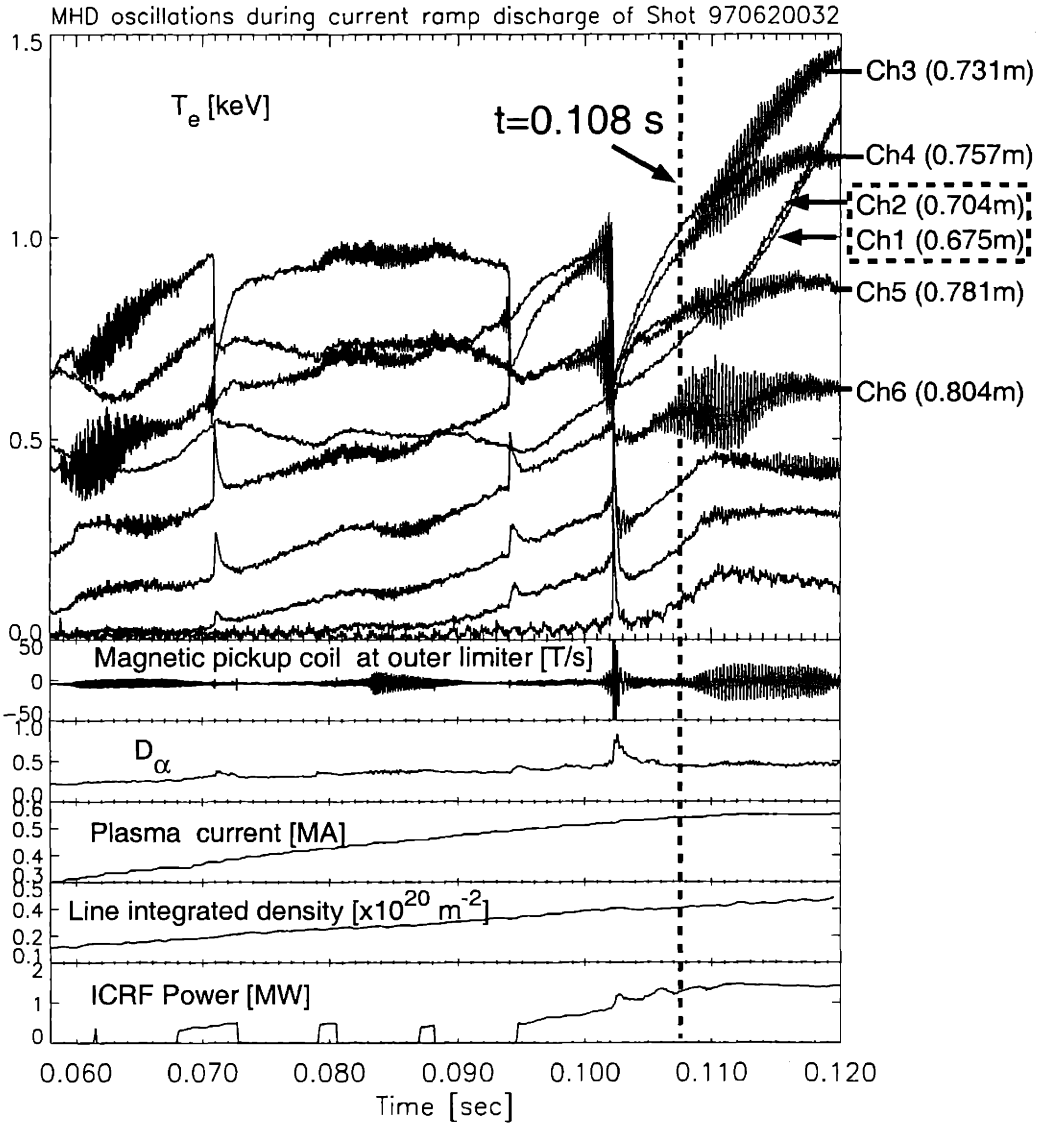

Figure 4.7: MHD activity during reversed magnetic shear plasma. Note that the electron temperatures of the two innermost channels are lower than the third channel (i.e. a hollow temperature profile).

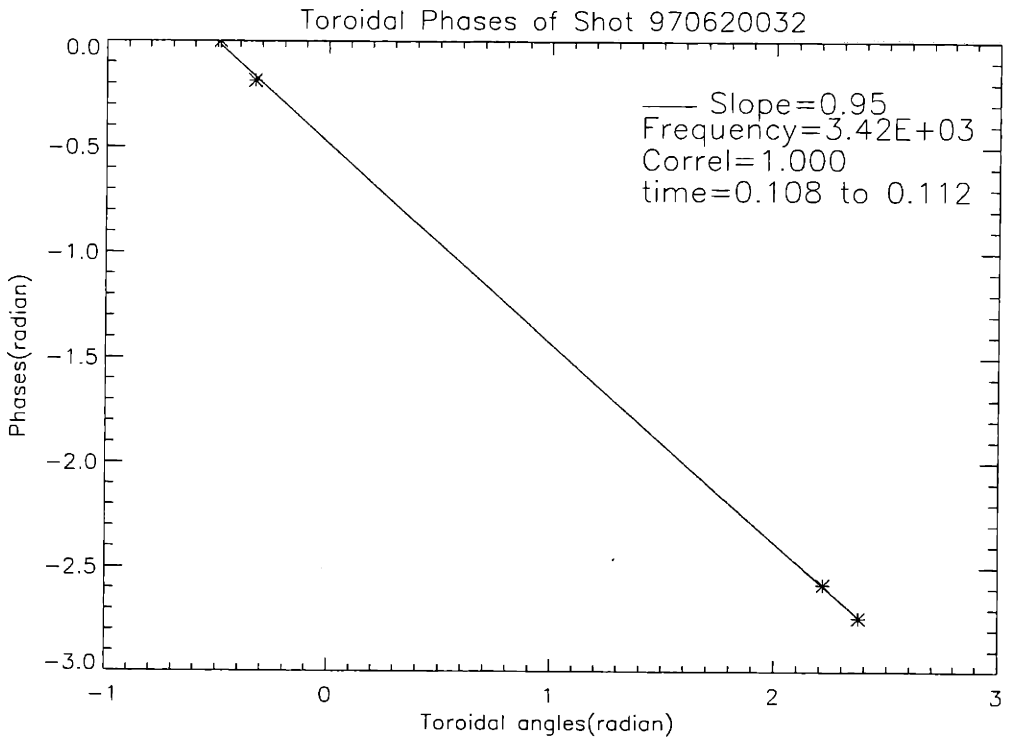

Figure 4.8: Toroidal mode number determination for resistive multiple tearing mode: n=1.

around t=108 msec. In order to use the pressure profile as an EFIT constraint, both ion and electron temperatures and densities are needed. The electron temperatures T_e were given by GPC, while the ion temperature T_i was inferred based on a simple model that the electrons and ions are thermally equilibrated and that the ion confinement time is constant over the profile. The ion density profile $n_i(R)$ was assumed to be the same as $n_e(R)$. The electron densities n_e were inferred from Abel-inverted visible Bremsstrahlung from a multichord diagnostic whose view is horizontal and near the midplane. The brightness[5] of the visible Bremsstrahlung diagnostic is a function of Z_{eff}, n_e, and T_e. When the electron temperatures T_e are provided from GPC and Z_{eff} is assumed to be a constant, n_e can be inferred. As a note, the inverted density profile obtained from far-infrared (FIR) interferometry is regarded as less reliable for this analysis. This is due primarily to the vertical view of the diagnostic, which passes cold, relatively dense plasma in the vacuum chamber above and below the main

[5] $\propto \frac{Z_{eff} n_e^2}{T_e^{0.37}}$

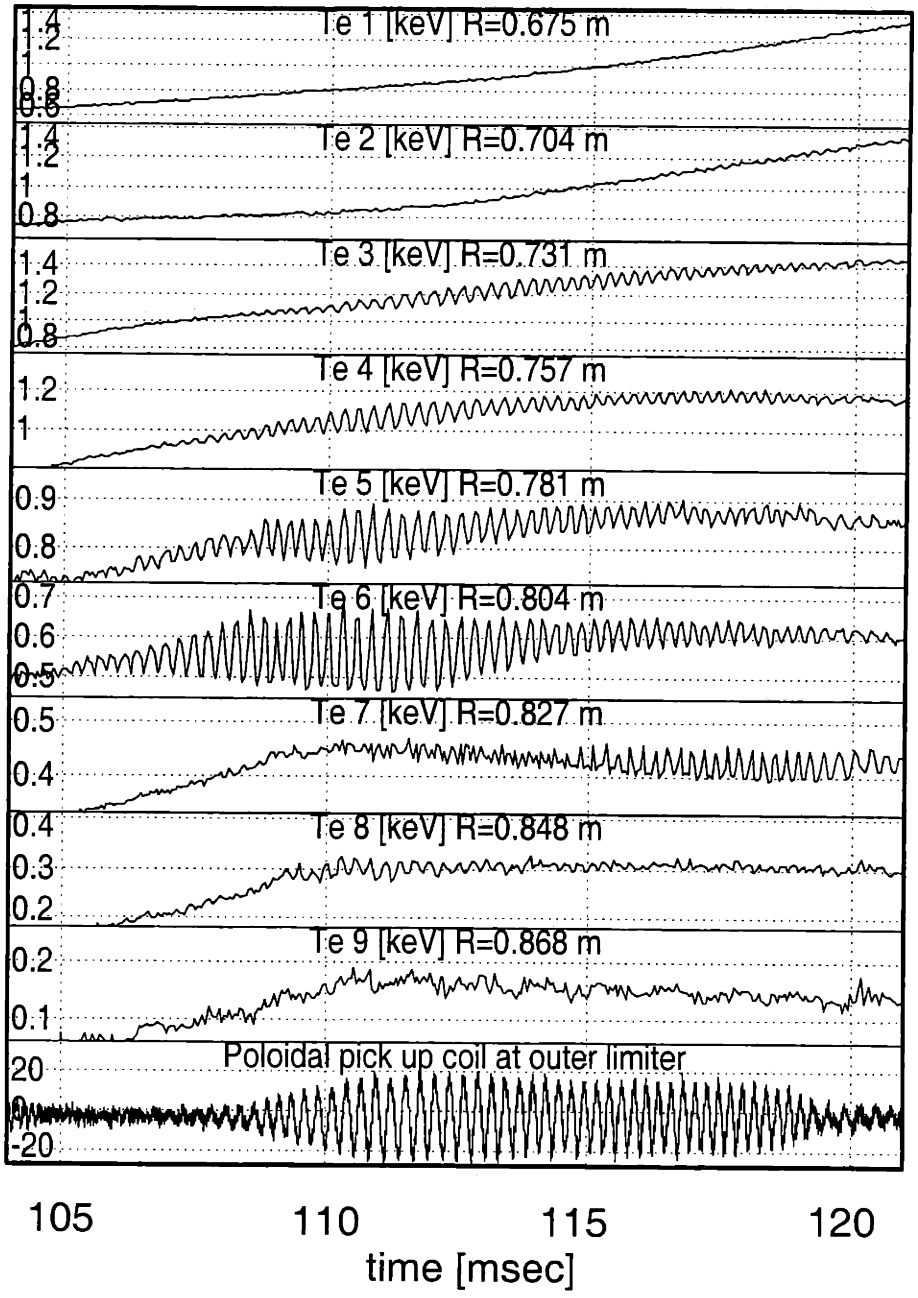

Figure 4.9: Enlarged view of the MHD activity observed on GPC and magnetics of Fig. 4.7 near t=108 msec. In particular, observe that the T_e fluctuations on Channel 6 are the biggest and that the oscillation frequency ($3 \sim 4$ kHz) is the same as that of the magnetics.

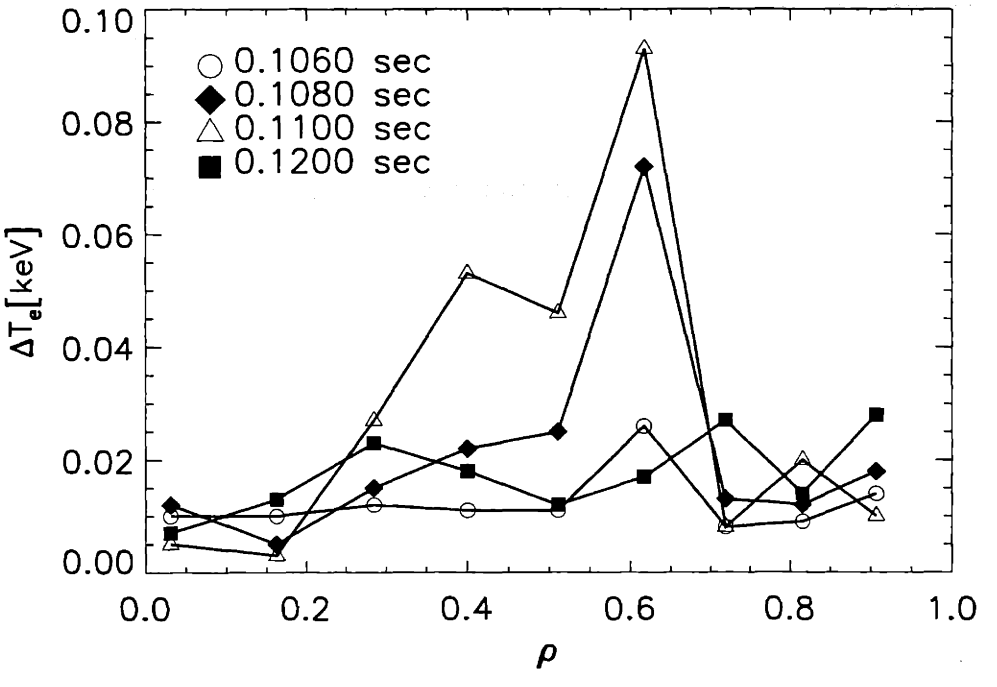

Figure 4.10: At t=0.108 sec considered here, Channel 6, which is located at R=80 $\sim$ 81 cm ($\rho \sim 0.62$), shows the biggest fluctuations. Also, note that the fluctuations of Channel 6 evolve, peak near t=0.11 sec and then the biggest fluctuations move outward into Channel 7 ($\rho \sim 0.72$) at t=0.120 sec.

plasma. Since the contributions of the edge plasmas to the FIR line integrated density measurements are not separated from those of the main plasma, the inversion process is sensitive to rather arbitrarily assumed edge plasma densities. For this reason, the horizontal visible Bremsstrahlung diagnostic was preferred for density measurement. Therefore, the pressure profile is given by $P = n_e T_e + \sum n_i T_i \sim n_e(T_e + T_i) \leq 2 n_e T_e$, where n_e is inferred from visible Bremsstrahlung brightness, while T_e is measured by GPC.

The dashed curve of Figure 4.11 is the pressure profile at t=108 msec calculated in the aforementioned way. Based on this internal pressure profile, as well as magnetics, a most likely reversed magnetic shear configuration has been reconstructed during the current ramp stage. For the stability analysis, the EFIT-reconstructed equilibrium at t=108 msec was used, when the global MHD (G) started to evolve sinusoidally. Figure 4.12 shows the q-profile reconstructed by the kinetic EFIT at t=108 msec.

4.2.2 Stability and interpretation

For stability analysis, the MARS code [57] has been used. This is a linear resistive MHD stability code with a given toroidal mode number and we consider $n = 1$, which has been ascertained in magnetics unambiguously, as shown in Figure 4.8. This stability analysis using MARS code was carried out in collaboration with J.J. Ramos. For the input parameters, the Lundquist number (or magnetic Reynolds number S_0) and the shape of the temperature profile are needed. Unless otherwise specified in the following case, $S_0 \equiv (\tau_R/\tau_A)_0 = 1.67 \times 10^7$ is used. The shape parameter ($\eta_i \equiv d(\ln T_i)/d(\ln n_i)$) has been determined from the relationship between density ($n(\psi)/n_0 = (P(\psi)/P_0)^{1-\alpha}$) and temperature ($T(\psi)/T_0 = (P(\psi)/P_0)^{\alpha}$), so $\eta_i = \alpha/(1-\alpha)$. Since the density profile was weakly decreasing, a best fit for α was found to be $\frac{6}{7}$, giving η_i= 6.0.

The first distinguishable mode has resistive double tearing-like behavior, as shown in Figure 4.13. When the magnetic Reynolds number increases (in other words, η, which is inversely proportional to S_0, decreases), such an instability disappears, which indicates that it is a non-ideal (resistive) mode (i.e. ideally stable). Around the

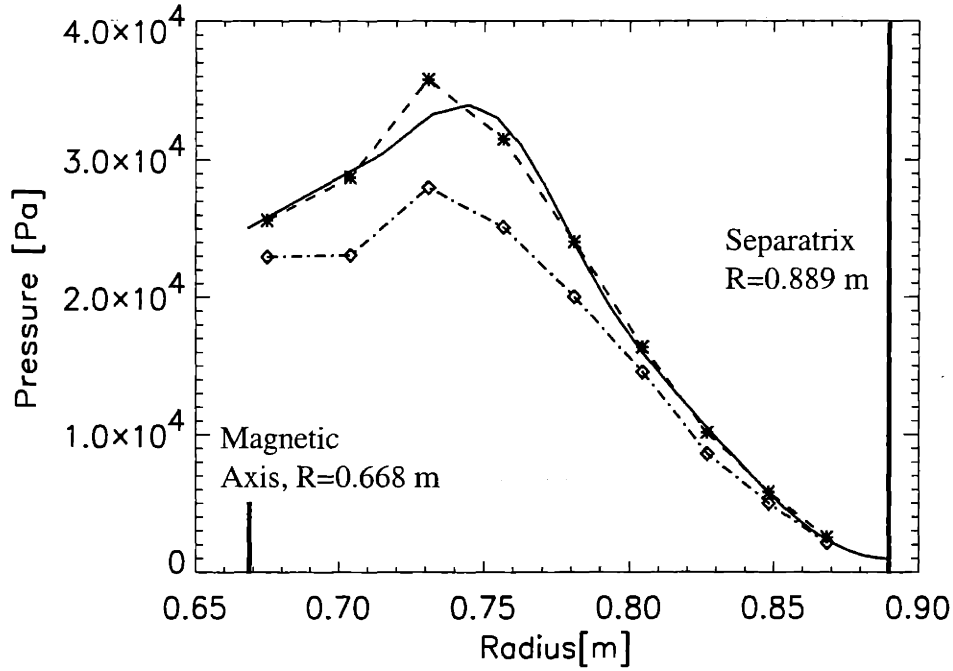

Figure 4.11: Pressure profiles: Solid curve - from EFIT reconstruction; Dashed curve - calculated from T_e of GPC and n_e inferred from visible Bremsstrahlung; Dash-dot curve - 2 $\times(n_e T_e)$, based on T_e of GPC and n_e from TCI-inversion using routinely calculated EFIT reconstruction.

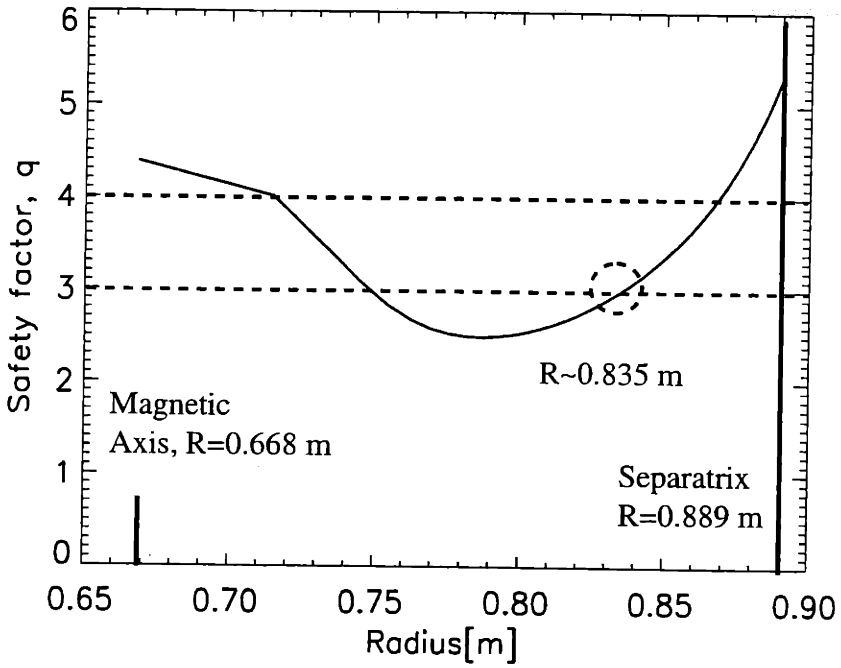

Figure 4.12: q-profile at t=108 msec. Note that the outer q=3 rational surface is located at R$\sim$ 83.5 cm ($\rho \sim 0.73$), which is close to $(\Delta T)_{max}$.

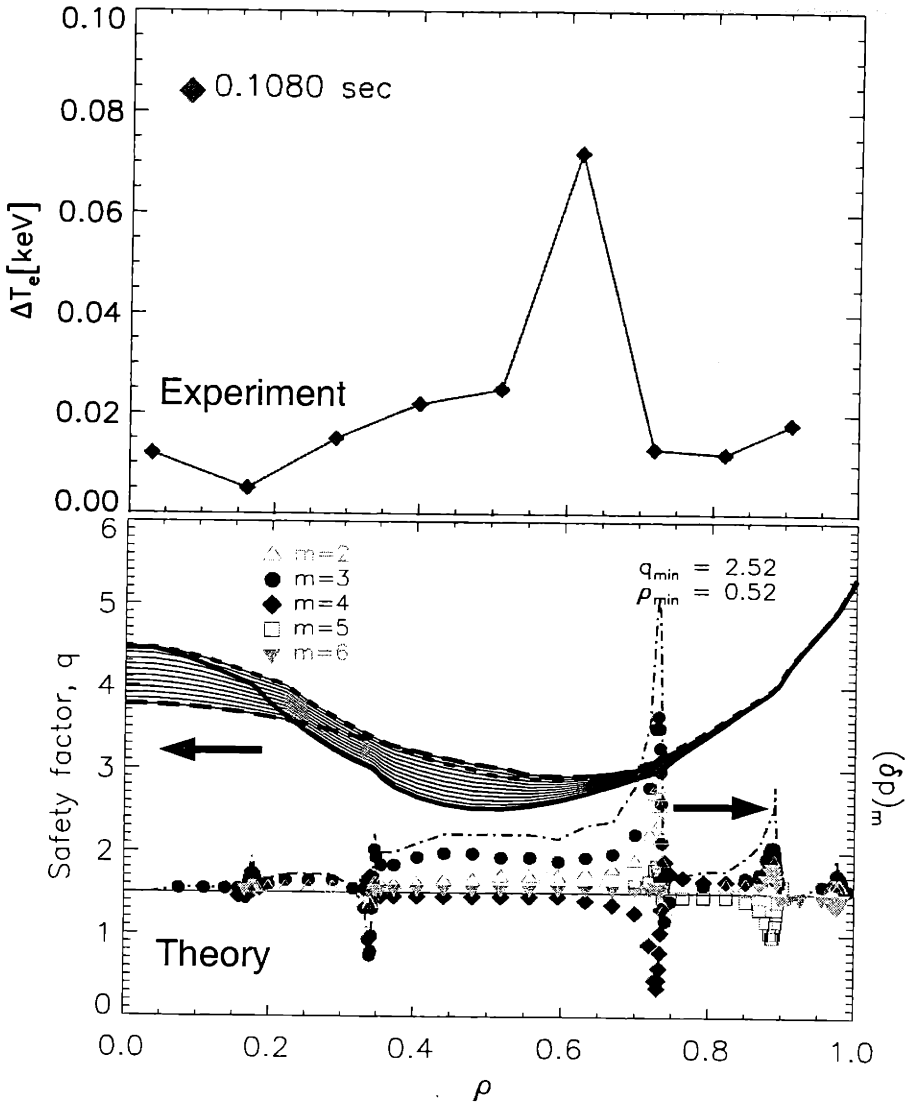

Figure 4.13: n=1 resistive "multiple" tearing mode. Note that resonant layers are observed not only at the outer $q = 3$ surface, but also at the inner $q = 3$ and at the $q = 4$ rational surfaces, which characterizes the "multiple" tearing mode. For the solid thick q-profile curve, $S_0 = 1.67 \times 10^7, \gamma\tau_A \sim 1.8 \times 10^{-4}$, where γ is the growth rate $[sec^{-1}]$ and τ_A is Alfvén time $\sim 8 \times 10^{-8}$ sec. When all the components are summed up, the total predicted pressure fluctuations (δp) are delineated with the dash-dot curve. This can be compared with the temperature fluctuations (ΔT_e) at t=0.108 sec. Theory and experiment results match each other. The other two cases, whose q-profiles are shown in thick short and long dashed curves respectively, also predicted almost the same fluctuations.

$q = 3, 4$ rational surfaces, there were big pressure fluctuations, whose mode components are represented in different symbols (i.e. $\bullet(m = 3), \diamond(m = 4)$). Also, near each resonant surface, every mode component changes its phase. When all of the components are summed up [6], the peaked pressure fluctuation (δp) theoretically predicted in the MARS code is located near the outer $q = 3$ rational surface, whose radial location is 83.5 cm ($\rho \sim$0.73) (See the dash-dot curve and the solid thick curve of Fig. 4.13). Since other resonant layers are seen at various rational surfaces, it can be called a resistive "multiple" tearing mode. In comparison with the experimental observation of Fig. 4.13, the location of the peaked fluctuations predicted in the MARS code is less than 2-3 cm away from Channel 6 (R = 80 - 81 cm ($\rho \sim 0.62$)), whose ΔT_e is the biggest. A range of possible q profiles is shown by the solid thin curves. For a thick short dashed curve of Fig. 4.13, the q-profile has been reconstructed based on two fixed normalized current density points in the core region. On the other hand, a thick long dashed curve shows another q-profile using lower fixed on-axis q-value (q_0) with similar normalized current density profile. All the three cases were reconstructed almost equally likely, apart from the specified constraints, although the q_0 changed from 4.5 to 3.8. From the other two cases, the outer q=3 surfaces ($\rho \sim 0.7$) are even closer to the location of the peaked ΔT_e channel. Figure 4.14 shows the sensitivity of q_0 in the reconstructed equilibrium, in which the most likely occurs at the lowest χ^2. Setting aside the elevated χ^2 cases which appear to indicate a random difference in convergence, Figure 4.14 shows that the EFIT reconstruction is unable to distinguish between central q-values in the range $1 \leq q_0 \leq 4.5$. Therefore the profiles of Figure 4.13 must be considered merely plausible examples, motivated by the independent observation that sawteeth are absent and so $q_0 > 1$. The safety factor at larger minor radius is much less sensitive to uncertainties in the reconstruction. Therefore the position of the outer flux surface is reasonably well known, whereas the position of the inner flux surface cannot be determined from EFIT. The predicted pressure fluctuations were in phase. This also matches well with the experimentally observed

[6] $\delta p = \sum_m (\delta p)_m = \sum_m [\delta p_m(r) \exp\{i(m\theta + n\phi)\}]$.
Assuming ϕ is fixed with θ=0 (ie at the midplane), $\delta p = (Const) \sum_m [\delta p_m(r)]$. If ϕ=0, $Const = 1$. Thus, $\delta p = \sum_m (\delta p_m(r))$, which is used for summing up the components.

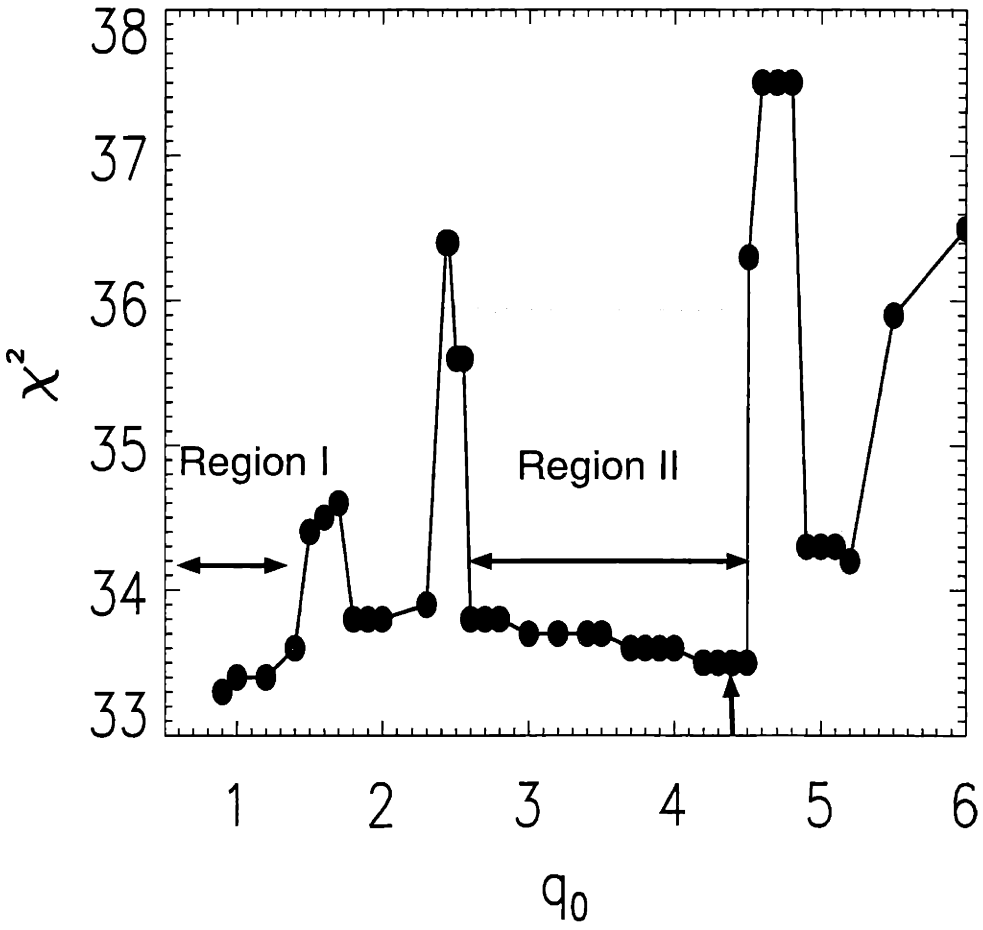

Figure 4.14: Sensitivity of the reconstructed equilibrium in terms of q_0. Near q_0=4.4 is the most likely, whose q-profile corresponds to the thick solid curve of Figure 4.13. Region I invokes typical sawteeth, whose q_0 is ≤ 1, while Region II is more likely to occur during the current ramp-up discharge without sawteeth.

in-phase electron temperature fluctuations. Since this "multiple" tearing mode is a global mode, it is no wonder that most of the GPC channels showed large or small electron temperature fluctuations in the experiment. The perturbed magnetic flux (Δb) [57] linear eigenfunction is shown in Figure 4.15. According to the MARS code results, $\gamma\tau_A \sim 1.8 \times 10^{-4}$, where γ is growth rate [sec^{-1}], τ_A: Alfvén time $\sim 8 \times 10^{-8}$ sec. Thus, the growth time is approximately 0.44 msec, which is within a typical range of tearing mode evolution.

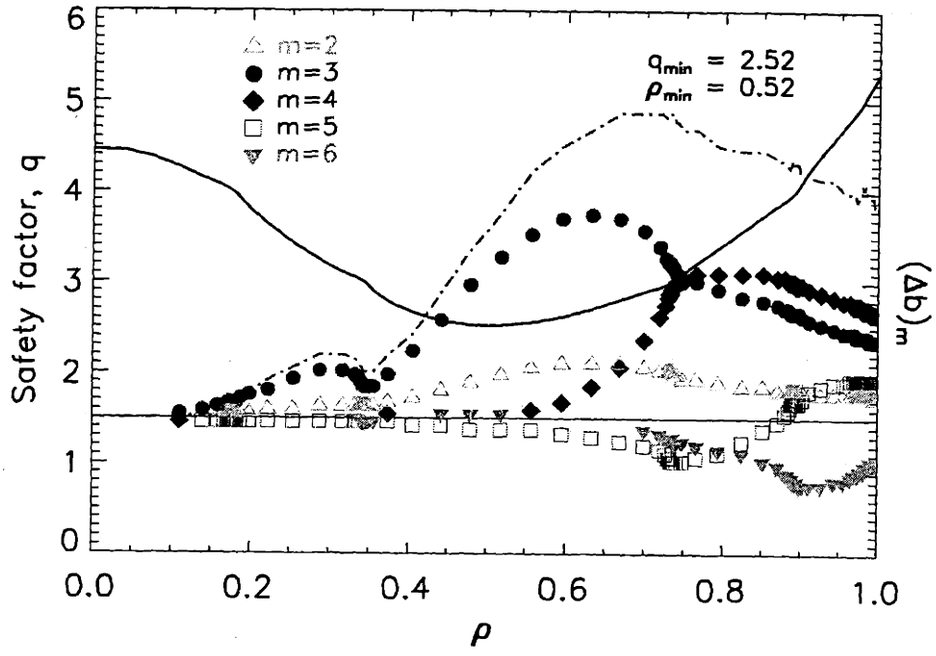

Figure 4.15: Perturbed radial magnetic flux defined as $\Delta b \equiv \frac{d\Phi}{d\theta d\phi} = [\nabla\psi \cdot (\nabla\theta \times \nabla\phi)]^{-1}\tilde{\mathbf{B}} \cdot \nabla\psi$. The sum of the Fourier components giving the perturbed magnetic flux at θ =0 is delineated with the dash-dot curve.

Although this particular MHD event was so benign that it did not evolve into disruption, some resistive double tearing-like MHD events almost terminated the whole plasma. Considering that the main purpose of maintaining reversed shear plasmas is to achieve high performance plasmas, attention should be paid to such MHD events that affect the plasma globally. In fact, similarly disruptive MHD activity is observed on the sawtooth-like crashes of Figure 4.7 (near t = 0.071, 0.094 and 0.102 sec). Re-

calling that the sawtooth-like crashes cannot be predicted in the frame of linear MHD theory, developing a nonlinear MHD theory would be required for this study. In addition, although it is premature to speculate how to suppress such double tearing-like MHD modes, an indicator of whether electron temperature (or pressure) profile is hollow or not can be used to avoid unfavorable situations. This suggestion is based on the observation that hollow electron temperatures tend to be more unstable, as shown in Figure 4.4. The electron temperature ratio of the innermost channel, which is usually located near the magnetic axis, to a middle channel of GPC can be an indicator about the hollowness. For example, T_e (Ch 1)/T_e (Ch 2) or T_e (Ch 1)/T_e (Ch 3) may be a good index experimentalists can check between discharges. To remedy such MHD events during C-Mod current ramp-up discharges, moderately increased current ramp-up rates (eg. the higher current ramp-up rates in Region B of Figure 4.1) seem to be desirable. Experimentally, faster current ramp-up rates lead to reduced numbers of unstable plasmas. This is also consistent with the infrequency of MHD events in Region C of Figure 4.1. On the other hand, this argument does not explain Region A of Figure 4.1, where few MHD fluctuations are observed. One thing which needs to be clarified is that a monotonic electron temperature profile is not a sufficient condition for absolute stability, in the sense that such profiles are sometimes accompanied by rather benign perturbations that are not in the plasma core region. It would, however, be fair to say that the plasmas with hollow electron temperature profile seem to be more unstable.

4.3 Resistive interchange mode

In addition to the multiple tearing mode discussed above, we also obtained a non-global mode in the MARS code, whose fluctuation is highly localized near the inner q=4 rational surface in the NCS region. Experimentally, this would be difficult to observe without suppressing all the other global MHD instabilities, apart from the requirement of spatially well-resolved diagnostics. In fact, there were some indications of highly localized fluctuations on GPC in the 1999 run campaign, which reminded us

of this theoretical prediction. However, the MHD activity in that case was determined to be unstable in terms of the ideal interchange mode, not resistive interchange mode. The detailed analysis will be given in the next chapter.

As shown in Figure 4.16, the resistive interchange mode was predicted to be highly localized at the inner q=4 resonant surface, with its resonant layer as narrow as 0.7 cm. This resistive interchange mode is contrasted with those found in DIII-D

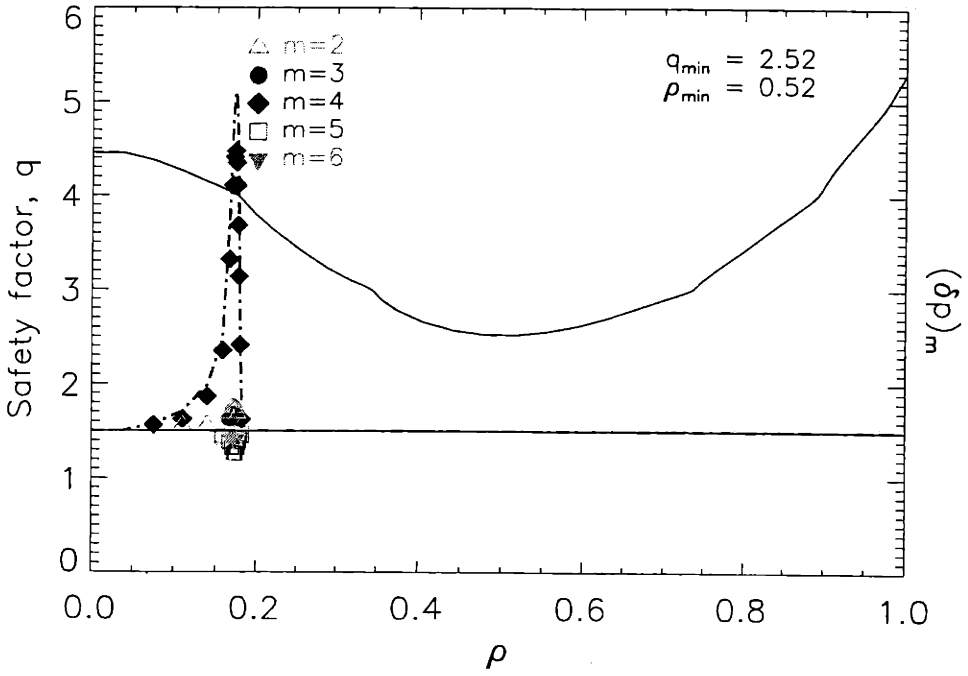

Figure 4.16: n=1 resistive interchange mode. Near the inner q=4 inner rational surface, the fluctuations are highly localized. Each symbol represents a poloidal mode component. The dash dot curve shows the predicted total pressure fluctuations (δp). With $S_0 = 1.67 \times 10^7, \gamma\tau_A \sim 4.9 \times 10^{-4}$, where γ is the growth rate[sec^{-1}], τ_A is Alfvén time $\sim 8 \times 10^{-8}$ sec.

experiments [47]. According to the DIII-D results, the resistive interchange instability can occur beyond a threshold β_N[7]. However, the β_N of the equilibrium discussed here was 0.27[$\%mT/MA$], which is low. Basically, this instability was predicted to occur due to a hollow pressure profile with q $\gg$ 1, not from high β_N. Since the elongation ($\kappa \sim 1.14$) during the current ramp was close to one, we could assume a circular

[7] $\beta_N \equiv \beta/(I_p/aB_0)$ [% m T/MA]; $\beta = 2\mu_0 < p > /B_0^2$, I_p: plasma current [MA], a: minor radius [m], B_0: magnetic field at magnetic axis [T], and $< p >$: volume averaged pressure [Pa]

plasma. The ideal (Mercier) stability criterion ($D_I < 0$)[8] was satisfied. In this case, the H-factor[9] in the NCS region was no more than -0.02. Since $|H| = 0.02 \ll 1/2$ and $(q^2 - 1)$ was positive, the resistive interchange mode stability criterion ($D_R < 0$)[10] was violated by the positive sign of p'.

4.3.1 Characteristics of resistive interchange modes

Theoretically, the growth rate of the resistive interchange mode is proportional to the one-third power of resistivity η [42, 44, 45]. To verify whether this mode evolves in such a way, the relationship between growth rates and resistivity (or S_0^{-1}) has been investigated using all the same configurations except different Lundquist numbers. As shown in Figure 4.17, the growth rate was proportional to $\eta^{1/3}$, which is exactly the same as theory predicts. The predicted growth rate of the resistive interchange mode based on the C-Mod discharge analyzed above is slightly larger than that of resistive 'multiple' tearing mode. However, in the experiment, only the global mode (resistive multiple tearing mode) has been identified, not the localized mode. Considering the predicted resonant layer is no larger than 0.7 cm, which is almost the limit of GPC spatial resolution ($\sim$ 9 mm), such an observation certainly seems to challenge diagnostic capabilities. On the other hand, even if the localized mode had been present, the large perturbations of the other global mode might have prevented us from noticing it. Thus, we think that if the global mode had been suppressed, we might have been able to observe such a localized mode. Such speculation stimulated the author to investigate whether such a localized mode would be observed, when not being interfered with by a global mode. As we will see in the next chapter, it led to identifying the Mercier interchange mode for the first time in experiments, ever since the theory was established in 1960 [58].

---

[8] According to Glasser, Greene and Johnson[45], $D_I = -1/4 + 2ap'/(B_s^2 S^2)(q^2 - 1)$

[9]
$$H = \frac{\mu_0 p' V' f}{2\pi q'} \left[< \frac{1}{|\vec{\nabla}\psi|^2} > - \frac{<B^2/|\vec{\nabla}\psi|^2>}{<B^2>} \right]$$

, where $p' = dp/d\psi, V' = dV/d\psi, q' = dq/d\psi$, $< \cdot >$: flux surface average quantity and $\vec{B} = f\nabla\phi + \nabla\phi \times \nabla\psi$.

[10] $D_R = D_I + (H - 1/2)^2$. In particular, if $|H| \ll 1/2$, $D_R \simeq D_I + 1/4 \simeq 2ap'/(B_s^2 S^2)(q^2 - 1)$

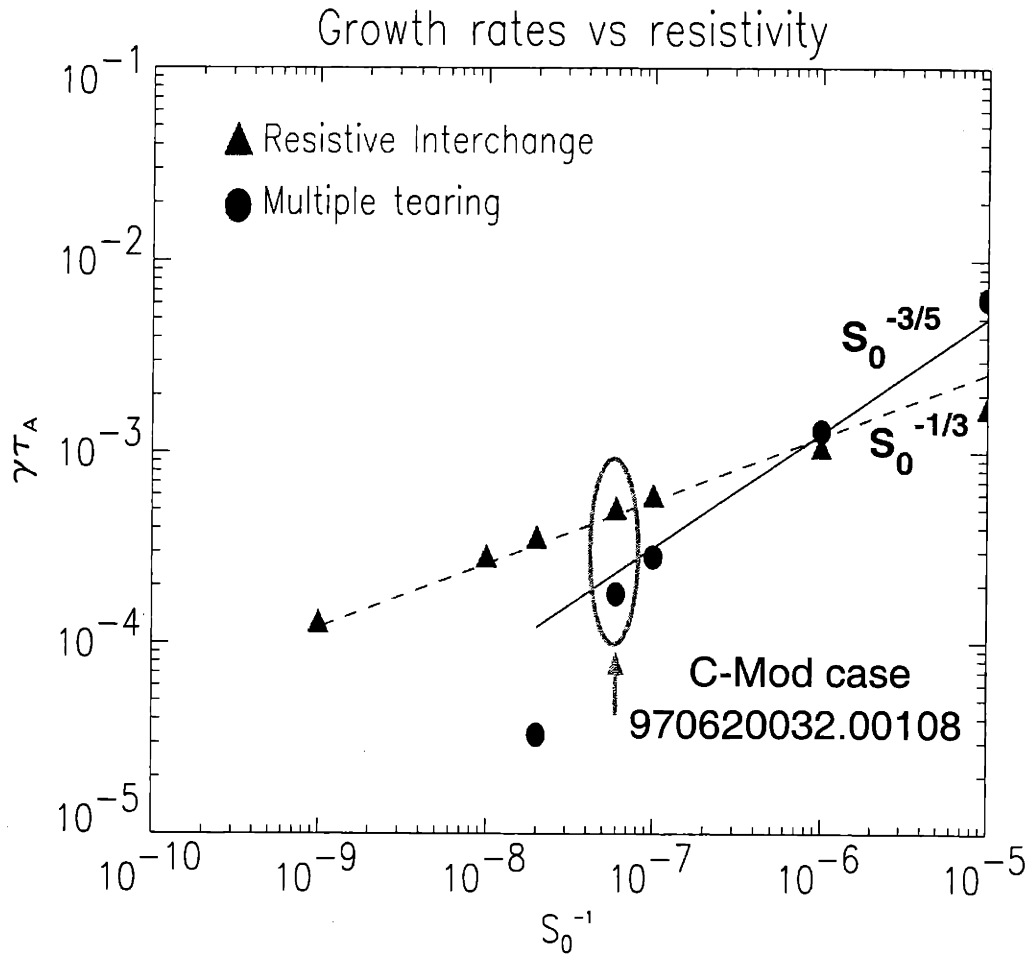

Figure 4.17: Growth rates vs resistivity. The Alcator C-Mod case is encircled. Although the resistive interchange mode was not observed in experiments, it has been predicted to be unstable. The dashed and solid lines are the theoretical growth rates of the resistive interchange and multiple tearing mode respectively. As resistive interchange mode theory predicts, the growth rate is proportional to $\eta^{1/3} \propto S_0^{-1/3}$. The resistive multiple tearing mode evolves in proportion to $\eta^{3/5} \propto S_0^{-3/5}$, which similarly agrees with the theoretical prediction for resistive single tearing modes.

Chapter 5

Identification of Mercier instabilities

5.1 Introduction

During the current ramp-up phase of some discharges in the 1999 C-Mod run campaign, highly localized MHD fluctuations were observed on the ECE diagnostics. These had some similarity to the predicted resistive interchange mode discussed in the previous chapter. The detailed analysis presented here shows that these fluctuations can instead be attributed to a **Mercier instability**. Such an identification may be the first since the Mercier criterion [58] was formulated forty years ago. Until now, no experimental identification of the mode in tokamaks has been reported, though there has been much theoretical speculation regarding Mercier instability in other toroidal devices [59, 60]. Recent theoretical studies of Mercier stability in reversed shear equilibria with monotonic pressure profiles have concluded that such equilibria are stable [61, 62, 63]. However, during the current rise in Alcator C-Mod, reversed shear is often accompanied by hollow pressure profiles, because the current rise time is much faster than the current diffusion time, leading to an off-axis peak in the Joule heating. Under these conditions, the Mercier criterion can be violated and it is of interest to investigate such discharges for signs of a Mercier instability. One reason such instabilities are difficult to observe is that a weak Mercier mode may be stabilized by

the so called finite ion Larmor radius (FLR) effect. The theory of FLR stabilization of ideal MHD modes has been developed over many years [64, 65, 66, 67]. Roberts and Taylor [64] derived the FLR term from the stress tensor and introduced it into generic MHD modes. Ara et al. [65] investigated the FLR effects on internal kink modes. Connor et al. [66] showed that, in high-β plasmas, the calculation of FLR effects on the Mercier instability at high toroidal mode number requires a solution of the ballooning equation. Tang et al. [67] investigated the FLR stabilization of ideal ballooning modes. Nevertheless, FLR theory is incomplete in the sense that, when stabilization is predicted, it finds a pair of purely oscillatory modes ($\omega_{\pm}$ (See Equation 5.8)). These are sensitive to any additional plasma dissipation, which normally leads to destabilization of one of the oscillatory modes and damping of the other. In fact, when resistivity or ion viscosity contributions are included in the dispersion equation, they have opposite effects, with resistivity driving the lower frequency mode, $\omega = \omega_-$, unstable and damping the higher frequency mode, $\omega = \omega_+$. In the case we shall discuss here, ion Landau damping is found to be the dominant dissipative effect and acts like ion viscosity by destabilizing the $\omega = \omega_+$ mode to drive a kinetic Mercier instability [68]. This analysis will be discussed in detail. Localized MHD fluctuations were observed in several discharges. As we will see, detailed analysis revealed that the localized MHD mode was due to a FLR modified, kinetic, Mercier instability. In addition, these reversed shear (RS) discharges displayed other MHD activity, such as off-axis sawtooth-like events in which a fast thermal collapse was observed on some ECE channels and temperature increase on others (i.e outside of an inversion radius) (See also the region of "S" of Figure 4.3).

In Section 5.2, the experimental observations of the localized MHD activity will be described. In section 5.3, the theoretical analysis is presented. Specifically, in section 5.3.1, a reconstructed equilibrium, immediately prior to the MHD activity, will be shown. In section 5.3.2, the results of MHD stability calculations will be shown using both the MARS code and a quasi 1-D model. These predict Mercier instability. In section 5.3.3, FLR stabilization will be discussed to show that the ideal Mercier modes found in section 5.3.2 are FLR stabilized. The dominant dissipative

effect for these modes is identified as ion Landau damping. In section 5.3.4, solutions of a kinetic dispersion relation, which includes ion Landau damping, are presented. These results show that a kinetic Mercier mode is indeed predicted to be unstable in the reversed shear core of C-Mod. In section 5.3.5, the frequencies will be compared with those from experiments. Section 5.4 presents a summary and discussion.

5.2 Observation of localized MHD fluctuations

As shown in Figure 5.1, a localized electron temperature fluctuation was observed on Channel 2 ($R = 0.716$ m) of the GPC in the core. It started to grow at t=115 msec and lasted a few tens of milliseconds, moving inward (i.e. Ch 2 to Ch 1). A similar localized MHD activity has been introduced in the previous chapter (See the region "R" of Figure 4.3). As mentioned, sawtooth-like crashes followed later (the first normal sawtooth crash ($q_0 \sim 1$) of this shot occurred at 340 msec). Fig. 5.2 shows a plot of the innermost four channels of GPC data, time expanded about t = 115 msec. Two things which should be emphasized are that the electron temperature (T_e) was hollow and that the fluctuation frequency was $\sim$ 3 kHz. As mentioned in Chapter 2, an additional 19 channel grating polychromator from PPPL (named 'GPC2') has been operational since 1998. Similar temperature fluctuations were observed on the GPC2 fast channels, but the raw signals were noisy. It is thus clearer to compare the Fourier-transformed amplitudes. The Fourier-transformed amplitudes at $\sim$ 3 kHz of the two combined GPCs (GPC and GPC2), plotted in Figure 5.3, clearly show that the fluctuations were localized within 2 cm ($\Delta\rho \sim 0.1$). Each point in Figure 5.3 is chosen from the combined 28 channels of GPCs. Other diagnostics (eg. density measurement) have been examined at the same locations; before, during and after the fluctuations (the time bins are illustrated as shaded regions of Figure 5.2).

A coherent frequency at 3.2 kHz was also observed on magnetic measurements. Figure 5.4 shows the Fourier-transformed amplitudes of the magnetic signals, which clearly have a 3.2 kHz coherent frequency peaked during the localized MHD event in the same time period. From the magnetics, the toroidal mode number was iden-

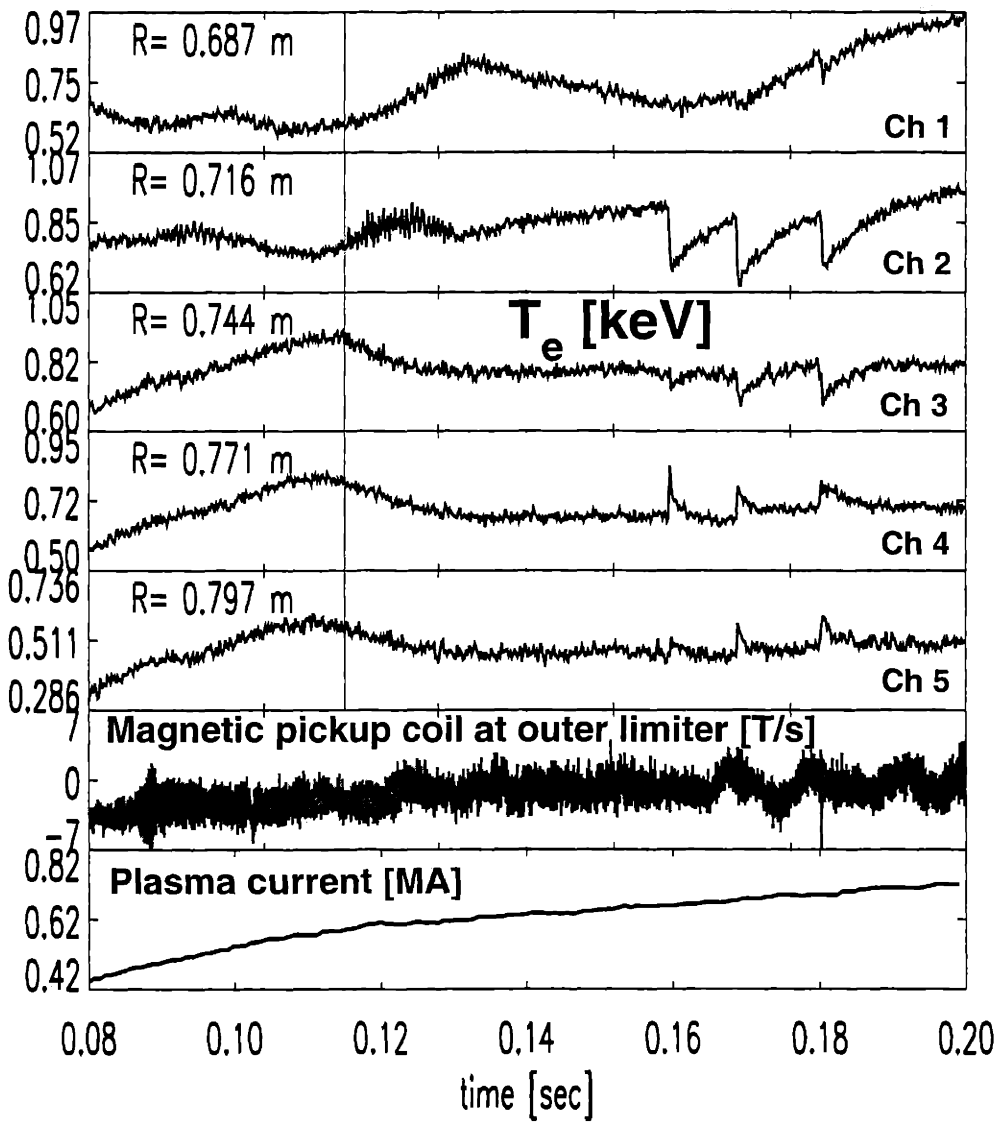

Figure 5.1: MHD activity during current ramp discharge. Near t=115 msec, highly localized MHD fluctuations are observed on the second channel and then sawtooth-like crashes follow later.

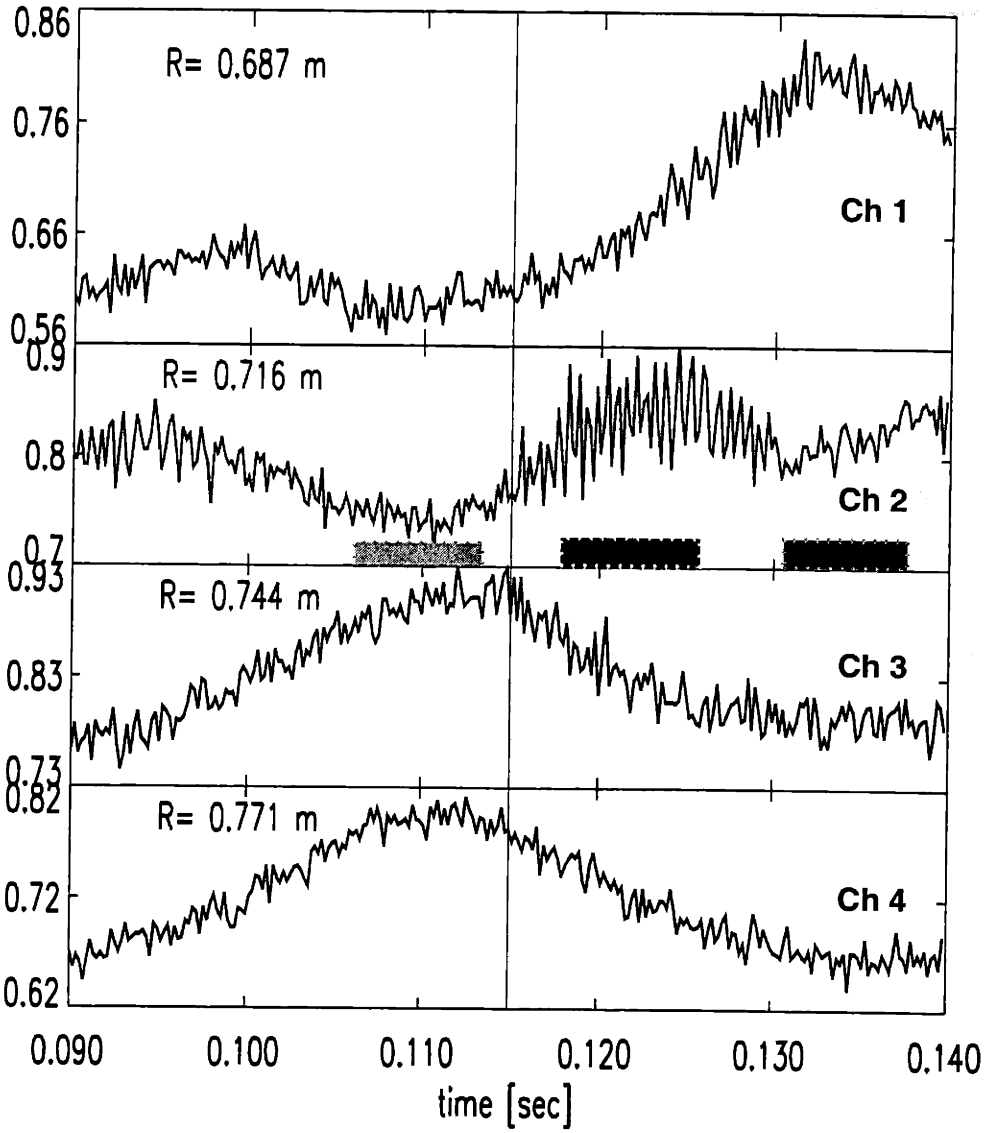

Figure 5.2: Highly localized MHD on the innermost four GPC channels. Note that the MHD is extraordinarily localized on the second channel and that the temperature profile was hollow; near t=115 msec, T_e(Ch 1)=0.61 < T_e(Ch 2)= 0.77 < T_e(Ch 3)=0.88 > T_e(Ch 4)=0.78 in keV units. See also the electron temperature profile in Figure 5.6. Each shaded area represents the time bin for comparison with magnetics; 'before', 'during' and 'after' this fluctuation.

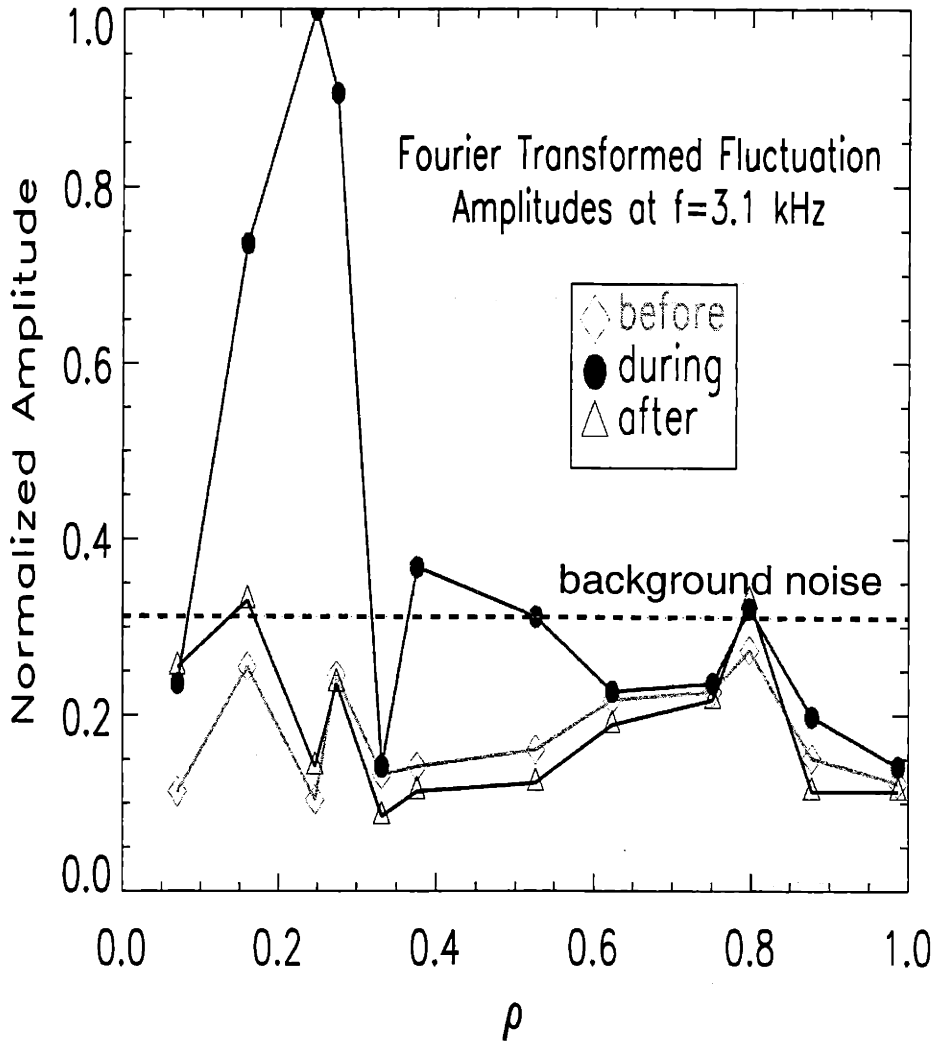

Figure 5.3: Fourier-transformed fluctuation amplitudes at $\sim$ 3 kHz of the combined dataset of GPC and GPC2. The amplitudes are normalized with respect to the maximum Fourier-transformed GPC fluctuation amplitude. The amplitudes during the localized MHD are significantly above those before and after the event. Later, comparison with the MARS results will show that the fluctuations were due to an ideal interchange mode.

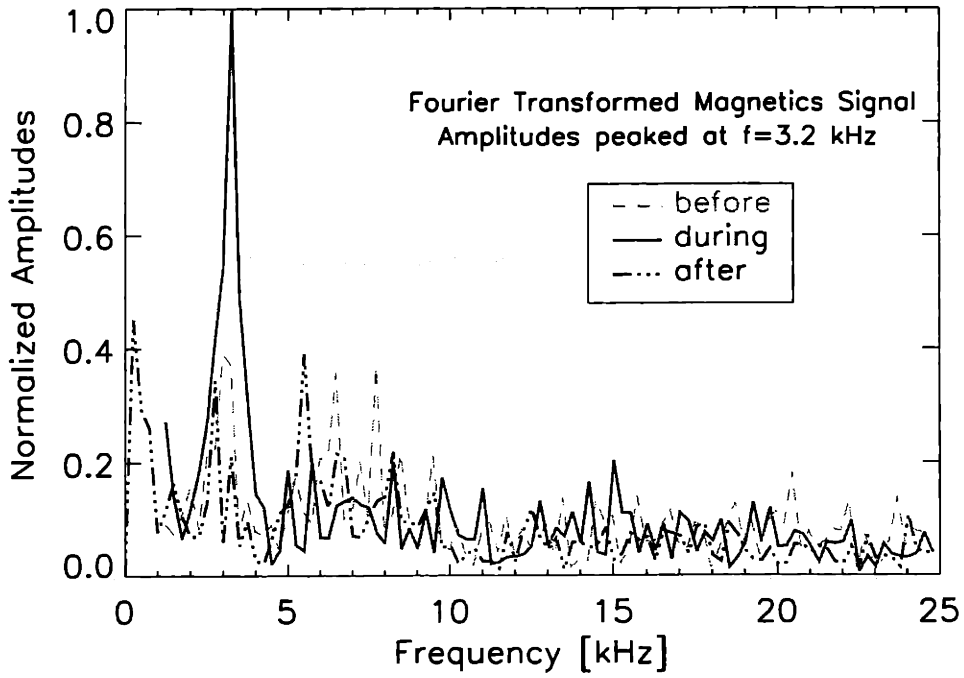

Figure 5.4: Fourier-transformed magnetic signals before, during and after the localized MHD. The coherent frequency near 3.2 kHz is dominant during the event. These time bins are as defined in Figure 5.2.

tified as $n = 1$ (See Figure 5.5). The MHD activity is found to rotate in the counter-I_p direction, which is equivalent to the ion diamagnetic drift direction, since we conjecture that the magnetic fluctuations originate from the same region where the electron temperature fluctuations are observed. As a note, the usual counter-I_p direction is equivalent to the electron diamagnetic drift direction in standard ($\mathbf{B} \times \nabla \mathbf{B}$ towards X-point) magnetic field operation because the pressure gradient is monotonic and negative with respect to the radial coordinate ($dp/dr < 0$). However, for an inverted pressure profile ($dp/dr > 0$), the counter-I_p direction becomes equivalent to the ion diamagnetic drift direction. As mentioned in chapter 4, the determination of the poloidal mode number (m) is uncertain, but when it is assumed that the core plasma flux surfaces are nearly circular ($\kappa \sim 1.26$), either $m = 5$ or $m = 6$ is found to be likely. The electron density was determined from the upgraded visible Bremsstrahlung, which has been successfully cross-checked with other density measurements, such as Thomson scattering and reflectometry. The density profile was found to be weakly decreasing with R in the core, as shown in Figure 5.6. It should be mentioned that there were spurious edge signals on the visible Bremsstrahlung diagnostic. Considering that reflections from the vessel might have caused the unexpected signals, the density data in the edge region in doubt have been neglected. The edge density profile was fortunately not critical in the following analysis related to the core region. Assuming that the equilibration time between electrons and ions was short but that the electron temperatures are slightly higher than the ion temperatures because the ohmic heating is primarily given to electrons, $T_i(0)/T_e(0)$ was estimated to be 0.9. In addition, assuming that the ion confinement time was constant over the plasma cross section, the ion temperature and pressure profiles were also estimated with $n_i \sim n_e$. Thus, the total pressure profile, as well as the electron pressure profile, was found to be hollow, as shown in Figure 5.6.

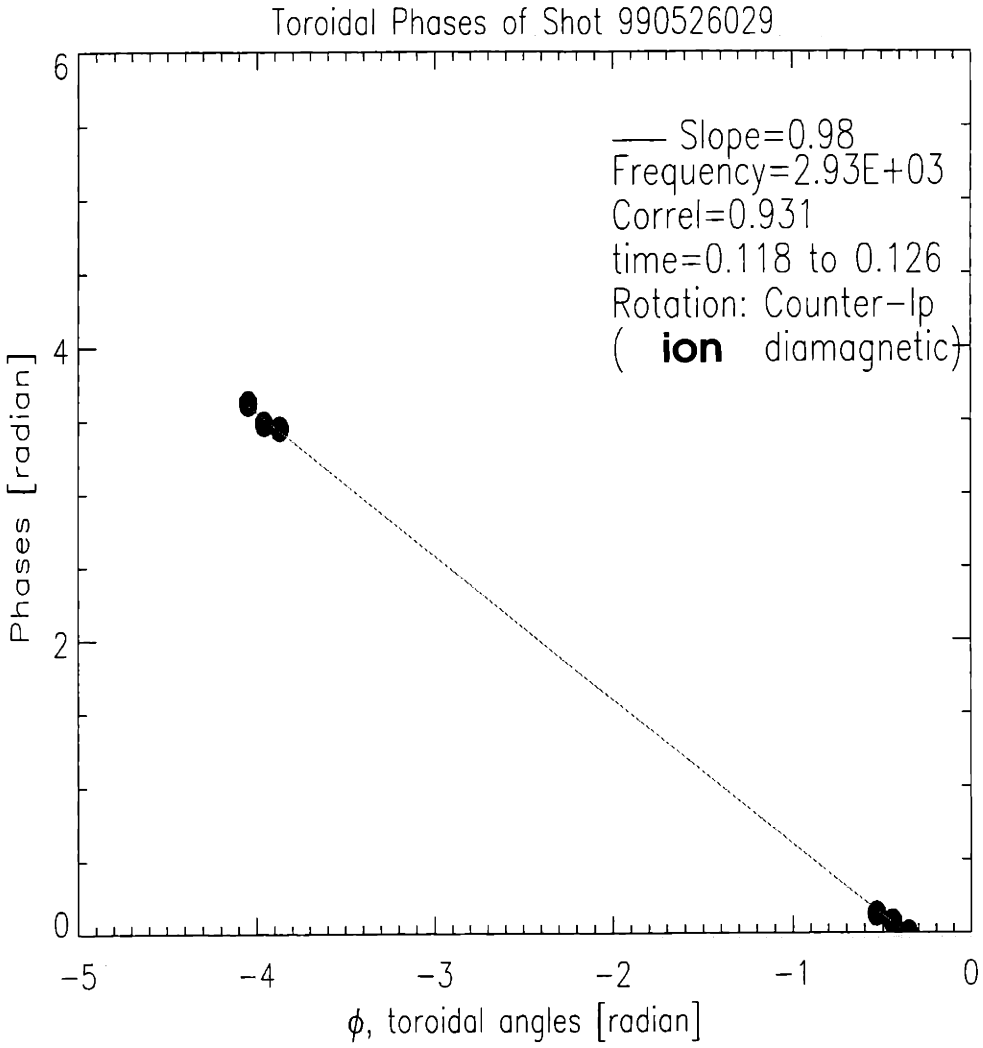

Figure 5.5: Toroidal mode number determination. In the 1999 run campaign, the magnetics were upgraded. From the new fast magnetics, the toroidal mode number was clearly identified as $n = 1$. In the lab frame, it was found to be rotating in the ion diamagnetic direction.

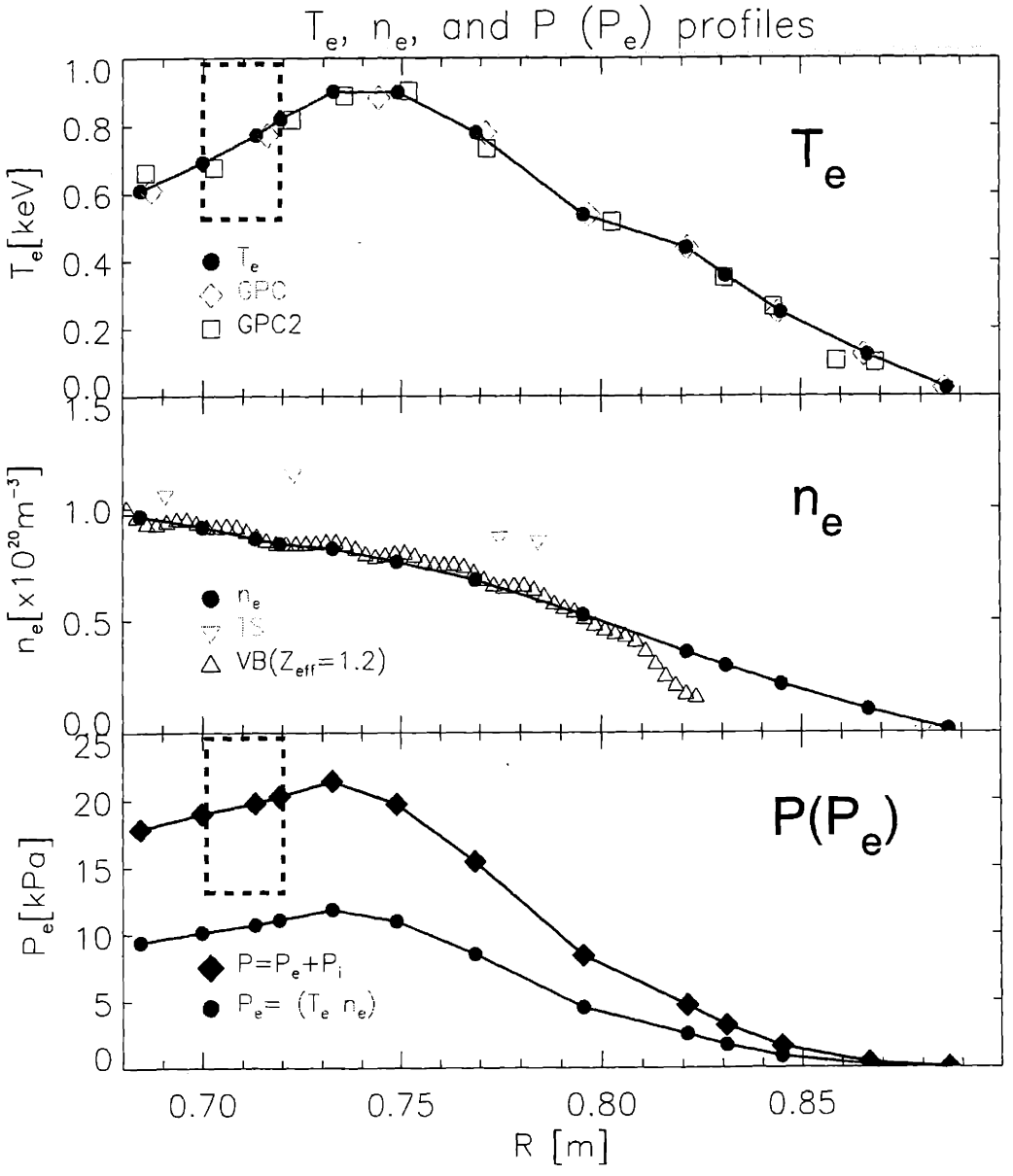

Figure 5.6: Electron temperature (T_e), density (n_e), pressure (p_e) and total pressure ($p = p_i + p_e$) profiles. Note that electron temperature is hollow, while the density is weakly decreasing. In addition, the total pressure is also hollow. Each circle represents one of the combined locations of GPC and GPC2. The dashed rectangle represents the location of the localized MHD activity from the combined data set.

5.3 Theoretical interpretation

5.3.1 Equilibrium

Using the pressure profile and two fixed normalized current density points in the core region as additional constraints to the EFIT program, an equilibrium with reversed magnetic shear was constructed. This showed $q(0) > 5$. Figure 5.7 shows the EFIT-reconstructed pressure profile with the input pressure constraints indicated. The associated q-profile is also shown. Comparison with Figure 5.3 shows that the localized fluctuations were observed near the inner $q = 5$ rational surface ($r/a \sim 0.25$). Thus, the poloidal and toroidal mode numbers $m/n = 5/1$ are found to be more likely than $m/n = 6/1$. Figure 5.8 shows the sensitivity of the reconstructed equilibrium vs q_0, in which the error-free zone is narrow near $q_0 = 5.5$. The q-profile of Figure 5.7 was found based on this reconstructed equilibrium. In the lower q_0 zone, the reconstructed equilibria with an error showed the 'triple hump' current density profile radially, which appears physically unlikely. On the other hand, at the reconstruction in the 'error-free' zone near q_0=5.5, smooth hollow current density profile has been reconstructed.

5.3.2 MHD stability theory

2-D toroidal ideal and resistive MHD simulations

Instability studies using the MARS code (with toroidal mode number $n = 1$) show two modes predicted to be unstable. Figure 5.9 shows the scaling of their growth rates, γ, with Lundquist number, S, in the code. One mode is the resistive "multiple" tearing mode discussed in chapter 4, for which $\gamma \sim S^{-3/5}$ [23]. The other mode, which for this plasma has the higher growth rate at the experimental value of S, is identified as an ideal-unstable mode by the observation that the growth rate ($\gamma_I \sim 1.0 \times 10^{-3} \omega_A$, where γ_I is the ideal growth rate and $\omega_A = B_0/R(\mu_0 \rho)^{1/2}$) becomes constant at high S. Figure 5.10 shows the radial structure of the pressure fluctuations (δp) associated with the ideal interchange mode and its poloidal harmonic content, whose peak is

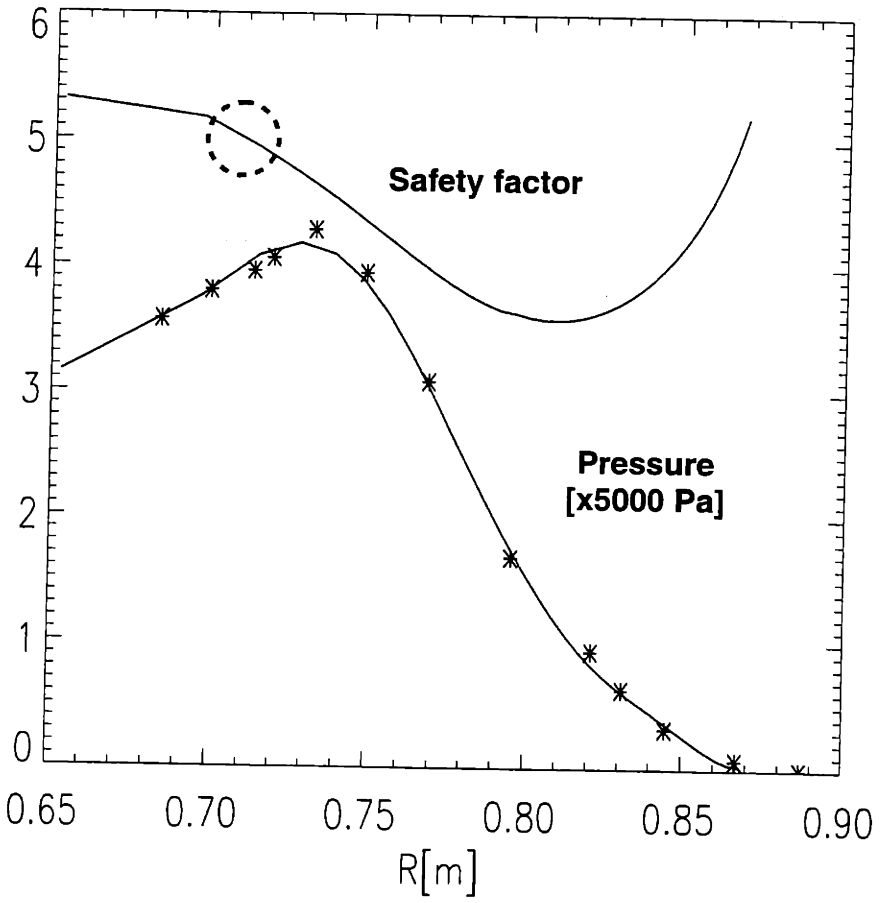

Figure 5.7: Safety factor and pressure profiles. The asterisks ($*$) represent pressures as input to EFIT reconstruction, while the solid curve is the EFIT output. Note the inner $q = 5$ surface is located in the inverted pressure gradient region ($dp/dr > 0$).

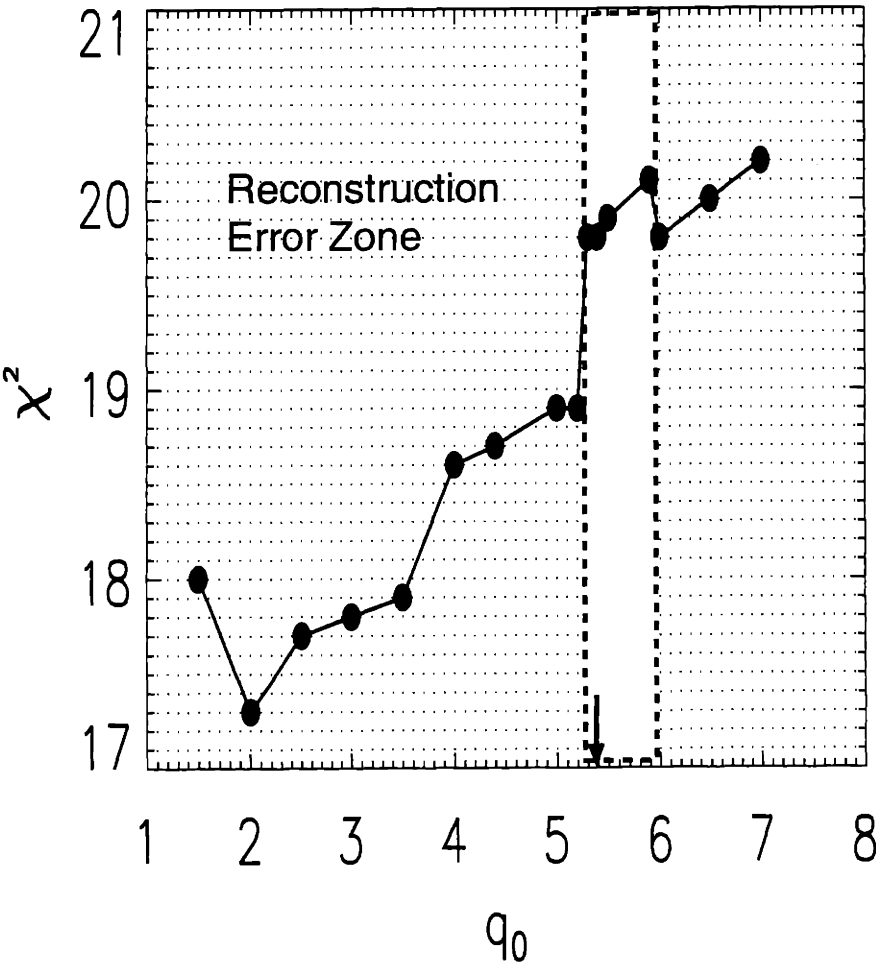

Figure 5.8: Sensitivity of the reconstructed equilibrium in terms of q_0. Near q_0=5.5 was the only error-free zone. The lower q_0 zone showed an error related to $\beta_p + l_i$, while the higher q_0 zone had an error related to β_p. Here, β_p is the poloidal β and l_i is the internal inductance of the plasma. In the lower q_0 zone with the error, a 'triple hump' current density profile has been reconstructed, which is very unlikely.

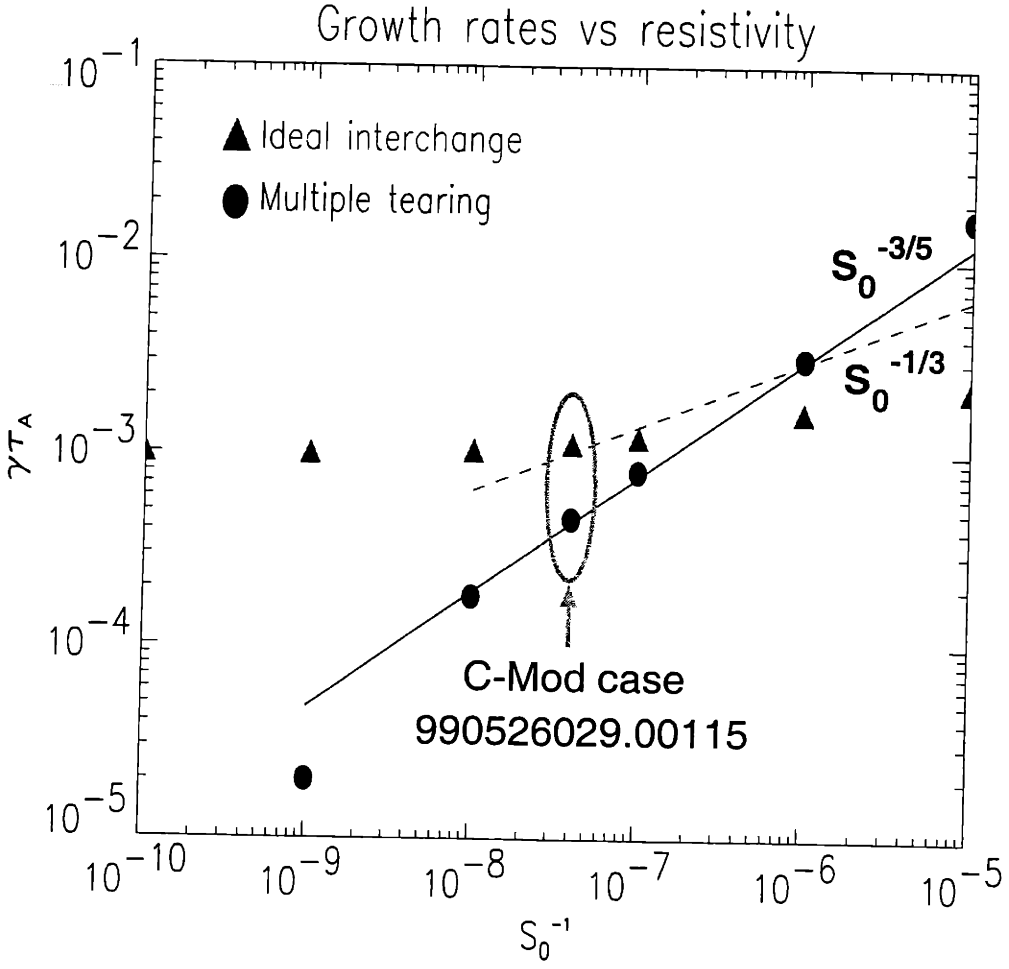

Figure 5.9: Growth rates vs resistivity using the MARS code. The Alcator C-Mod case is circled. As the resistivity decreases, the growth rates become independent of it, which is characteristic of an ideal MHD mode. The dashed and solid lines are the theoretical growth rates of the resistive interchange and multiple tearing mode respectively. Thus, the ideal interchange mode was predicted to have higher growth rate than the multiple tearing mode.

also located at the inner $q = 5$ rational surface ($r/a \sim 0.22$). The MARS mode radial structure agrees well with the experimental T_e perturbation in Figure 5.3.

Evaluation of the exact Mercier [58] stability criterion,

$$D_M - 1/4 < 0, \tag{5.1}$$

which is performed by the MARS code on each flux surface, reveals that this criterion is violated across a substantial region of the plasma core where the pressure gradient is reversed ($dp/dr > 0$). Near the magnetic axis, if the magnetic surfaces are approximately circular, D_M takes the form:

$$D_M = \frac{-2\mu_0 r p'(1-q^2)}{B^2 s^2} \tag{5.2}$$

with the shear $s \equiv rq'/q$ and primes representing radial derivatives. The key factors contributing to violation of the Mercier criterion in the core of C-Mod are the large values of q there ($q^2 > 20$), the moderate shear, and the reverse pressure gradient. This interchange mode, including the resistive interchange mode in Section 4.3, can be physically explained as follows: Suppose that a hollow pressure profile is observed in the core region as shown in Figure 5.11. On the outer flux surface in this figure, for $q > 1$, the portion of good curvature region at the flux surface is larger than that of bad curvature region. If the average is taken over the flux surface, the good magnetic curvature will be prevalent, which indicates that it will be stable. On the other hand, on the inner flux surface shown, the conventionally good and bad curvature regions in the core are reversed because the p''s in inboard and outboard regions of the core are parallel($\swarrow\swarrow$) and antiparallel($\nearrow\swarrow$) to the magnetic curvature $\vec{\kappa}$ which always points inward. Thus, as long as the hollow pressure profile is maintained with $q_{min} > 1$, the rational surfaces in the core region are prone to an interchange instability due to the positive pressure gradient (p'). Nevertheless, the question about which mode is unstable needs detailed calculations.

In the case discussed here, it is natural to identify the observed fluctuations with an $n = 1$ and dominantly $m = 5$ Mercier instability. The poloidal harmonic content

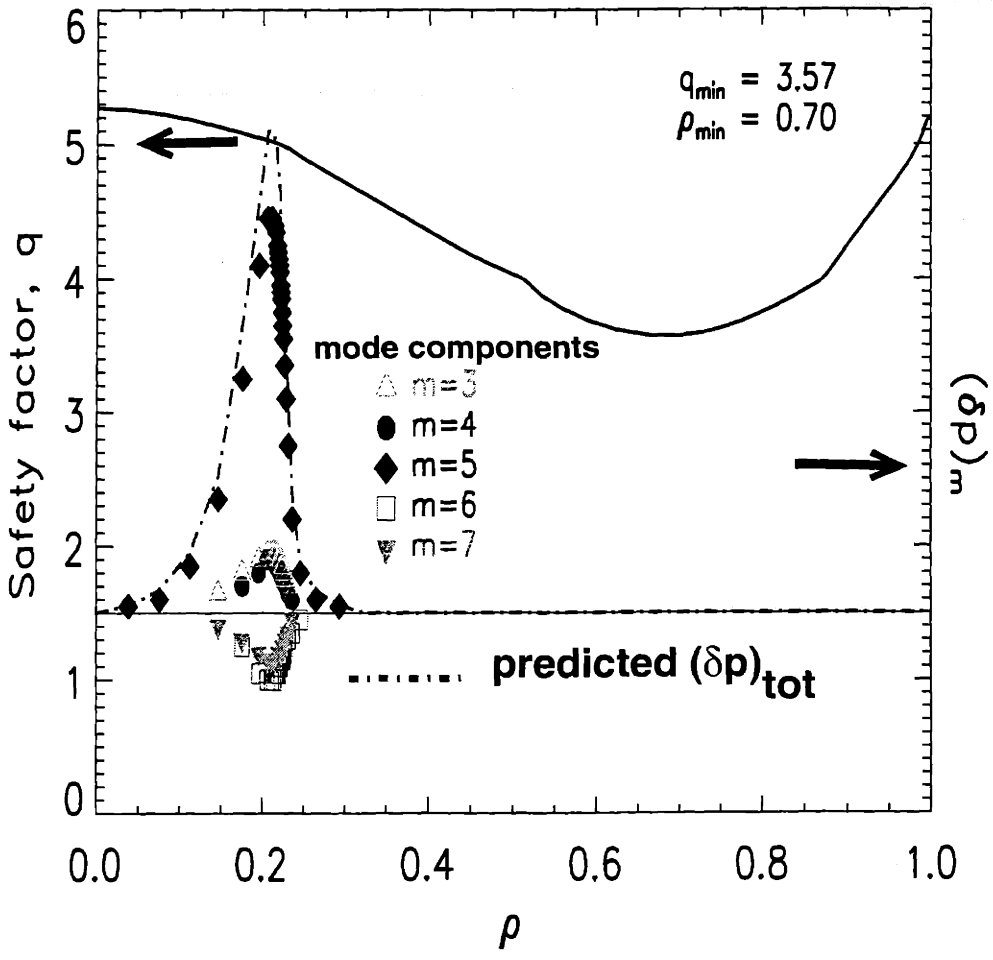

Figure 5.10: $n = 1$ ideal interchange mode. Near the inner $q = 5$ rational surface, the fluctuations are highly localized. Each symbol represents a poloidal mode component. The dash-dot curve delineates the predicted total pressure fluctuations (δp). With $S_0 = 1.25 \times 10^7, \gamma_{cmod}\tau_A \sim 1.2 \times 10^{-3}$, where γ is the growth rate$[sec^{-1}]$ and τ_A is the Alfvén time $\sim 8 \times 10^{-8}$ sec.

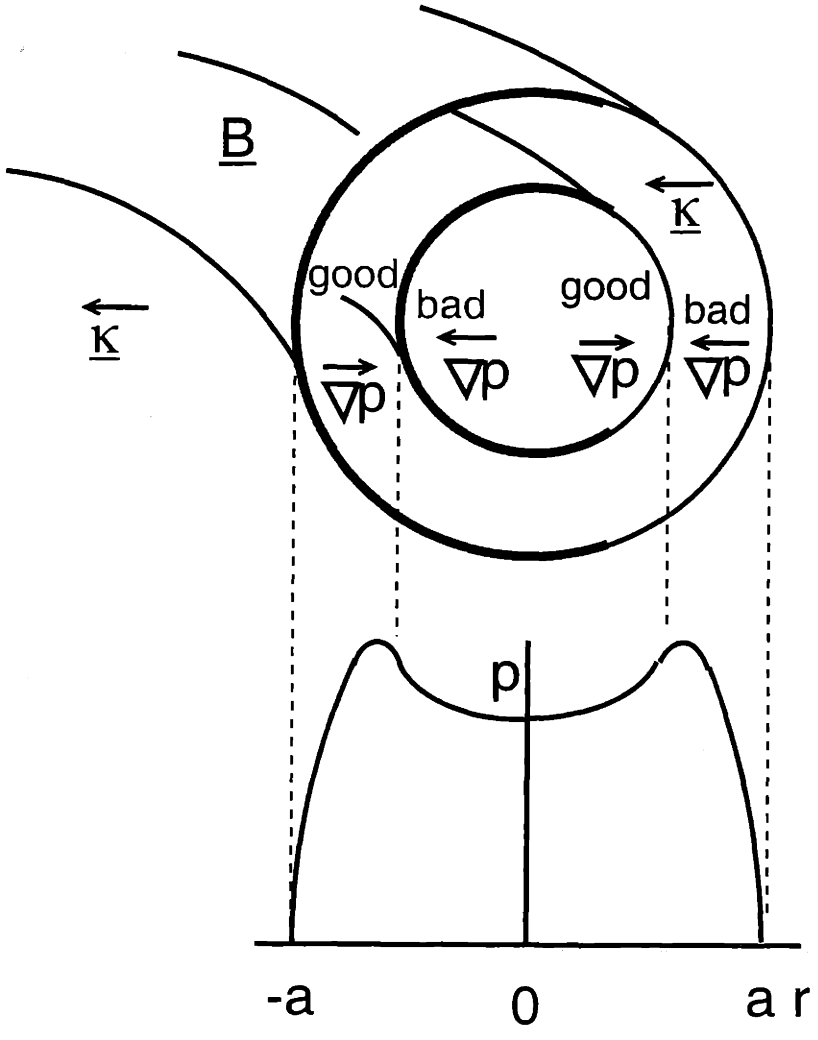

Figure 5.11: When a hollow pressure profile exists in the core, the good and bad curvatures are reversed relative to the normal (monotonically decreasing) pressure profile. The thick curves represent conventionally good curvature regions on the flux averaged surfaces for $(q^2 - 1) > 0$.

(in Figure 5.10) provides further support, since a feature of the Mercier instability is a weak 'ballooning' content in which all harmonics are centered on the same rational surface, in this case $q = 5$. This feature distinguishes a Mercier instability from true ballooning instabilities in which each poloidal harmonic, m, is centered on its own rational surface at $m = nq$, leading to a more radially extended eigenmode structure. However, the identification of highly localized temperature fluctuations in the C-Mod core with an instability of Mercier type raises the question of whether, since the Mercier stability criterion is violated over an extended region, other Mercier modes were also present and if not, why not. This question will be revisited later.

Quasi 1-D ideal MHD analysis

A surprisingly accurate replication of the fully 2-D MARS results was obtained by R.J. Hastie by solving a $1-D$ eigenmode equation for $\xi_r^{(m=5)}$, of the form [69]:

$$\frac{d}{dr}\left\{r^3 A \frac{d\xi}{dr}\right\} - r\xi(m^2-1)A + r\xi D_M s^2 = 0 \qquad (5.3)$$

with

$$A = (\frac{m-nq}{q})^2 + \frac{\gamma^2}{\omega_A^2}(1+q^2 f_+ + q^2 f_-) \qquad (5.4)$$

$$f_\pm = \frac{\omega_s^2}{\gamma^2 + \omega_s^2(m \pm 1 - nq)^2} \qquad (5.5)$$

$$\omega_s = C_s/Rq, \qquad C_s^2 = \frac{5}{3}\frac{p}{\rho} \qquad (5.6)$$

This, apparently cylindrical, equation contains two important toroidal effects:
(i) In $D_M s^2 \simeq -2r\mu_0 p'(1-q^2)/B^2$, the q^2 term represents both the effect of average toroidal curvature and the effect of 'weak ballooning' (the presence of the small sideband harmonics visible in the MARS eigenfunction in Figure 5.10).
(ii) The inertial enhancement factor, $(1+q^2(f_+ + f_-))$, represents inertial contributions from large sideband ($m = 4$ and $m = 6$) longitudinal displacements ($\xi_\parallel$), and also the effects of adiabatic compression at finite growth rate γ. For subsonic growth rates it reduces to the familiar form $(1+2q^2)$. Solution of Equation 5.3, with $q(r)$ and

$p(r)$ profiles similar to those used in the MARS simulations and the value of D_M taken from MARS, yields $\gamma \sim 0.95 \times 10^{-3}\omega_A$, within 5% of the value ($\gamma_I \sim 1.0 \times 10^{-3}\omega_A$) obtained from the MARS code. The corresponding eigenfunction is shown in Figure 5.12. These Mercier growth rates are in fact subsonic.

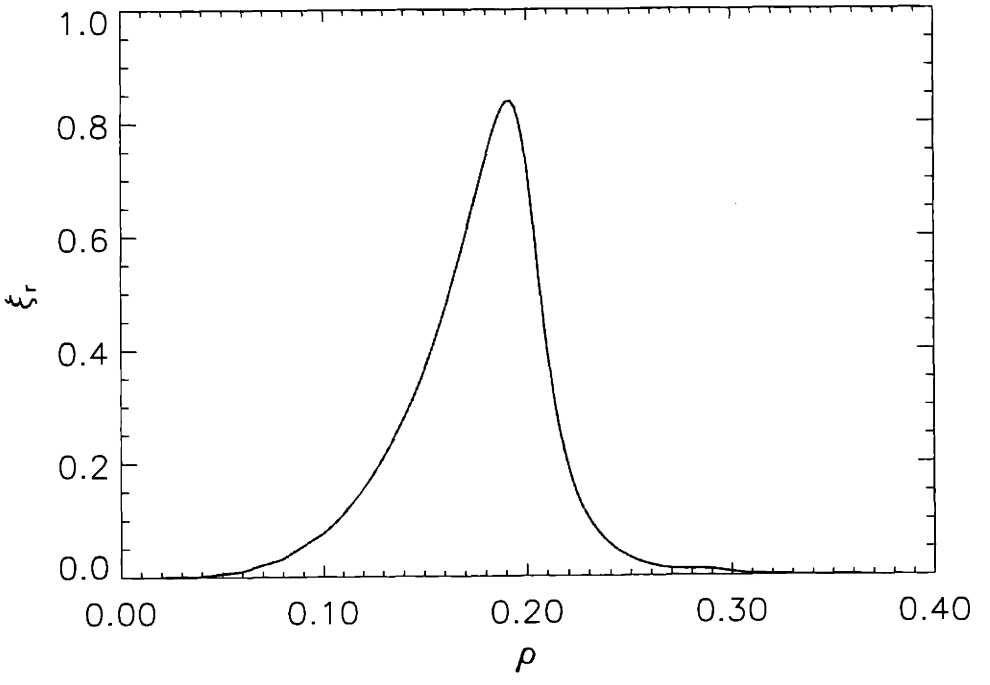

Figure 5.12: Eigenfunction based on a quasi 1-D model. The comparison with Figure 5.10 reveals the quasi 1-D model applicability.

5.3.3 The effect of finite ion Larmor radius (FLR) stabilization

The FLR modified eigenvalue [64, 70] can immediately be obtained from the ideal MHD result, calculated by e.g. the MARS code, by solving the dispersion relation,

$$\omega(\omega - \omega_{*i}) + \gamma_I^2 = 0 \ , \tag{5.7}$$

where γ_I is the ideal MHD growth rate, ω is the complex eigenvalue, $\omega_{*i} = \frac{nq}{n_e eBr}\frac{dp_i}{dr}$ (assumed constant), n is toroidal mode number, and q is safety factor. In fact, for a weak instability, inertia is only important close to the resonant magnetic surface so that only $\omega_{*i}(r = r_s)$ is required, where r_s is the resonant surface location. The result is a pair of modes with $\omega = \omega_\pm$ where,

$$\omega_\pm = \frac{\omega_{*i}}{2} \pm \sqrt{\frac{\omega_{*i}^2}{4} - \gamma_I^2} \tag{5.8}$$

Thus, when

$$\gamma_I < \frac{\omega_{*i}}{2}, \tag{5.9}$$

the ideal MHD solutions are replaced by a pair of marginally stable oscillatory modes with frequencies in the range $[0, \omega_{*i}]$, ie within the diamagnetic gap in the Alfvén continuum. Surprisingly, for an $n = 1$ ideal mode, when ω_{*i} is evaluated for the core plasma conditions in the Alcator C-Mod discharge, it turns out that inequality 5.9 is satisfied and that the ideal $n = 1$ Mercier mode is FLR stabilized. In fact, $\omega_{*i}/2 \sim 2.9 \times 10^4$, while $\gamma_{cmod} \sim 1.5 \times 10^4$ where γ_{cmod} is the growth rate predicted from the MARS code for C-Mod conditions (i.e. with $S \approx 1.25 \times 10^7$). This value is slightly different from γ_I obtained previously.

It is, however, well known [71, 72, 73] that FLR stabilization is not robust. Addition of any plasma dissipation to the equations results in destabilization of one of the oscillatory modes and damping of the other. Which mode is damped and which destabilized depends on the the precise nature of the dissipation. In the context of a two fluid analysis of internal kink modes, Porcelli and Migliuolo [71] showed that with the addition of resistivity the ω_- solution is destabilized and the ω_+ solution damped, while perpendicular ion viscosity has the reverse effect. Lakhin and Mikhailovskii [72] have found that longitudinal neo-classical viscosity is similar to perpendicular viscosity in driving ω_+ and damping ω_-. The task is therefore to identify which dissipative effect is dominant in any given situation. For the conditions of the C-Mod discharges under consideration, the following characteristic frequencies were evaluated: electron

collision frequency, ν_e; ion collision frequency, ν_{ii}; ion diamagnetic frequency, ω_{*i}, which is taken to be roughly equivalent to the mode frequency ω_+; thermal ion transit frequency, $\omega_{ti} = \sqrt{2T_i/m_i}/Rq$; and Alfvén transit frequency, $\gamma_A(\equiv \omega_A/q)$. These are listed in Table 5.1. From these results we conclude that: (i) electrons are col-

Notation	Frequency [rad/sec]
γ_A	2.5×10^6
γ_I	1.3×10^4
ω_{*i}	5.8×10^4
ω_{ti}	8.2×10^4
ν_{ii}	2.7×10^3
ν_e	2.3×10^5

Table 5.1: Characteristic frequencies

lisional ($\nu_e \gg \omega_\pm$); (ii) ions are collisionless ($\nu_{ii} \ll \omega_+$); and (iii) an oscillatory mode for which $\omega \sim \omega_{*i}$ is strongly resonant with passing ions of thermal energy, $\omega \sim \omega_{ti}$. Ion Landau damping is, therefore, likely to be the dominant form of dissipation for the upper of the two FLR stabilized gap modes, so the relevant kinetic theory is examined in the next section.

5.3.4 Kinetic theory of Mercier modes and the effect of ion Landau damping

The relevant 'inertial layer' theory for low frequency modes in the presence of ion Landau damping has been developed in a number of papers [73, 74, 75]. Solving the drift kinetic equation for the perturbed ion distribution function one finds that this contains the two sideband harmonics with $m' = m \pm 1$, which are strongly Landau resonant. Parallel ion dynamics is also affected by an electrostatic component in $E_\parallel$, so the analysis requires a consistent solution of the quasi-neutrality condition to determine this electric field. The resulting dispersion relation, Equation (21) of

Ref.[75], can be written in the form:

$$\omega(\omega-\omega_{*i})+q^2\omega\omega_{ti}[(1-\frac{\omega_{*ni}}{\omega})F(\frac{\omega}{\omega_{ti}})-\frac{\omega_{*ni}\eta_i}{\omega}G(\frac{\omega}{\omega_{ti}})-\frac{N^2(\frac{\omega}{\omega_{ti}})}{D(\frac{\omega}{\omega_{ti}})}]+\gamma_I^2(1+2q^2)=0 \quad (5.10)$$

where,

$$F(x) = x(x^2+\frac{3}{2})+(x^4+x^2+\frac{1}{2})Z(x) \quad (5.11)$$

$$G(x) = x(x^4+x^2+2)+(x^6+\frac{x^4}{2}+x^2+\frac{3}{4})Z(x) \quad (5.12)$$

$$N(x) = (1-\frac{\omega_{*ni}}{\omega})[x+(x^2+\frac{1}{2})Z(x)] - \frac{\omega_{*ni}\eta_i}{\omega}[x(x^2+\frac{1}{2})+(x^4+\frac{1}{4})Z(x)] \quad (5.13)$$

$$D(x) = (\frac{1}{x})(1+\frac{1}{\tau})+(1-\frac{\omega_{*ni}}{\omega})Z(x)-\frac{\omega_{*ni}\eta_i}{\omega}[x+(x^2-\frac{1}{2})Z(x)], \quad (5.14)$$

with $\tau = T_e/T_i$, $\omega_{*n_i} = \frac{nqT_i}{n_i eBr}\frac{dn_i}{dr}$, $\eta_i = d\ln T_i/d\ln n_i$ and $Z(x)$ the plasma dispersion function. Equation 5.10 has been solved numerically, again in collaboration with R.J. Hastie, with parameter values representing C-Mod conditions ($\omega_{*i}/\omega_{ti} = 0.71, \eta_i \sim -2$), and by varying the ideal MHD growth rate (γ_I/ω_{*i}) over the range $[0, 0.7]$, which spans the value found by the MARS code, γ_I/ω_{*i}=0.22. An unstable kinetic Mercier mode is found throughout this range. Figures 5.13 and 5.14 show the growth rate, γ/ω_{*i}, and frequency, ω/ω_{*i}, in this range.

5.3.5 Frequency comparison

For the C-Mod conditions, γ/ω_{*i}=0.27 and ω/ω_{*i}=1.34. This frequency is calculated in the reference frame of the $\mathbf{E}\times\mathbf{B}$ drift. Thus, in the laboratory frame, the mode frequency, obtained by Doppler shifting, is given by

$$\omega = 1.34\omega_{*i}+\omega_E, \quad (5.15)$$

where ω_E is the $\mathbf{E}\times\mathbf{B}$ drift frequency. To compare with the observed frequency, $f \sim$ 3.2 kHz, it is assumed that for these low energy plasmas, there is no bulk rotation in

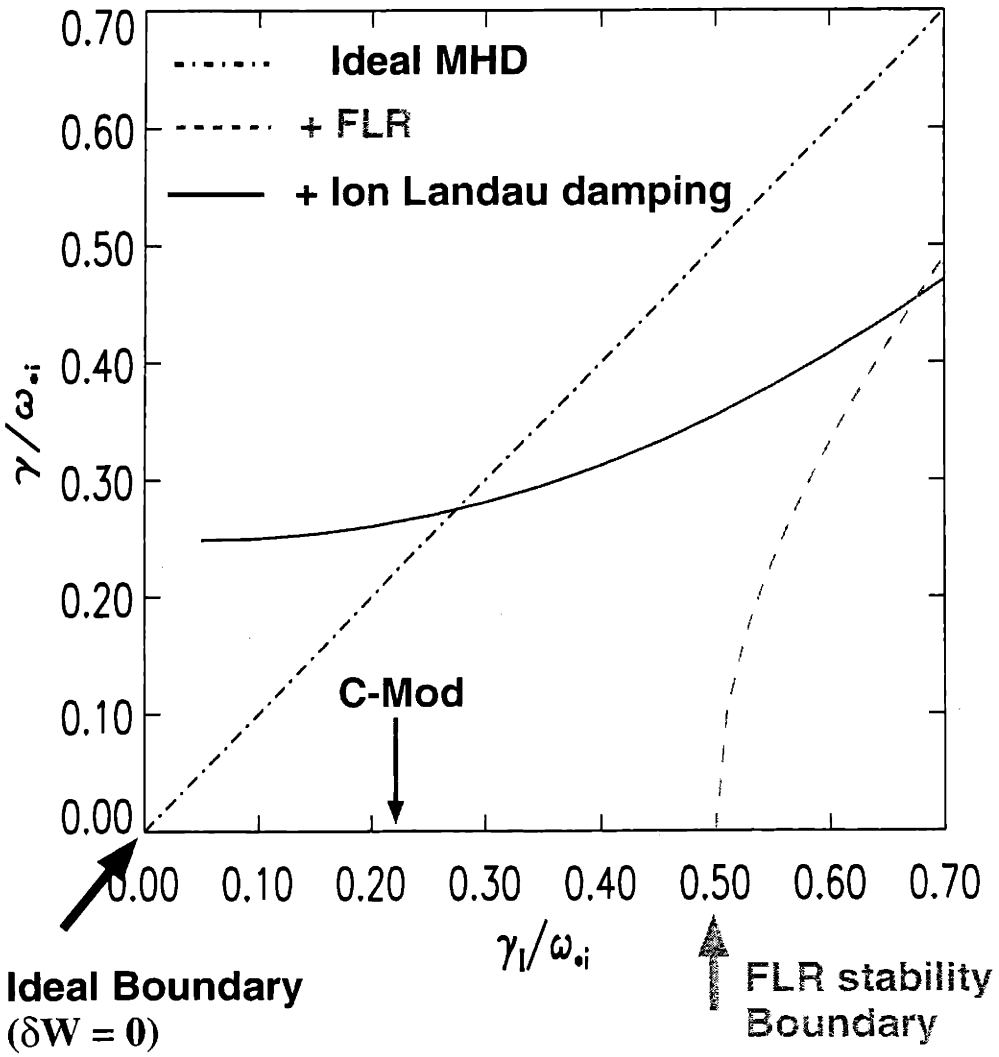

Figure 5.13: Growth rates, $\frac{\gamma}{\omega_{*i}}$. The solid curve is the predicted growth rates from solving Equation 5.10. It is based on all the contributions from ideal MHD stability, FLR effect and ion Landau damping dissipation, while the dashed and dash-dot curves result from ideal MHD with and without FLR stabilization effects. Note that any unstable mode (which may be driven by either resistivity or ion viscosity) can evolve without being hindered between the ideal boundary ($\delta W \equiv 0$) and the FLR stability boundary.

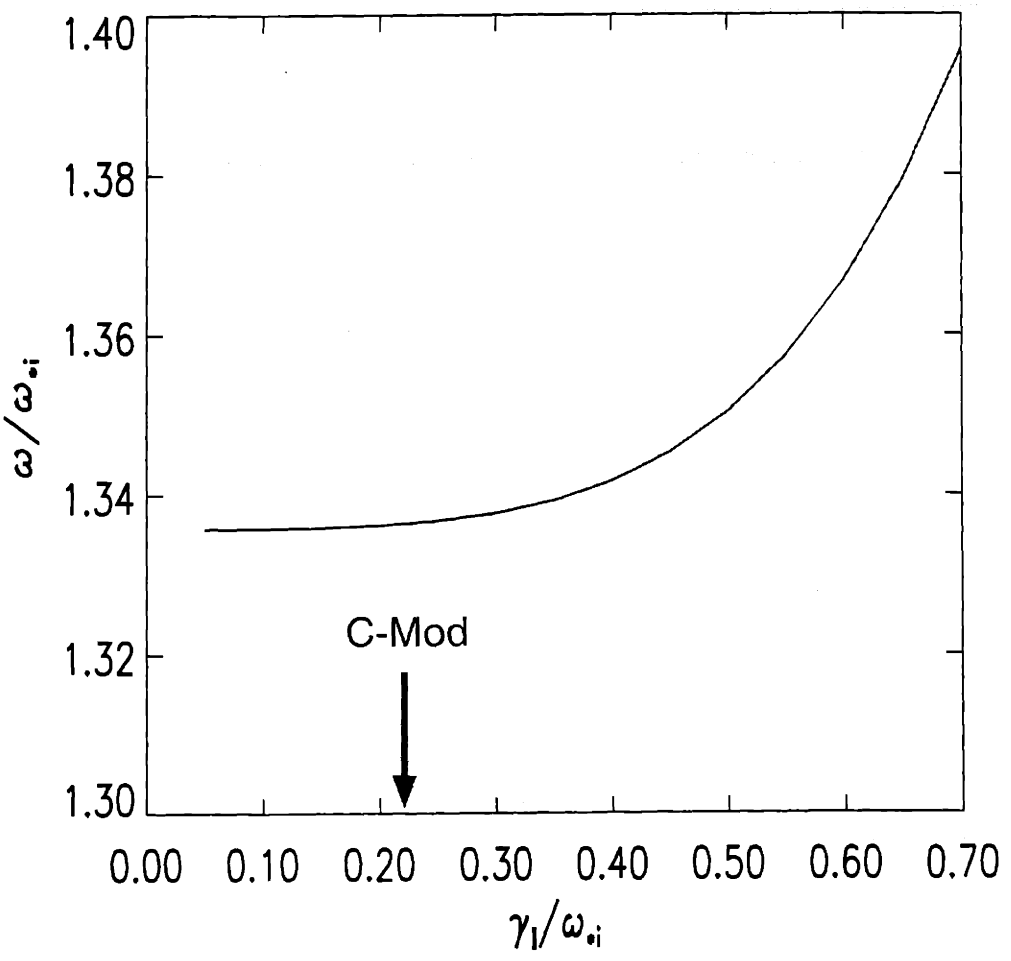

Figure 5.14: Predicted frequency (ω/ω_{*i}) in the reference frame of the $\mathbf{E} \times \mathbf{B}$ drift.

the plasma core, so that

$$\Omega_{plasma} \equiv \omega_{*i} + \omega_E = 0, \tag{5.16}$$

from which we obtain $\omega \sim 0.34\omega_{*i}$, corresponding to a frequency f_{KM}= 3.1 kHz ($f_{KM}$is the kinetic Mercier mode frequency), and in the ion diamagnetic direction, as observed. Considering that X-ray spectroscopy [76] during current ramps in typical C-Mod ohmic plasmas shows that heavy impurities have toroidal velocities as large as 50 km/sec (corresponding to a toroidal rotation frequency $f_{rot} \sim 12$ kHz) in the counter-I_p direction, the assumption of stationary bulk ions is open to question. However, as discussed in Ref. [77], the rotation of the heavy impurity ions can differ strongly from that of the bulk ions.

5.4 Discussion and Conclusions

In experiments, all the localized MHD fluctuations indicate that, at least for m=5, the Mercier instability seems to be of a relatively benign nature, possibly because of its localized nature. Higher order resonant modes at, eg $q = 4.5$, must be even more localized, and may even be stable since ion Landau resonance becomes weaker at higher mode numbers. Since $\omega \sim \omega_{*i}$ scales with the toroidal mode number n, only higher energy ions are resonant with higher frequency mode. As ion Landau damping becomes weaker, other forms of plasma dissipation must be considered and these could damp the $\omega \sim \omega_+$ mode. Resistivity, for example [71], is known to provide damping. The low frequency mode $\omega = \omega_- \ll \omega_{*i}$ must then be considered separately. In this case, the mode frequency is too low to resonate with passing ions (of thermal energy), and collisional trapped ion dissipation is most likely to be the dominant dissipative mechanism. Returning to the case of the $n = 1$ mode, we note that the kinetic Mercier instability has a substantial growth rate as $\gamma_I \rightarrow 0$, i.e as the Mercier criterion becomes marginally satisfied. For equilibria which are Mercier stable, i.e which satisfy equation 5.1, the kinetic instability can be followed as the mode moves into the Alfvén continuum, as shown by Zonca, Chen and Santoro [75]. Thus, a kinetic "Mercier" mode, driven by ion-Landau damping, rather than a resistive interchange

instability, may provide an explanation for localized fluctuations seen in discharges which are not ideal (Mercier) unstable. However, it is possible that the sawtooth-like, thermal collapse, events which are also observed in these discharges, are related to the simultaneous presence of two such Mercier modes with eg $m = 4$ and $m = 3$. Alternatively they may be related to the coupling of a Mercier mode with a double tearing mode, which is potentially more harmful than the rather benign localized mode itself.

In summary, during current ramp discharges, highly localized MHD activity was observed on GPC, whose frequency was ~3 kHz. Utilizing the additional fast GPC2 channels, the MHD fluctuations were found to be localized within 2 cm. Based on the two combined GPCs, the electron temperature profile was ascertained to be hollow, while the density profile inferred from visible Bremsstrahlung diagnostic was weakly decreasing. Assuming the thermalization time between electron and ion is short with $n_i \sim n_e$, the pressure profile was found to be hollow as well. Taking into account the pressure constraint in the EFIT program, a reversed shear equilibrium was found whose $q(0) \gg 1$. According to linear stability theory, it was determined to be unstable in both the MARS code and quasi 1-D model calculations. When a kinetic effect, such as FLR stabilization, is included, the ideally unstable mode was predicted to be stabilized, which resulted in two oscillatory modes with $\omega = \omega_{\pm}$. However, considering that i) electrons are collisional ($\nu_e \gg \omega_{\pm}$) ; ii) ions are collisionless ($\nu_{ii} \ll \omega_{\pm}$); and iii) the frequency of one of the oscillatory modes ($\omega_+ \sim \omega_{*i}$) is comparable to the thermal ion transit frequency (ω_{ti}), ion Landau damping was found to be the dominant dissipative effect, destabilizing the $\omega = \omega_+$ mode. Conclusively, detailed theoretical studies, with both MHD stability codes and collisionless ion kinetic analysis, have led to the identification of the localized temperature fluctuations as **FLR modified Mercier instabilities** with $n = 1$. Such an identification in Alcator C-Mod may therefore be the first definitive experimental observation of Mercier instability in tokamaks.

Chapter 6

Edge localized modes (ELMs) and their inferred geometrical dimensions

Since steady state high performance (H-mode) plasma is the most likely scenario for near term burning plasma experiments [17], there have been many experiments to achieve the goal with increasing input power. In H-mode plasmas, edge localized modes (ELMs), which can be characterized by 'MHD activity with quasi-periodic bursts localized at plasma edges' [78], have often been observed. During the MHD events, particles are expelled from the main plasma and the energy confinement degrades, typically by $\sim$ 15 % [79]. ELMs, however, are providing not only detrimental but also beneficial effects. For example, while ELM-free H-mode can be degraded by accumulated impurities, we can take advantage of ELMs to regulate impurities without suffering H to L back transitions. Nevertheless, some big ELMs (so called Type I or 'Giant' ELMs) seem to be more troublesome because they can damage the first wall surface materials, in that the associated heat loads to the wall exceed the limits the surface materials can endure. Thus, the understanding of ELMs has been one of the key physics issues for more than a decade. Although they are not perfectly understood yet, there is a widespread opinion that some ELMs (eg. Type I ELMs) can be

explained in terms of ballooning instability. In particular, using an $S-\alpha$ diagram [1], such ballooning characteristics are predicted in theory and have been ascertained in some experiments. Nevertheless, there is less theoretical consensus regarding smaller ELMs, such as Type III ELMs [80].

In terms of experimental observations, ELMs are challenging the spatiotemporal resolution of most diagnostics because they are not only localized at the plasma edge but also change too rapidly to resolve in time. This is a primary reason that ELMy geometric structure has not been known. As a note, before and after some ELMs, important parameters such as pedestal width and height and pressure gradient have been studied in various machines (JT-60U, JET, DIII-D, ASDEX-UG, Alcator C-Mod) [81, 82, 83, 84, 85]. However, during an ELM event itself, ASDEX-UG was the only tokamak capable of measuring the electron temperature and density profiles [86]. Only Type I ELMs, which have bigger perturbations than any other type of ELMs, have been measured in ASDEX-UG, while Type III ELMs have not. Even for the measured Type I ELMs, the poloidal structure has not been resolved. In this chapter, however, a new method is presented which has the potential to infer ELMy geometrical dimensions indirectly via ECE diagnostics [87], which may provide not only radial but also poloidal structures of ELMs. This is based on ECE refraction effects in high density plasmas, which are significant in the vicinity of the high density gradient.

In section 6.1, ELMs are briefly reviewed and C-Mod observations are discussed. In section 6.2, the signal dips seen on the ECE diagnostic during Type III ELMy bursts are analyzed in terms of refraction effects. Specifically, in Section 6.2.1, a newly developed ray tracing code is discussed and compared with a conventional code, TORAY [88]. In section 6.2.2, the ray trajectories are calculated in four steps. First, various density models and their corresponding refractive index profiles will be considered. Second, the ray trajectories outside the main plasma are found in a simple way. Third, the ray trajectories in the main plasma are found using a so called 'reciprocal' method. Fourth, the ECE signal changes for each model are calculated. In

[1] ballooning parameters[43, 78]: S - shear $(=\frac{r}{q}\frac{dq}{dr} \equiv \frac{d(\ln q)}{d(\ln r)})$, $\alpha = -2\mu_0 \frac{Rq^2}{B^2}\frac{dp}{dr}$

section 6.3, the ELM dimensions and their uncertainties inferred from the comparison with experimental observations are discussed. Then, the signal evolution will be interpreted in terms of poloidal rotation. In addition, some caveats for comparing the results with theoretical predictions are discussed. In section 6.4, the influence of Type III ELMs on the main plasmas is assessed based on the inferred density perturbation model.

6.1 Edge localized modes (ELMs)

There are two good review articles which can provide general aspects of on-going ELM research; one is the review by Zohm [79] mostly phenomenological and the other by Connor [78], theoretical. For detailed information, the reader is referred to the references the two articles cited.

6.1.1 Classifications

There are several types of ELMs, of which Type I, III and dithering ELMs are described here. In general, Type I ELMs are characterized by big D_α burst and high heat loading to the wall, whereas there is no magnetic precursor. As the input power (P) increases, the ELM repetition frequency (ν_{rep}) increases, too (ie. $d\nu_{rep}/dP > 0$). This has been explained in terms of an ideal ballooning stability limit, which is probably coupled with another ideal MHD instability such as an ideal kink [79, 83, 89]. For Type III ELMs, rather bursty but little D_α is observed, with magnetic precursors. The associated mode numbers (m/n) are usually identified to be high. As the input power goes up, the ν_{rep} of Type III ELMs decreases and they disappear eventually. Noting that there is an upper limit to the edge T_e at which these ELMs occur, a plausible explanation for Type III ELMs is resistive ballooning instability, which might be coupled with an external kink mode. In dithering H-modes, D_α is observed to move up and down but the repetition frequency is reduced, compared with Type III ELMs. This is believed to occur when the plasmas go in and out of H-modes repeatedly in a 'limit cycle'. The ELMs described above tend to occur at different input powers.

If the auxiliary power is increased, dithering, Type III H-modes, ELM-free H-modes, and then Type I ELMs may be observed successively. Such an interesting example is shown in Zohm's review [79]. Historically, the ASDEX group modeled Type III ELMs successfully as a so called 'peeling mode', where the edge localized pressure profile expands and peels off outwardly, as shown in the Figure 6.1. Recently, ELMs have

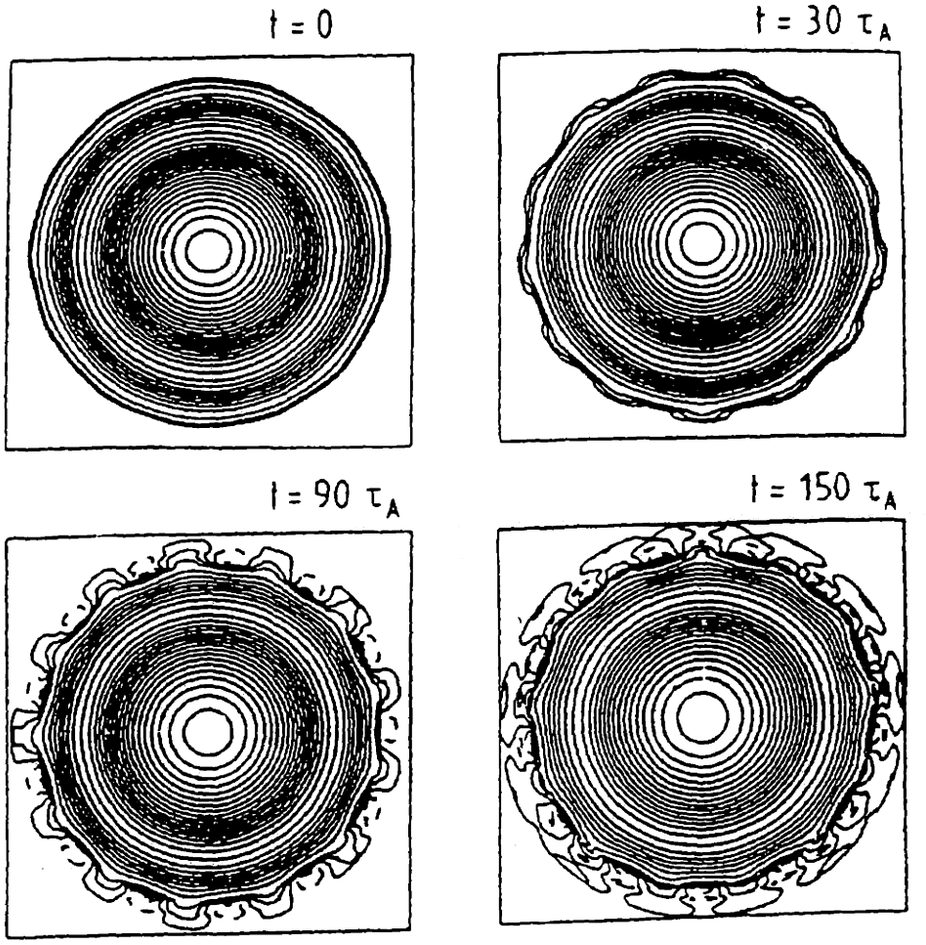

FIG. 92. Contour plots of the pressure for the non-linear evolution of free-surface modes.

Figure 6.1: Peeling mode model contour plot. This figure was imported from the H-mode studies of the ASDEX group (Ref. [90]).

been modeled as a combination of a ballooning mode (driven by pressure gradient) and a peeling mode (driven by current density) [80]. Thus, Type III ELM density

models for this study, as will be shown in Section 6.2.2, have been constructed with reference to such 'peeling' mode-like structure, in which poloidal variations need to be considered.

6.1.2 ELMs in Alcator C-Mod

In Alcator C-Mod, Type III ELMs and dithering have been observed frequently, while Type I ELMs have not. However, there is a rather unique regime called 'enhanced D_α (EDA)' H-mode in C-Mod, in which the impurities are extracted steadily without having intermittent instabilities. Because EDA H-modes do not degrade in time, since they release not only impurities but also their radiation losses steadily, this is regarded as one of the most favorable operational scenarios in future tokamaks. Returning to the ELM phenomena, the absence of Type I ELMs in C-Mod is possibly due to the limited input power. However, in some cases, the pressure gradients are near or above the first ballooning limit [90]. As a newly reinforced RF auxiliary power system (up to 7 MW) is expected to be operational in 2000, we may be in a better position to see whether Type I ELMs can be seen in C-Mod. In general, Type III ELMs in C-Mod plasmas have clear degradation in terms of energy confinement time [90, 91], compared with good ELM-free or EDA H-modes.

Type III ELMs on ECE diagnostics of Alcator C-Mod

Figure 6.2 shows the experimental observation of rather unusual Type III ELMy bursts. On the left top five time traces, we can clearly see that there are signal drops during Type III ELMs on GPC, whose operating frequency is the 2nd harmonic X-mode. At first, it was surprising to see T_e drops on core channels because ELMs are generally considered to be "edge-localized". This motivated the author to initiate the search for other explanations. On the other hand, positive signal spikes are seen on the right five time traces, which show signals from the fundamental harmonic O-mode radiometer. At the same time, on a divertor Langmuir probe, we observed similar spikes in ion saturation currents, which implies that there were intermittent radial

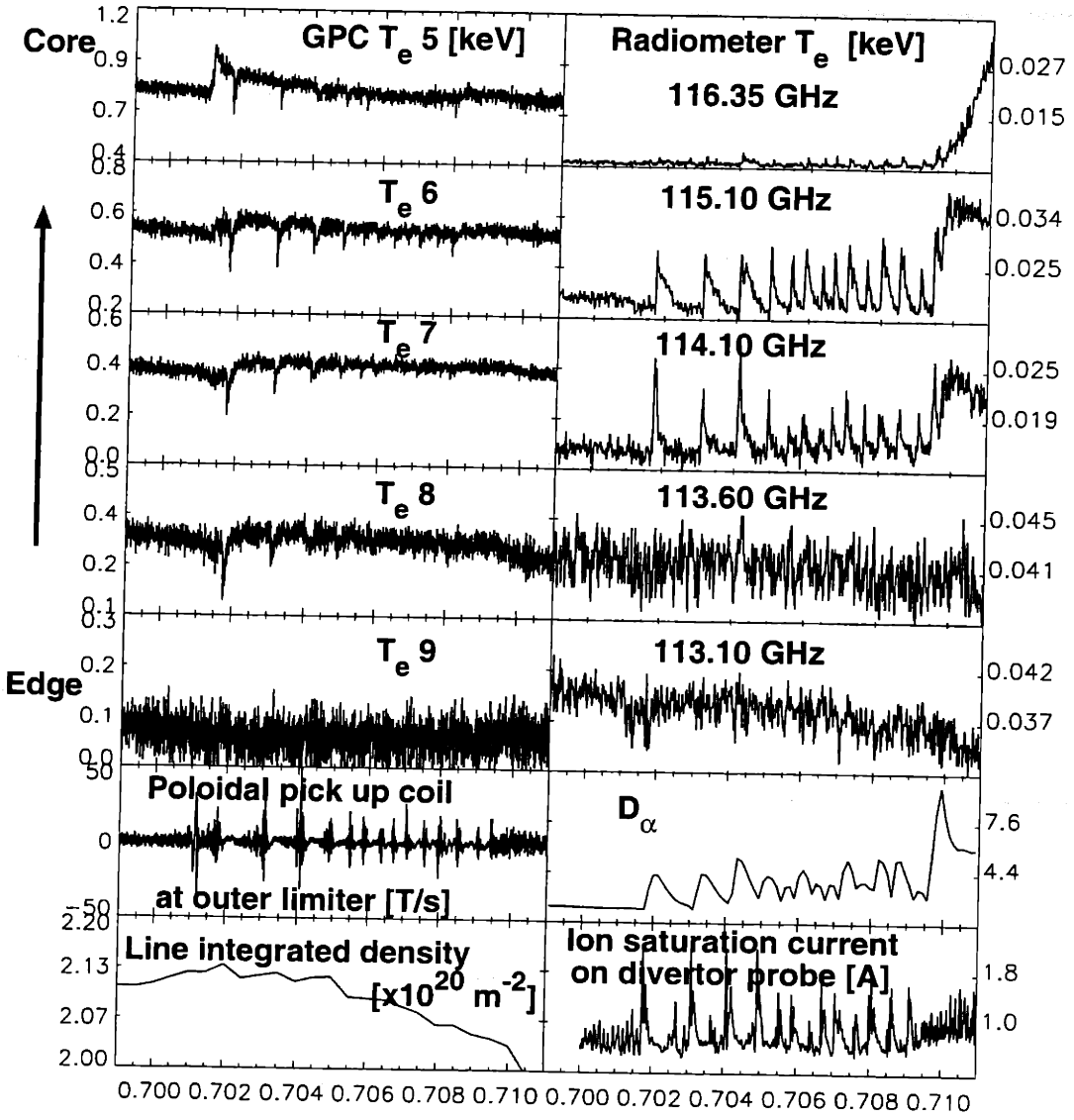

Figure 6.2: Signal drops on the 2nd harmonic X-mode GPC at each ELM, while signal increases on the fundamental harmonic O-mode radiometer. On the ion saturation current of divertor probe, similar spikes are observed. The magnetics show the toroidal mode number (n) is as high as 14.

particle fluxes coming from the main plasma. Based on the magnetic analysis, the associated toroidal mode number of this particular case was ~14, while the poloidal mode number could not be determined not only due to 2π phase shift ambiguity but also from the negligible signals on inboard magnetic pick up loops (this is also evidence that this type of MHD has 'ballooning' character). It should be noted that such signal drops on GPC were observed only in rather high density plasmas. Figure 6.3 shows the fractional changes of the GPC during the Type III ELMy bursts. When the electron temperature fractional changes are defined as $\Delta T_e/T_{avg} \equiv (T_{max} - T_{min})/T_{avg}$, Ch 5 and Ch 7 showed approximately 25.7 and 43.6 % drops. Figure 6.4 shows all the associated density profiles at the approximate time of the ELMy bursts. In particular, the GPC and radiometer density cutoffs vs R are found based on the conditions of $\omega_{pe}^2/\Omega_{ce}^2 = 2$ and $\omega = \omega_{pe}$ respectively (See Equations 2.19 of Chapter 2). Hence, it seems unlikely that the whole density profile was enhanced to cause density cutoff of core channels in this case.

Based on the circumstantial evidence, there were two initial ideas regarding the phenomenon of core ECE dips at ELMs; **density cutoff or refraction effects**. For the density cutoff hypothesis, if highly narrow density spikes block the view of the ECE collection optics, there could be some reduced signals from evanescent waves. For refraction effects, we need to consider that any ray trajectory is affected by the first derivative of the refractive index, not only by the value of refractive index itself.

Density cutoff vs refraction effects

A rough estimate of the density spike thickness required to explain the ECE dip based on density cutoff may be calculated from the following equation;

$$\Delta x = \ln(\frac{P_0}{P})/(2\kappa_{im}) \tag{6.1}$$

where P_0 and P are the signal intensities before and during the ELMy bursts and κ_{im} is the imaginary part of $N\omega/c$. The e-folding length was found to be in the submicron range, so if the thickness (Δx) is as large as 1 mm, we should have almost

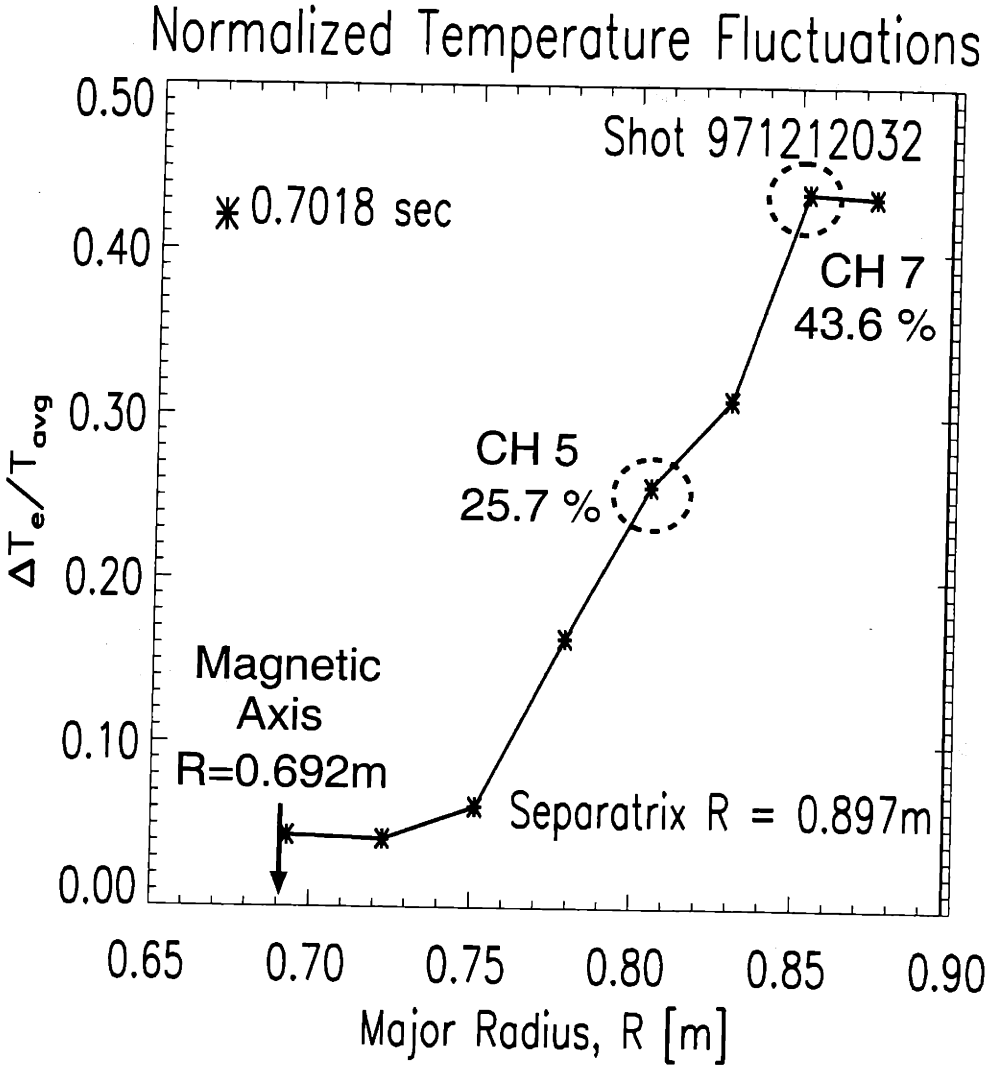

Figure 6.3: Fractional changes of GPC during Type III ELMy bursts. Overall, 10 $\sim$ 50 % fractional changes were observed. In particular, the changes (26 and 44 %) of Ch 5 and Ch 7 are referenced to check whether a model is appropriate or not.

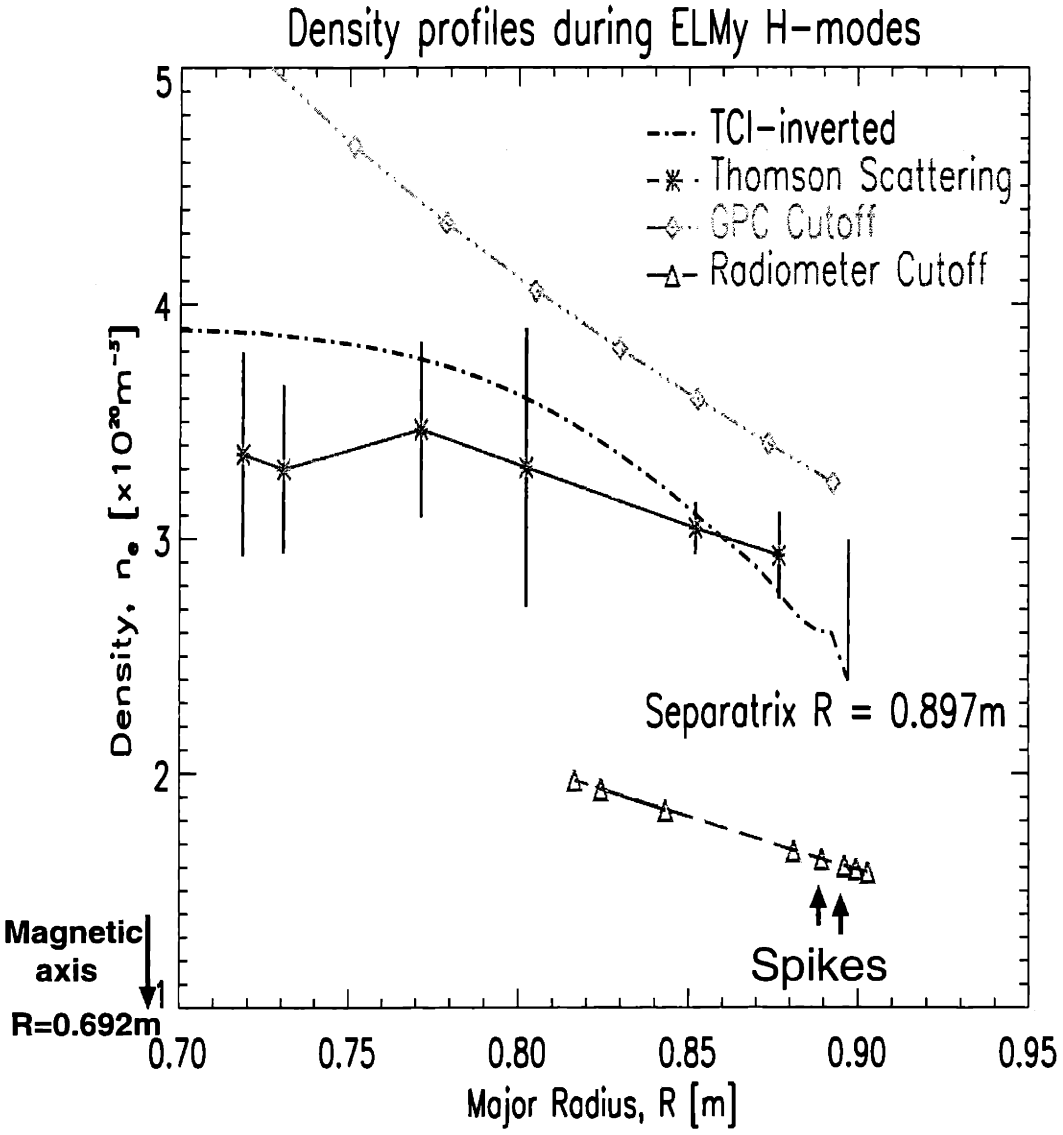

Figure 6.4: Density profiles based on measurements and cutoff conditions. TCI-inverted and Thomson scattering density profiles are from measurements. On the other hand, the GPC and radiometer cutoff density profiles are derived from the density cutoff conditions associated with the second harmonic of X-mode and the fundamental harmonic of O-mode respectively. Near the separatrix, two radiometer channels are noted for the signal spikes, which implies that the local density should be lower than their corresponding cutoff densities ($\approx 1.5 \times 10^{20} m^{-3}$).

no signals during density cutoffs (like right after pellet injection). Considering that the signal drops are in the range of 10 to 50 %, it is very unlikely that the signal drops are caused by such density cutoff. On the other hand, the refraction effect is a good candidate to explain such signal drops but needs to be calculated using a ray tracing code for comparison, which is a complex task. The detailed procedures will be described in the following section.

6.2 Refraction effects during ELMs

6.2.1 Ray tracing code

In the past, a ray tracing code in the electron cyclotron frequency range called TORAY has been successful for general purposes. However, it is inappropriate for accommodating any poloidal variations. For the ELM models we are considering, poloidal variation is essential for modeling refraction effects. Hence, a new ray tracing code that is capable of handling poloidal changes was needed and has been developed.

Ray equations

For perpendicular propagation of X-mode waves, the dispersion relation $D = D[N, \Omega_{ce}^2, \omega_{pe}^2, \omega]$ (e.g. Equation 2.9) becomes

$$D = 1 - N^2 - (\frac{\omega_{pe}}{\omega})^2 \frac{\omega^2 - \omega_{pe}^2}{\omega^2 - \omega_{UH}^2} \tag{6.2}$$

where $N^2 = (ck/\omega)^2$, $\omega_{pe}^2 \propto n(\mathbf{x})$: density and $\Omega_{ce} \propto |\mathbf{B}(\mathbf{x})|$: magnetic field. Using the dispersion relation, the ray equations can be found as follows [88];

$$\begin{aligned} \frac{d\mathbf{x}}{dt} &= \frac{-\frac{\partial D}{\partial \mathbf{k}}}{\frac{\partial D}{\partial \omega}}, & \frac{d\mathbf{k}}{dt} &= \frac{\frac{\partial D}{\partial \mathbf{x}}}{\frac{\partial D}{\partial \omega}} \\ \frac{d\mathbf{x}}{ds} &= -sgn(\frac{\partial D}{\partial \omega}) \frac{\frac{\partial D}{\partial \mathbf{k}}}{|\frac{\partial D}{\partial \mathbf{k}}|}, & \frac{d\mathbf{k}}{ds} &= \frac{\frac{\partial D}{\partial \mathbf{x}}}{|\mathbf{V_g}| \frac{\partial D}{\partial \omega}} \end{aligned} \tag{6.3}$$

, where $\mathbf{V_g}$ ($\equiv \frac{d\mathbf{x}}{dt}$) is group velocity and $s = |\mathbf{V_g}|t = |\frac{d\mathbf{x}}{dt}|t$ is the arc-length. Considering the axisymmetric characteristics of the tokamak, no toroidal angle dependency is included for this analysis. Since the toroidal variation is expected to be smaller than the poloidal one (ie. $\lambda_{\|} > \lambda_{\perp}$), the toroidal length of the ECE collection optics aperture has been set to be slightly larger than the poloidal length. The position vector ($\mathbf{x}$) and its wavevector ($\mathbf{k}$) can then be described in 2-dimensional form; i.e. $\mathbf{x} = \mathbf{x}$ (x,y), $\mathbf{k} = \mathbf{k}$ (k_x, k_y). Thus, the solutions of the four coupled ordinary differential equations (ODE) provide the ray trajectory. The key component of this ODE solver is LSODE, whose routine is provided in IDL 5.2 (the latest version, as of 2000, available in C-Mod group).

Benchmarking with TORAY code

To benchmark the newly developed code with TORAY, a simple monotonic density profile has been assumed and some sample ray trajectories were found for low ($n_0 = 4 \times 10^{20} m^{-3}$) and high ($n_0 = 7 \times 10^{20} m^{-3}$) density cases. As shown in Figures 6.5 and 6.6, the ray trajectories agreed well within 0.5 % error. The slight difference between TORAY and the new code near the resonant layer of Figure 6.5 comes from the fact that the thermal effects are considered in TORAY, while the new code is based only on the cold plasma approximation (See Chapter 2). However, since we are interested in the location of the beam at the resonance layer, rather than the deposited absorption power, such thermal effects do not cause any problem for further analysis. Similarly, the case in which the density exceeds the wave cutoff has also been ascertained to give proper reflection in both calculations, as shown in Figure 6.6. Thus, the newly developed code has been successfully benchmarked with the conventional ray tracing code, TORAY.

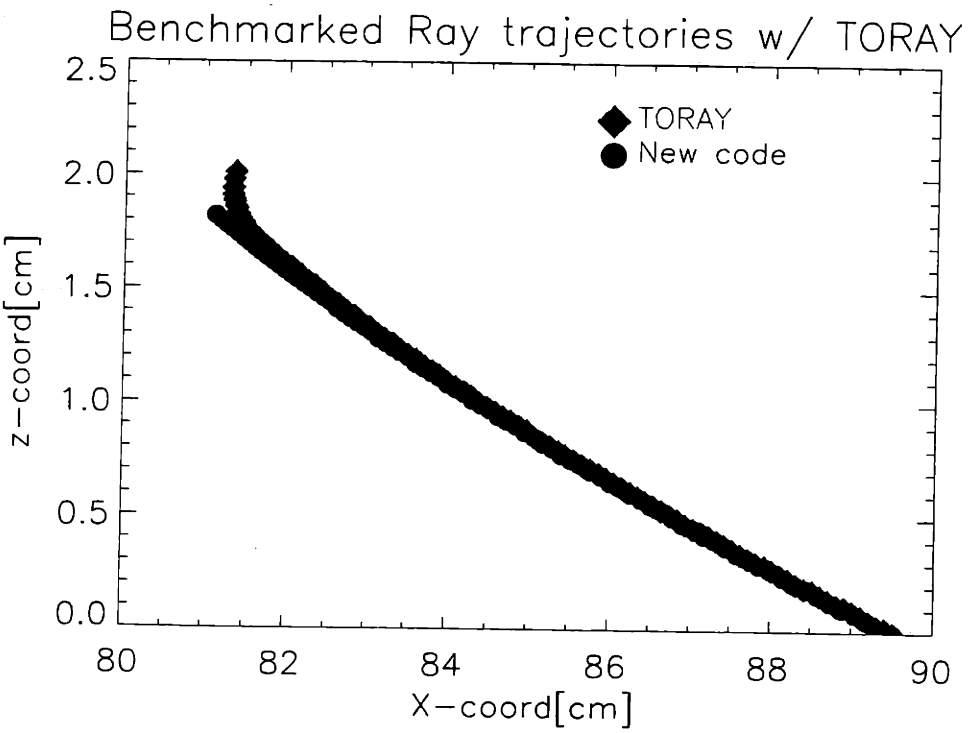

Figure 6.5: Resonance layer benchmarked with TORAY. The positions at the resonance layer (R=81.3 cm) agree well between two calculations. The bent trajectory of TORAY reflects the fact that thermal effects are considered for power absorption, while the straight trajectory of the new code is based on cold plasma approximation only.

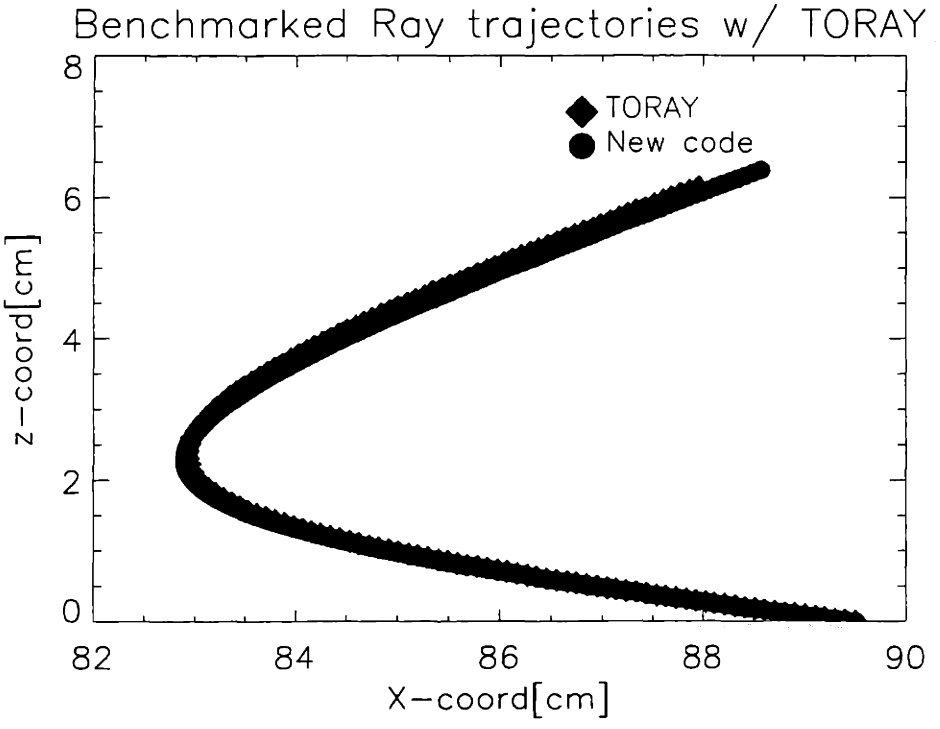

Figure 6.6: Density cutoff benchmarked with TORAY. Both the ray trajectories agree well. Near R=82.9 cm, the cutoff occurred and the ray trajectories reflected back.

6.2.2 Refracted ray trajectories

Density models including poloidal variations

Four types of density models have been considered; a) reference b) hump c) dip d) dip without bank cases. All the other density profiles are compared with a reference density profile (monotonic). The referenced density profile ($n_0 = 3.66 \times 10^{20} m^{-3}$) has been determined based on the Thomson Scattering density profile (See Figure 6.4). The four types of density profiles at the midplane are shown in Figure 6.7. The asso-

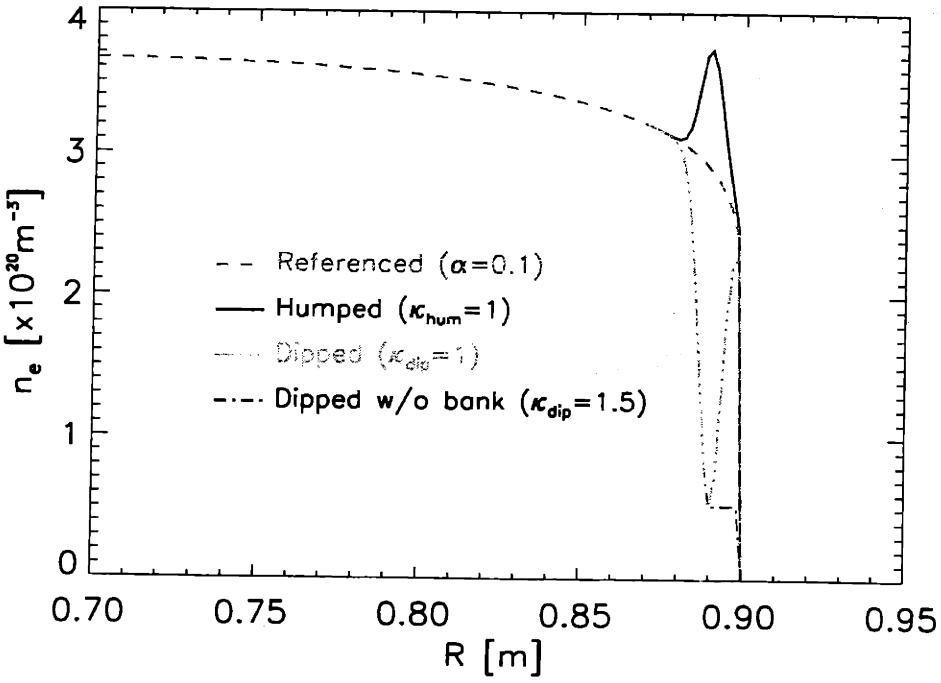

Figure 6.7: Density profiles at the midplane

ciated density surface plots near the midplane edge, displaying the assumed poloidal and radial variations, are shown in Figure 6.8. The density hump case (b) of Figure 6.8) was at first regarded as most likely because it could most easily explain the signal drops on GPC. This is physically plausible in the sense that the higher density leads to smaller refractive index, which becomes more sensitive to density changes. However, it does not explain the signal spikes observed on fundamental O-mode radiometer. In particular, considering that the signal spikes occurred in the midst of

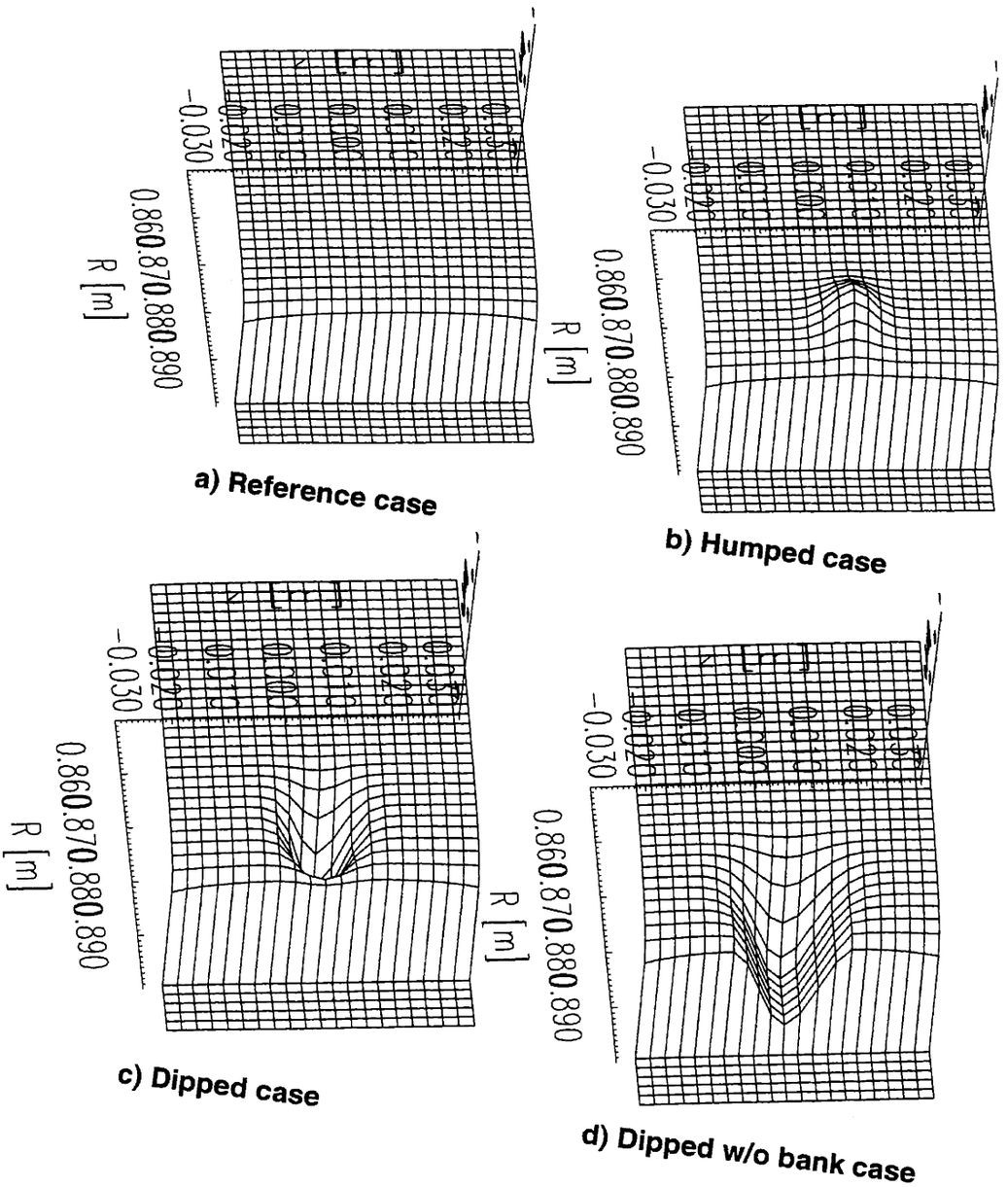

Figure 6.8: Density models near the midplane. The reference case (a)) has a typical monotonic density profile. Model b), c) and d) have been made to describe the ELMy phenomena. As we shall see later, the model d) turns out to be the most likely.

density cutoffs of the O-mode radiometer, the local density near the channels showing those spikes should be lower than between ELMs. The opposite case (density dip case c) of Figure 6.8) has also been investigated. However, this model also has unrealistic feature in that the density 'bank' next to the density trough is so high as to prevent the fundamental harmonic O-mode radiometer from receiving emission. Finally, perhaps the most plausible density profile has been modeled as density dip without edge bank, as shown in d) of Figure 6.8. In this model, the particles are ejected from the main plasma and the edge density decreases monotonically in R, which satisfies various aspects on different diagnostics (eg. signal drops on GPC, signal spikes on O-mode radiometer and Langmuir probes). Compared with the previous examples, this one has not been represented by a simple analytical formula. However, numerical manipulation allowed us to explore the model. The analytical form adopted for this analysis is as follows;

$$n[x,y] = n_0 \left[1 - \frac{x^2 + \frac{y^2}{\kappa^2}}{a^2}\right]^{\alpha} \pm \sum_{j=1}^{N} q_j n_0 \exp\left[-\left(\frac{s_j}{b_j}\right)^2\right] \tag{6.4}$$

where n_0 is peaked density, a minor radius, κ elongation, α peakedness, N-Number of humps (dips), j : j-th hump (dip),

$$s_j \equiv \sqrt{\{(x-\alpha_j)\cos\theta_j + (y-\beta_j)\sin\theta_j\}^2 + \frac{\{-(x-\alpha_j)\sin\theta_j + (y-\beta_j)\cos\theta_j\}^2}{{\kappa_j}^2}}$$

s_j pseudo distance, q_j weighting, b_j half of the hump (dip) width, θ_j tilted angle, κ_j hump (dip) elongation, and (α_j, β_j) hump (dip) center position.
When the second term of RHS of 6.4 is absent, it gives the reference case (a) of Figure 6.8). When the sign of this term is positive or negative, it represents the humped and dipped cases respectively. For the model d), the density is the same as the model c) up to the radial position of the density trough, while the density and poloidal density gradients outside of the density trough have been set to be equal to those at the density trough.

There are many free parameters we can adjust. For example, the width (b_j),

height (q_j), elongation (κ_j), rotation angle (θ_j), and radial position (α_j, β_j) are five key parameters. Figure 6.9 shows the definition of each parameter. For initial calculations, the radial position has been fixed near R=0.89 m, which is 1 cm away from the last closed flux surface (LCFS). This was determined from the O-mode radiometer observation, in which the signal spikes were located near R=0.89 m, while no other channels of the O-mode radiometer showed changes. In addition, the local density of the center of ELMs at the midplane should be less than the cutoff density of the associated channels ($\approx 1.5\times10^{20}m^{-3}$) of the O-mode radiometer. $0.5\times10^{20}m^{-3}$ was used for most runs. The rotation angle has been set to have the center of ELMs located at the midplane. There are two reasons for fixing the rotation angle at the midplane. First, if there had been two minima observed in the signal dips, we could infer that the minima occurred with the perturbations off the midplane. However, as we had one minimum signal drop, it can be assumed that the ELM perturbation should be symmetric with respect to the midplane. Second, as will be shown later, a density perturbation located at the midplane gives the most signal changes. Hence, we may take advantage of the up-down symmetry of the calculations, so all the calculations started from the upper right quadrant of the plasma cross-section. In addition, the density perturbation has been assumed to be rotating poloidally, which may explain the smooth decrease and increase of the GPC signal levels near the minima. In the ray tracing program, the radial and poloidal lengths (eg. width and elongation) are inputs. These two parameters characterize the physical dimensions of the radial and poloidal density perturbation at each ELM. The associated refractive index profiles for two wave frequencies are shown in Figure 6.10. Since the frequency of Ch 5 (256.4 GHz) is higher than that of Ch 7 (241.3 GHz), its refractive index profile changes more slowly.

Ray trajectories in vacuum collection optics

The collection optics outside of the main plasma are of course fixed and define which rays leaving the plasma will be detected. To provide starting rays, the optical system has been modeled. As described in Chapter 2, two focusing mirrors are in the form

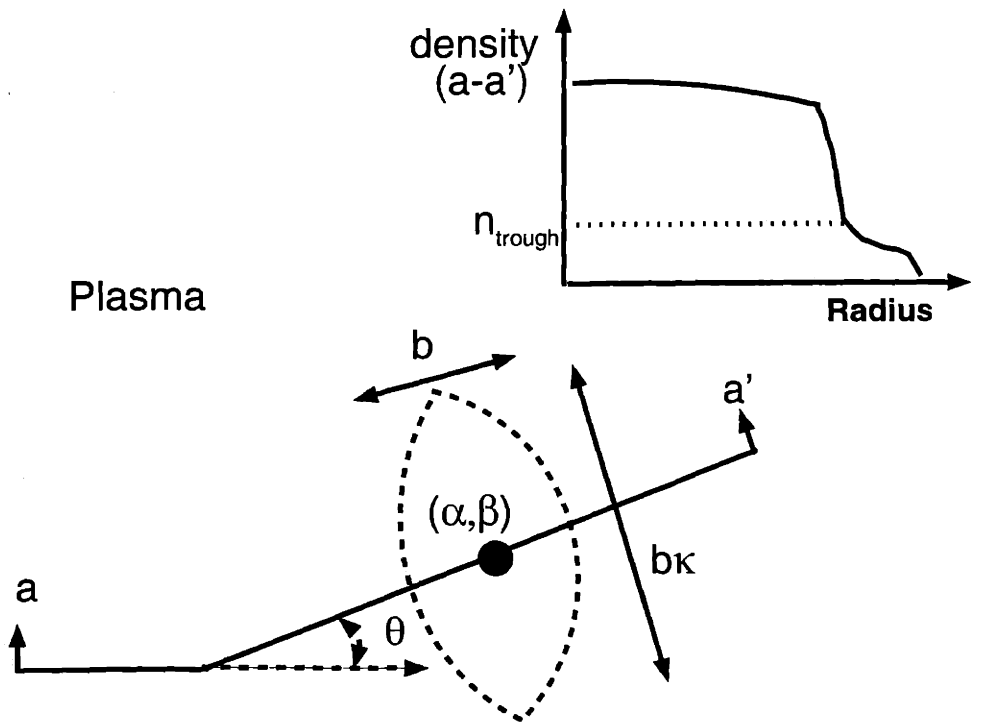

Definitions

(α,β): center position

b: width

κ: elongation

θ: rotation angle

n_{trough} : local density at trough

Figure 6.9: Definitions of key parameters. The schematic density profile (a-a') shows the local density height (i.e. n_{trough}) and all the other definitions are self-explanatory in this figure.

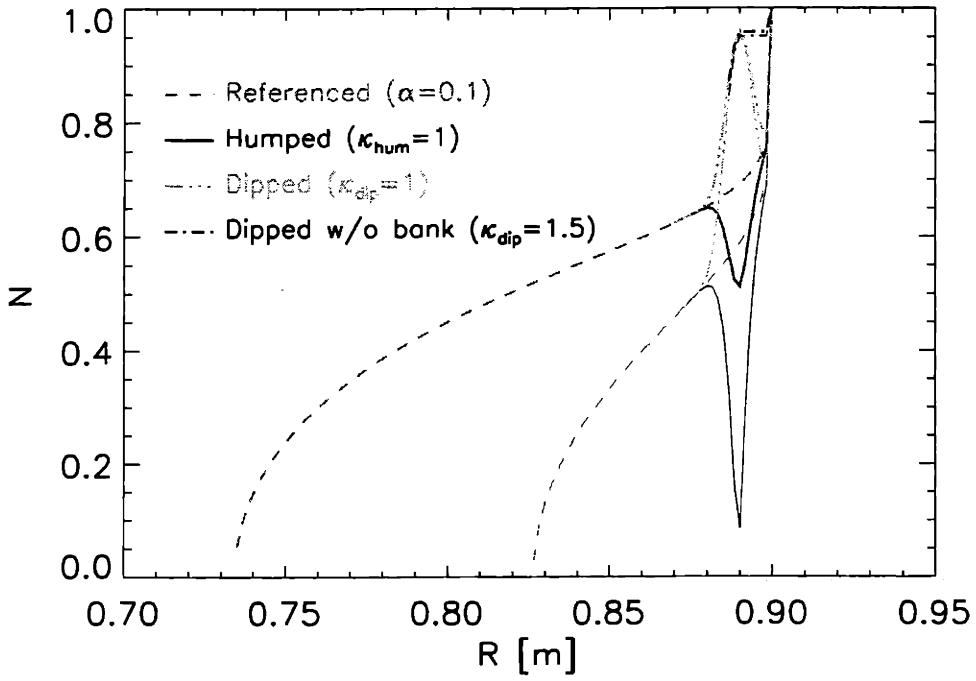

Figure 6.10: Refractive index profiles at the midplane

of an ellipse with a minor diameter of 20.3 cm and a major diameter of 28.7 cm with $f = 2.7$ m focal length. Considering that the aperture of the collection optics is 3 cm $\times$ 5 cm rectangle and that the poloidal length is narrower by 3 cm, the detector aperture was chosen to be 3 cm diameter. The length of the optical system up to the defining aperture is $4f$=10.8 m. Based on this model, the one-to-one corresponding rays between object and image on the detector have been found using OPTICA [92] and used for reference values for further ray tracing analysis. Figure 6.11 shows the schematic diagram of the ray trajectory calculations using OPTICA. The starting point was chosen to be radially located at R=0.90 m, which is just outside the LCFS. It is 25 cm from the nominal plasma axis (R_0 = 65 cm), which is the focal point of the first elliptic mirror. As illustrated in the bottom of Figure 6.11, the upper and lower limits at each height (z) at the R=0.90 m reference line were determined by assessing whether or not each ray could reach the aperture whose diameter is 3 cm. The calculated collectible angles ($\Delta\theta$) from each height are shown in Figure 6.12.

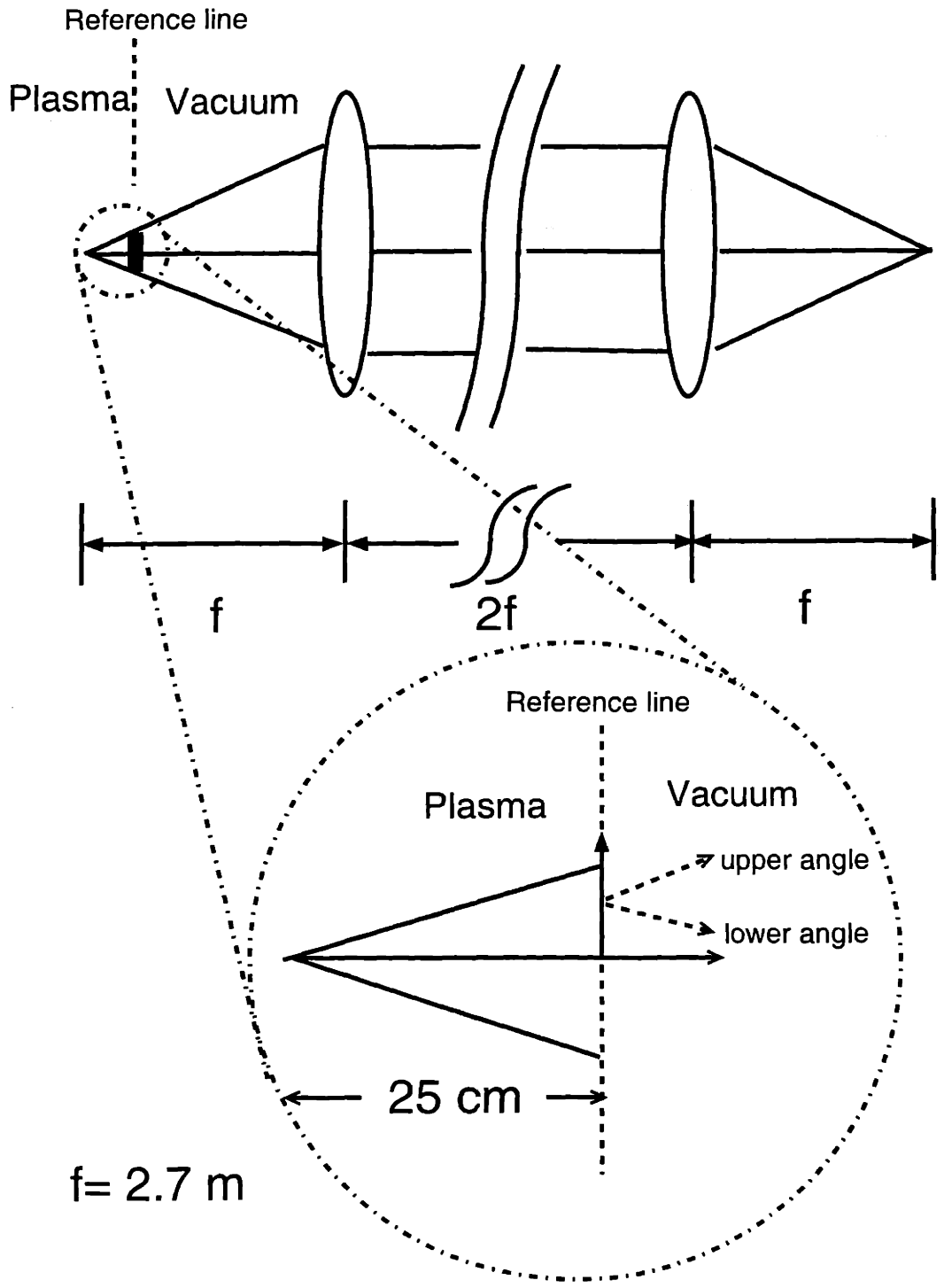

Figure 6.11: Schematic diagram of the ray trajectory in vacuum collection optics using OPTICA. The distance between two elliptic mirrors is $2f$=5.4 m, and each optical component is scaled down from the real experimental setup.

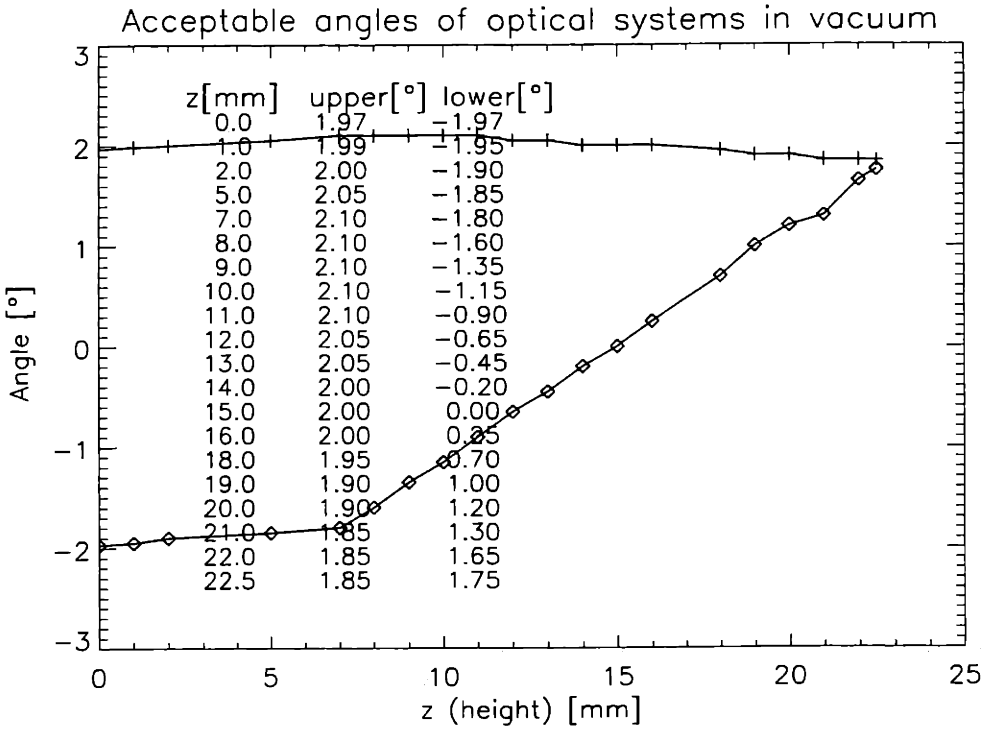

Figure 6.12: Collectible angles vs height in vacuum collection optics. The upper and lower limits of the angles are found using OPTICA. Near $z = 15$ mm, the lower limit becomes zero.

Ray trajectories in the main plasma

The main purpose of this investigation is to see whether the rays which are accepted by the collection optics are refracted by ELMs so that they see colder regions. To minimize the number of calculations, a reciprocal method has been used. 'Reciprocal' means a ray tracing is performed from vacuum into plasma, rather than from plasma to vacuum. In general, every ray which connects an object and its image has one-to-one relationship so the ray trajectory can be found in either way equivalently. In a forward method, each possible ray trajectory needs to be checked individually to see whether it can make it into the collection optics. However, in a reciprocal method, a few ray trajectories, which have already been verified to be accepted in the collection optics, are enough. As a note, such a reciprocal method for an ECE ray trajectory is equivalent to a forward method for an electron cyclotron resonance heating (ECRH) ray trajectory, which is actually launched from vacuum into the plasma region. In this regard, an ECRH ray tracing program, like TORAY, could have been an effective tool to calculate ECE ray trajectories. However, as TORAY cannot accommodate poloidal variations, all the models except the reference case needed to be run in the newly developed ray tracing code. Each figure shown here represents the best fit parameters found for each model. The detailed calculations are described below.

Each density perturbation model has been fully explored in terms of its width and elongation. As shown in Figure 6.13, three ray trajectories leaving from each point at a specific height were investigated; upper, middle and lower angle cases. The upper and lower angles were chosen based on the previous calculation related to vacuum collection optics, while the middle angle was the arithmetic average of the two limiting angles. To interpret the results in terms of their effect on temperature measurements, the middle angle has been selected for representing each point concerned. In general, the variations between the upper and lower angle cases were not significant in terms of height and temperature (z, T_e). To minimize any calculation errors, the mesh size (Δz) between two adjacent points was chosen to be no more than 3.8 mm. Figure 6.13 shows the reference case, where we can clearly see that all the rays of Ch 5 and Ch

7 are concentrated within 2 cm of the midplane, as they should be. The solid curves show the trajectories from the upper and lower angles, while the dotted curve shows the trajectory from the middle angle. The dashed contour plot shows the refractive index, with spacing 0.025 for Ch 5 and 0.05 for Ch 7, and the solid vertical line is located at the resonant layer for each frequency near the midplane. In the contour plot, the radial refractive index gradient near the LCFS can be seen to be large because this reference case is modeled for an H-mode (eg. peakedness α=0.1 in Eq. 6.4). Although these two figures show three ray trajectories from each of 20 points, the following figures use 60 points, but consider only the middle angle to avoid overly complicated plots. It was checked for a few cases that taking 180 rays does not change the pattern.

Figure 6.14 shows the density hump case. In this model, the density hump acts like a concave lens in optics. Apparently, the ray trajectories which started closer to the midplane on the bottom figure are bent so drastically as to see the vacuum region. Thus, such rays have negligible contributions in the signal estimation of electron temperatures. The refraction effect in the top figure (higher frequency) is not so drastic as that in the bottom figure. Although the estimated signal drops, about which the detailed procedures will be explained later, (eg. 7.4 and 49.5 % on Ch 5 and 7 respectively using a Gaussian weighting) were close to the values from the experimental observation (26 and 44 %), there was no reasonable combination of the adjustable parameters to explain the underestimated change of emission on the high frequency channel (Ch 5).

Figure 6.15 shows the dip case with a Gaussian density perturbation. This model is opposite to the previous density hump case. Thus, the density dip acts like a convex lens. However, it looks like an overfocusing lens. It is found that the ray trajectories which started slightly off the midplane were refracted most. This suggests that a certain ray trajectory near the edge of the perturbation is refracted most in the curved surface of the density dip model. In this model, the refraction effects could be described a little better than in the density hump case, in that the estimated signal changes (16.0 and 45.2 %) are closer to the experimentally observed changes.

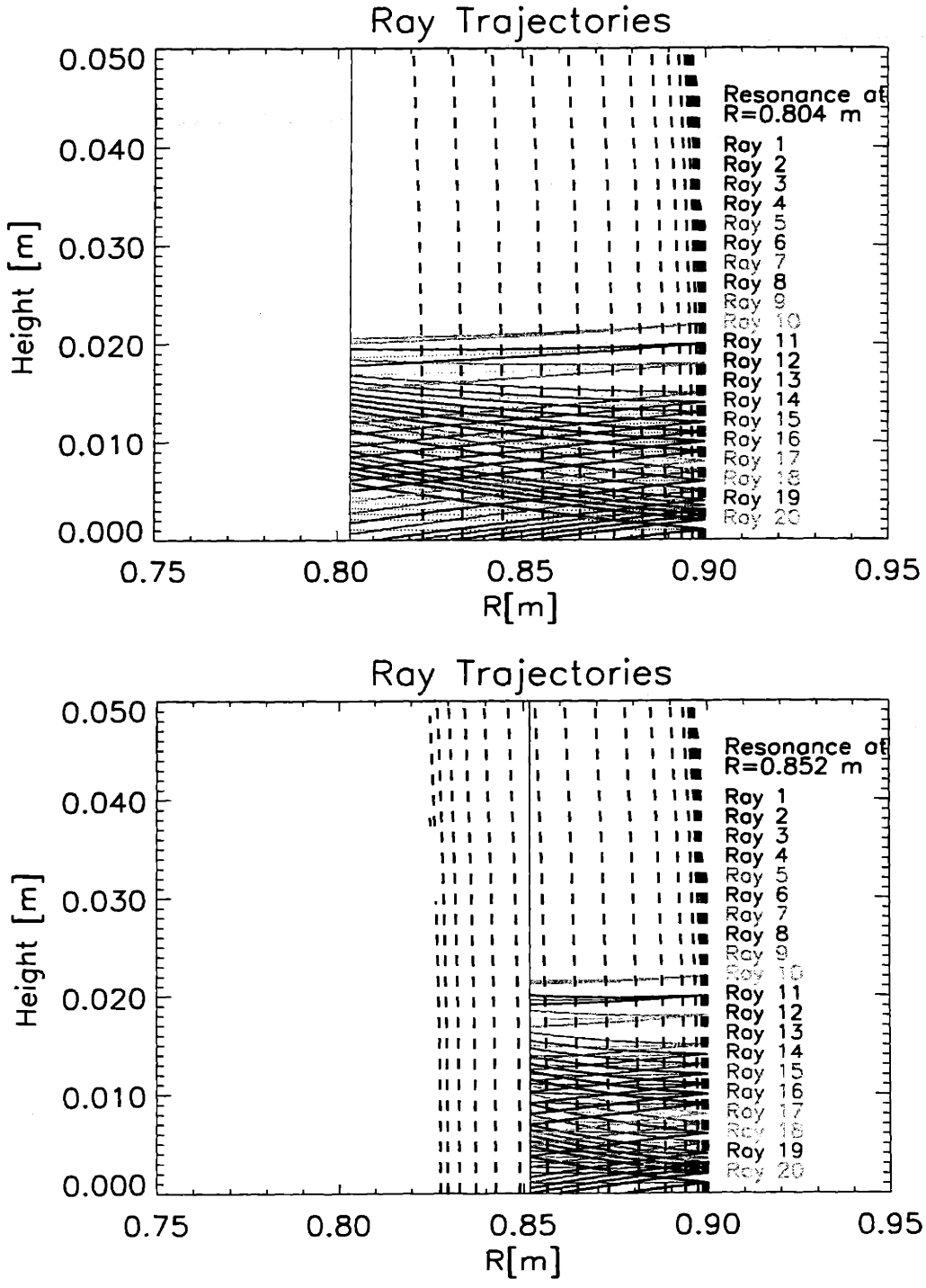

Figure 6.13: Ray trajectories of Channel 5 and 7, whose resonance layer are at R =0.804 m and 0.852 m respectively. Note all the rays are near the midplane. These are the reference cases.

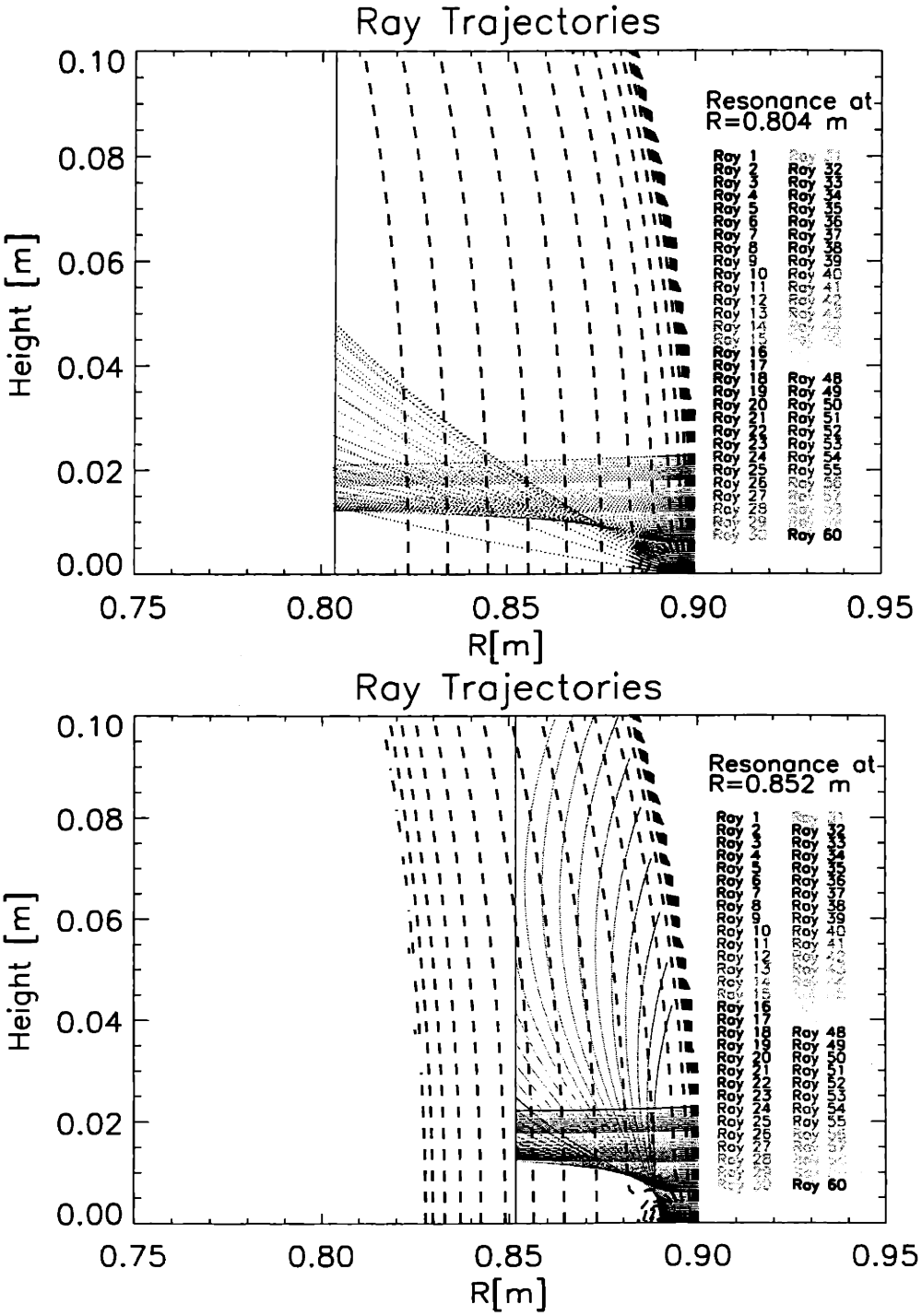

Figure 6.14: Ray trajectories of Channel 5 and 7. Due to density hump, the ray trajectories are bent. 7.4 and 49.5 % signal changes respectively are estimated using Gaussian weighting, while 4.5 and 26.6 % signal changes are estimated using constant weighting.

However, the density 'bank' outside the density trough is unrealistic from a particle transport standpoint, as mentioned in Section 6.2.2.

Figure 6.16 shows the case with constant n_e outside the dip. In comparison with Figure 6.15, the contour plot of the ELM outside a certain radial position near the LCFS shows the refractive index is varying only in the poloidal direction. Like the density dip case above, there is a certain poloidal position slightly off the midplane where the ray trajectories are refracted most. In addition, the radial and poloidal lengths of the perturbed region were found to be critical. For example, when the elongation, which is related to poloidal length, changes from 1 to 1.5, Ch 5 shows a factor of 2 change, which will be discussed later. As a result, the most probable parameters that may explain the experimental observations were found based on this model. Although it is not presented here, another density model was tried in which only radial variation was assumed without poloidal variation. The density profile of this model at the midplane was exactly the same as that of the density hump case and it was extended poloidally without showing poloidal variation. In this model, the ray trajectories were found almost the same as the reference case, which predicted insignificant signal changes. That implies that radial gradients of refractive index are not important for determining the ray trajectories, while poloidal gradients are indeed critical.

Estimation of ECE signal perturbation

All the physical quantities, including electron temperature (T_e) and density (n_e), are assumed to be constant at each flux surface, except in the vicinity of the perturbation. Each modeled density profile, which assumed elliptical density surfaces, is valid when such quantities are well aligned with respect to the actual C-Mod flux surfaces. As shown in Figure 6.17, the electron temperature and density in the big circle region are valid under the aforementioned assumption and can be mapped back to the equivalent midplane quantities. For example, if a ray reaches the point 'a' in Figure 6.17, it is mapped onto the midplane position ('b'). Then, the corresponding temperature is found. Therefore, if a ray reaches a point outside the valid region, the mapping may

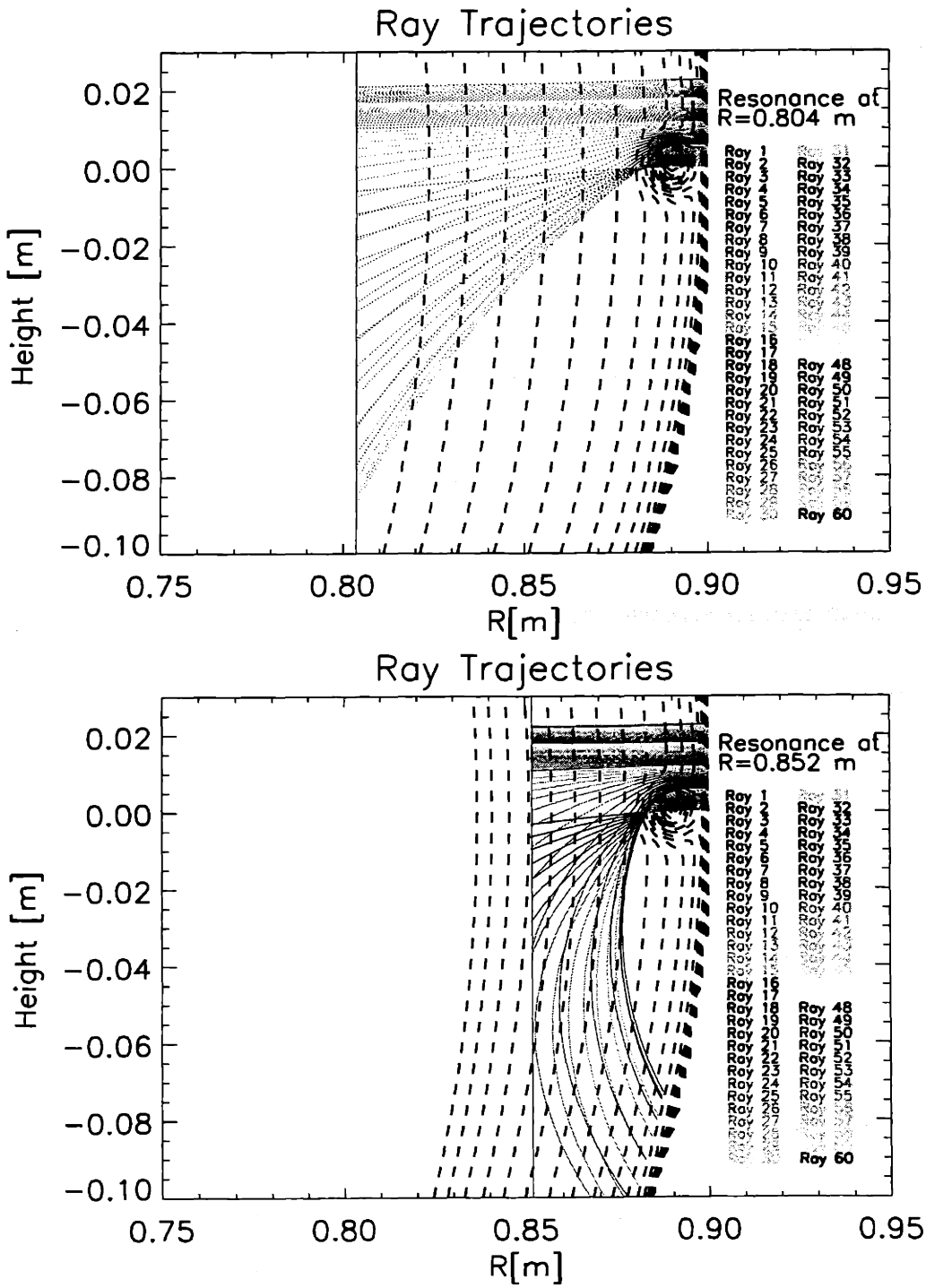

Figure 6.15: Ray trajectories of Channel 5 and 7. Due to the poloidally localized density dip, the ray trajectories are refracted drastically. 16.0 and 45.2 % signal changes respectively are estimated using Gaussian weighting, while 10.7 and 33.5 % signal changes are estimated using constant weighting.

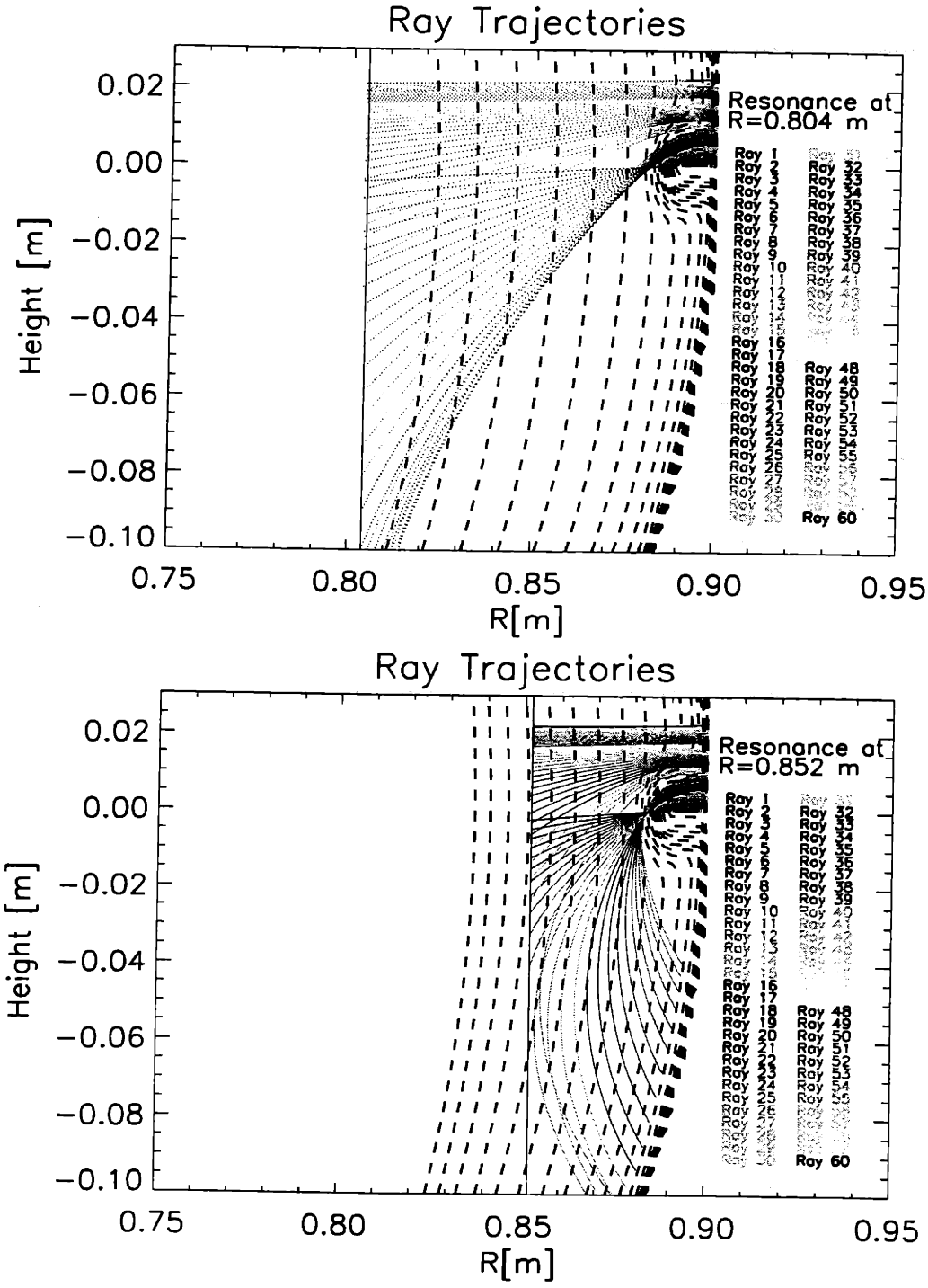

Figure 6.16: Ray trajectories of Channel 5 and 7. Due to the density dip without a bank at larger radii, the ray trajectories are bent enough to be consistent with the experimental observation. 23.2 and 41.8 % signal changes respectively are estimated using Gaussian weighting, while 21.3 and 39.1 % signal changes are estimated using constant weighting.

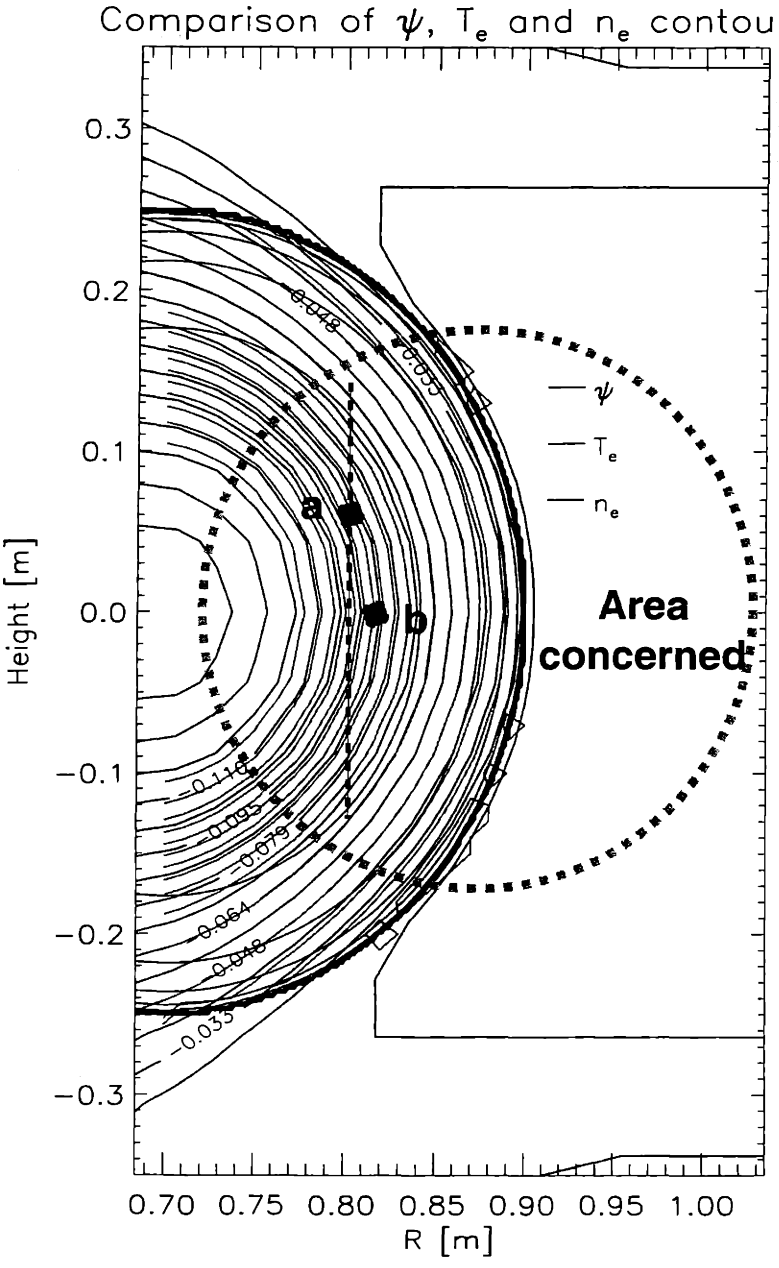

Figure 6.17: Comparison with ψ, T_e and n_e. The big circle represents the valid region for mapping each physical parameter. For example, the temperature of point 'a' is mapped onto that of point 'b'. However, if a ray reaches a point outside the big circle, the associated temperature may cause some error but it gives negligible contribution. For example, the resonance layer (R ~0.852 m) for Channel 7 is located within the valid region, while part of the resonance layer ($R \sim$ 0.804 m) for Channel 5 near the edge may contribute to some small errors.

be in error. In the cases discussed here, most of the rays are located in the valid region, while a few rays, that give negligible contributions, are refracted beyond the circle. Hence, the validity of the effective temperature calculations is generally acceptable. To interpret the ray trajectory results, it should be noted that the etendue ($A\Omega$ where A is area and Ω is solid angle) is conserved for any ray tracing case. As illustrated in Figure 6.18, the etendue is proportional to $(\Delta\theta)$ and (Δz) because

$$A\Omega = \frac{A_1 A_2}{d^2} \propto \frac{(d\Delta\theta)(\Delta z)}{d^2} \propto \frac{(\Delta\theta)(\Delta z)}{d}. \tag{6.5}$$

The total collected signal (I) is approximated by

$$I = \sum_j I_j = (const) \cdot \sum_j T_j (A\Omega)_j w_j \tag{6.6}$$

where T_j is the temperature from blackbody radiation at the emission layer (assuming 'optically thick' plasmas), and w_j is the weighting. The signal changes can then be found by

$$\frac{\Delta I}{I} = \frac{I - I'}{I} = \frac{\sum_j [T_j - T_j'](A\Omega)_j w_j}{\sum_j T_j (A\Omega)_j w_j} = \frac{\sum_j [T_j - T_j'](\Delta\theta)_j (\Delta z)_j w_j}{\sum_j T_j (\Delta\theta)_j (\Delta z)_j w_j} \tag{6.7}$$

where I and I' are the signal intensities before and during the ELM perturbation respectively, $(\Delta\theta)_j$ is the collectible angle, and $(\Delta z)_j$ the vertical spacing of the rays. The weighting factors (w_j) associated with the aperture cannot be described as a simple step function and need to be determined considering the edge effects, or, so called 'vignetting'. According to Hsu's investigation about the aperture edge effects in our optical system [2], the weighting can be given as the dashed curve in Figure 6.19. Two extreme weightings (Gaussian and constant) drawn in solid curves of Figure 6.19 were considered in the calculations. As will be discussed later, the signal change estimation is only weakly dependent on the shape of weighting factors.

Figure 6.20 shows the variation of fractional T_e changes in terms of poloidal elongation (κ_{hump}) for the density hump model. Since the practical weighting is between

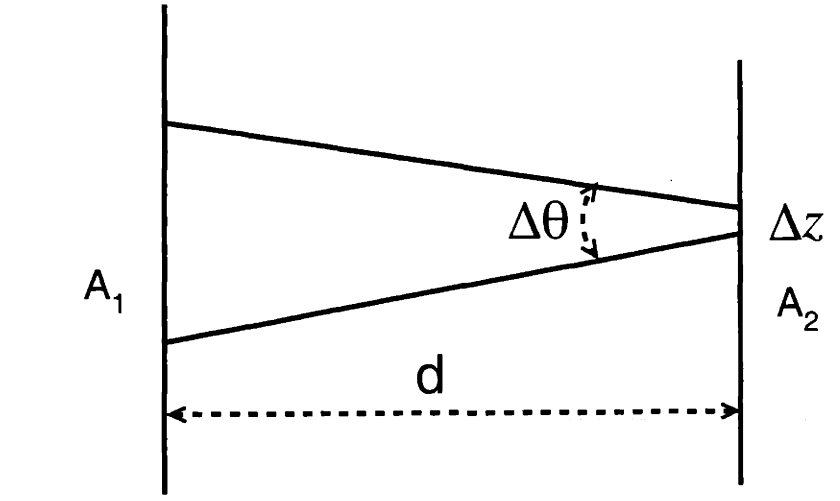

Etendue

$$A\Omega = \frac{A_1 A_2}{d^2}$$

Figure 6.18: Etendue (AΩ) calculation.

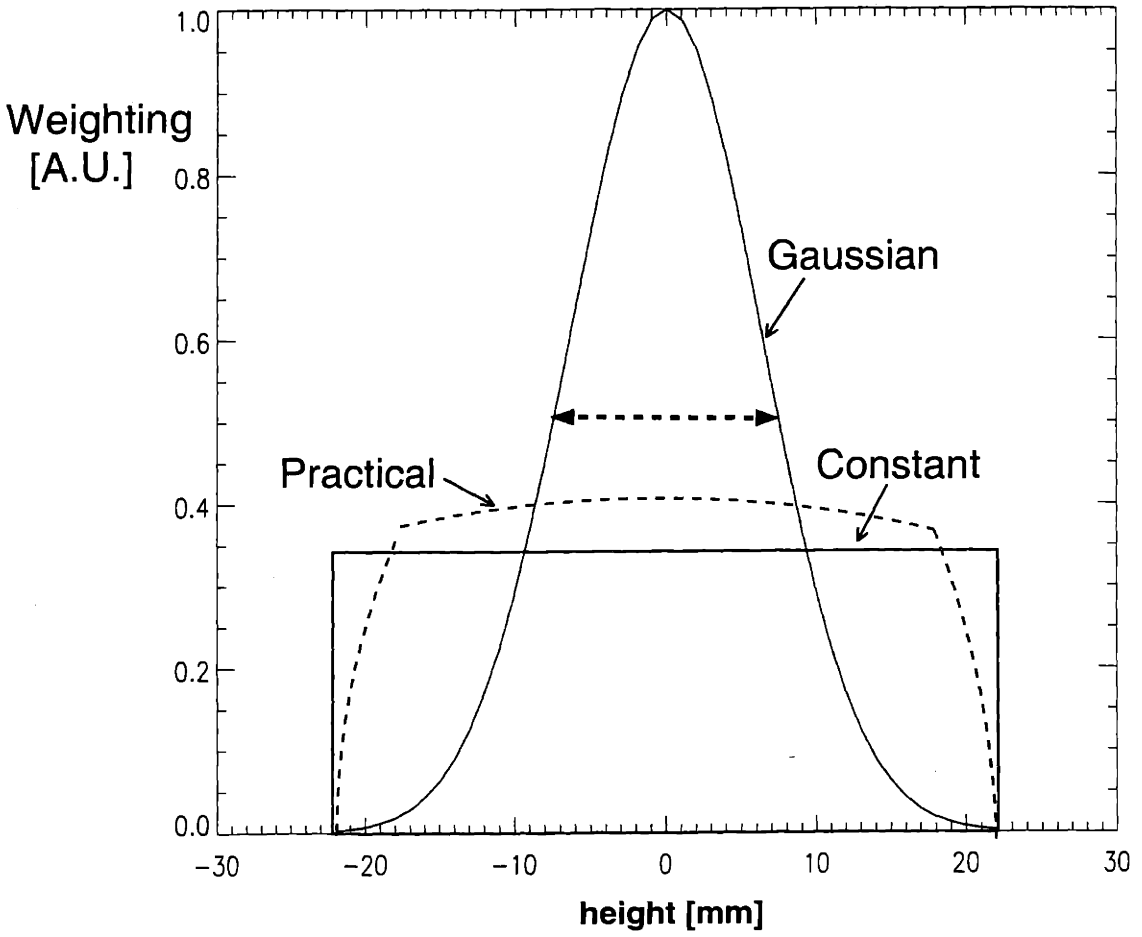

Figure 6.19: Weighting function ($w_j = w_j(z)$). In practice, the vignetting at the edge of the ECE collection optics aperture requires weighting factors, as shown in the dashed curve. Two extreme cases (Gaussian and constant weighting) were considered in these calculations. In fact, the signal change estimation is weakly dependent on the shape of weighting factors.

the two extreme weightings, the case with $\kappa_{hump} = 1$ is found to be the closest to the experimentally observed changes. The peak edge density for this investigation is $3.8 \times 10^{20} m^{-3}$, which gives a refractive index of the low frequency wave (Ch 7) of $\sim$ 0.1, close to the cutoff condition. If the density goes down, the fractional changes will drop, which implies that the signal drop of the high frequency wave (Ch 5), which is well below the experimentally observed change (26 %), will always be underestimated in this model. Similarly, Figure 6.21 shows the fractional T_e changes in terms of

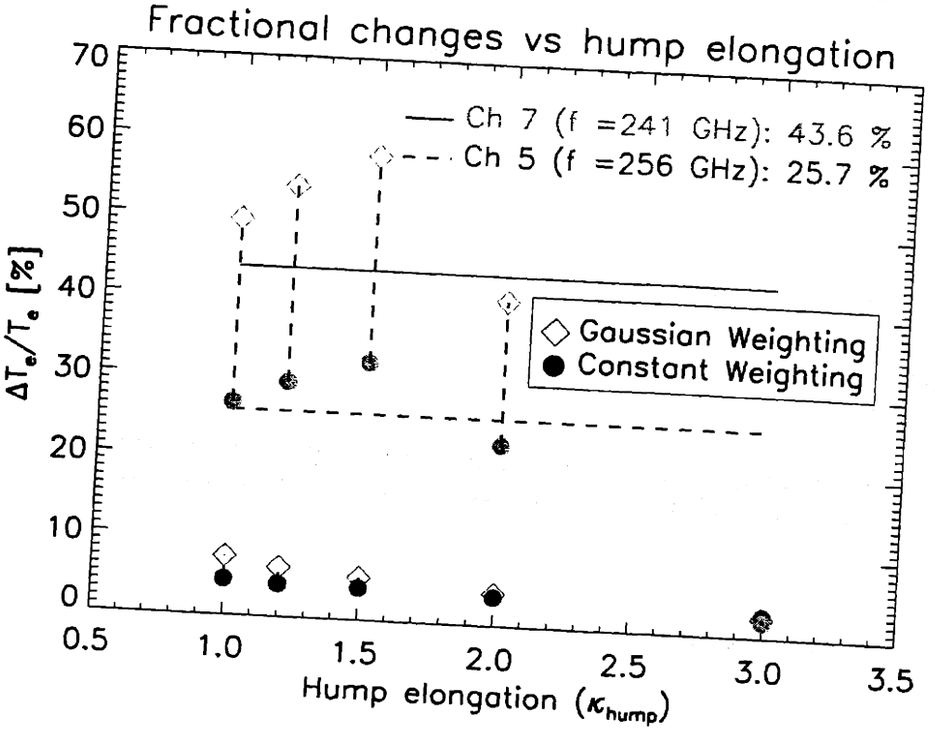

Figure 6.20: Fractional changes of T_e vs poloidal hump elongation. Horizontal lines represent the experimentally observed fractional changes of Ch 5 and Ch 7 of GPC respectively. The estimated signal changes of $\kappa_{hump} = 1.0$ are the closest to the experimentally observed changes.

poloidal elongation (κ_{dip}) for the density dip model. The case with $\kappa_{dip} = 1$ is the closest to the situation observed in experiments. The lowest density was set to be $n_{trough}^{ELM} = 0.5 \times 10^{20} m^{-3}$, which is well below the cutoff density of the fundamental O-mode radiometer. The dependences of the density dip without edge bank model will be discussed in the following section separately.

Considering all the aforementioned contributions, Table 6.1 summarizes the signal

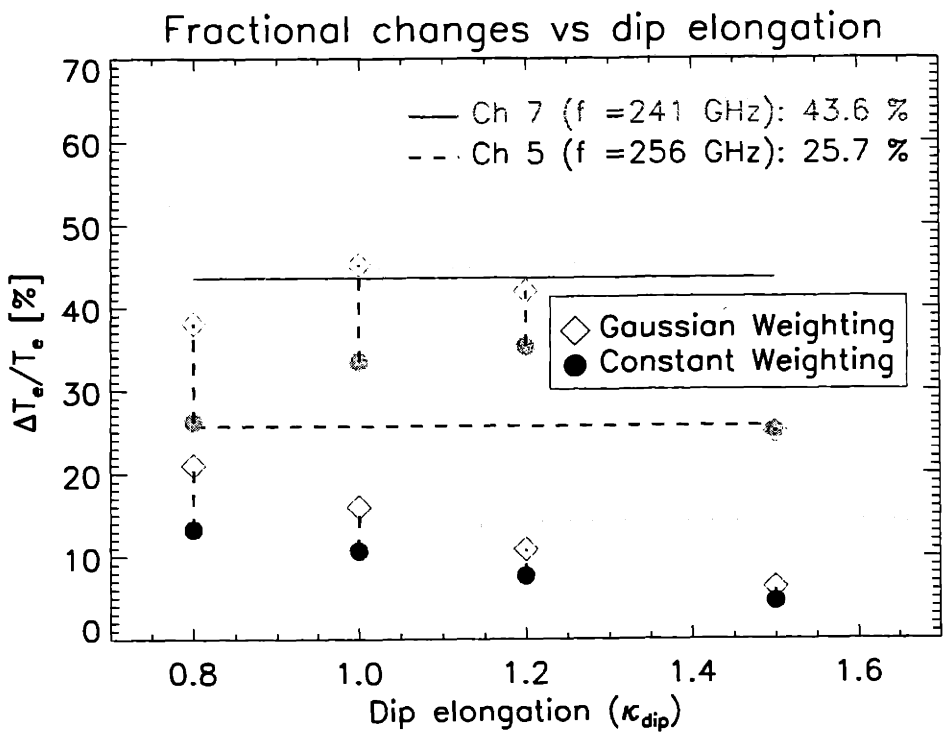

Figure 6.21: Fractional changes of T_e vs poloidal dip elongation. Horizontal lines represent the experimentally observed fractional changes of Ch 5 and Ch 7 of GPC respectively. The estimated signal changes of $\kappa_{dip} = 1.0$ are the closest to the experimentally observed changes.

changes of Ch 5 and Ch 7 for the three density models in comparison with experimental observation. Each case in this table was the best in that the estimated signal changes were closest to the experimentally observed changes. For example, the density dip model with $\kappa_{dip} = 1.0$ shown in Figure 6.21 predicts that the fractional changes of Ch 5 and Ch 7 respectively are 10.7 and 33.5 %, given constant weighting. Depending on the type of weightings, there are some changes in hump and dip density models. However, for the dip without edge bank model, which is regarded as the most physically realistic, there are no significant changes between Gaussian and constant weightings. Thus, the perturbed density model of a density dip without edge bank (κ_{dip}=1.5) is closest (within 5%) to the experimental observation.

Although an ELM is edge-localized, it has been shown that it can affect even the core channels of ECE diagnostic due to refraction effects. The signal changes on the ECE diagnostic during ELMs are consistent with an ELM causing a poloidally and radially varying density loss. The extent to which one can infer the detailed parameters of this perturbation is addressed in the following section.

Perturbed density model	Gaussian		Constant	
	Ch 5	Ch 7	Ch 5	Ch 7
Hump (κ_{hump}=1.0)	7.4	49.5	4.5	26.6
Dip (κ_{dip}=1.0)	16.0	45.2	10.7	33.5
Dip without edge bank (κ_{dip}=1.0)	41.2	44.9	32.8	39.7
(κ_{dip}=1.5)	**23.2**	**41.8**	**21.3**	**39.1**
Experiment	**Ch 5 - 25.7**		**Ch 7 - 43.6**	

Table 6.1: Signal changes of each model

6.3 Inferred dimensions

The ECE signal dips and spikes have been explained successfully on the basis of a plausible density loss model (i.e. dip without edge bank model ($\kappa_{dip} = 1.5$)) using refraction effects. Before inferring various free parameters defined in Figure 6.9, the uncertainties and limits need to be addressed.

A ray's angular deviation ($\delta\theta$) due to a density perturbation can be represented

approximately as

$$\delta\theta \propto (k_\theta \Delta r)\delta N, \tag{6.8}$$

where k_θ is a poloidal wave number, Δr radial width, and δN the refractive index change [31].

Since δN depends on δn_e, its uncertainty is dependent on the range of δn_e. The signal spikes observed on the fundamental O-mode radiometer suggest that the upper limit of the local density (n_{trough}^{ELM}) at R=0.89 m during an ELM is the corresponding cutoff density ($1.5 \times 10^{20} m^{-3}$). On the other hand, the lower limit is set by the fact that the density cannot be negative. Assuming the modeled reference density is $2.9 \times 10^{20} m^{-3}$ as shown in Figure 6.7, the δn_e is 1.4 - 2.9 $\times 10^{20} m^{-3}$ and δN for Ch 5 and Ch 7 is 0.17 - 0.31 and 0.25 - 0.41 respectively. When an ELM perturbation is assumed to be located at the midplane and its minimum density increases from 0.0 to 1.5 $\times 10^{20} m^{-3}$, the fractional electron temperature changes on the low frequency channel (Ch 7) are found to be rather insensitive, while those on the high frequency channel (Ch 5) decrease almost linearly, as shown in Figure 6.22. As will be explained later, since the elongation factor was fixed at $\kappa_{dip} = 1.5$ for these calculations, $(k_\theta \Delta r)$ is fixed as well. Thus, the angular deviation is only dependent on the δN, which is true for ELMs that are modeled as sinusoidally continuous. However, as will be discussed later, the results here are not dependent on whether a density perturbation is sinusoidally continuous. A density of $0.5 \times 10^{20} m^{-3}$ at R = 0.89 m was found to be most consistent with the experimentally observed changes on both channels.

As shown in Figure 6.16, the refracted rays of Ch 5 reach the colder regions at the resonance layer, while some rays of Ch 7 are totally reflected out of the plasma and thus contribute to no emission. Hence, as shown in Figure 6.22, the signal changes of Ch 5 show smooth density dependence, which appear to be proportional to $(\delta n_e)^2$. On the other hand, the signal changes of Ch 7 show nonlinear behavior, probably because the biggest signal decrease comes from those rays which are effectively reflected out of the plasma. However, for the most refracted rays of Ch 7 with n_{trough}^{ELM} above $1.8 \times 10^{20} m^{-3}$, initial launching angles are very critical to determine whether its

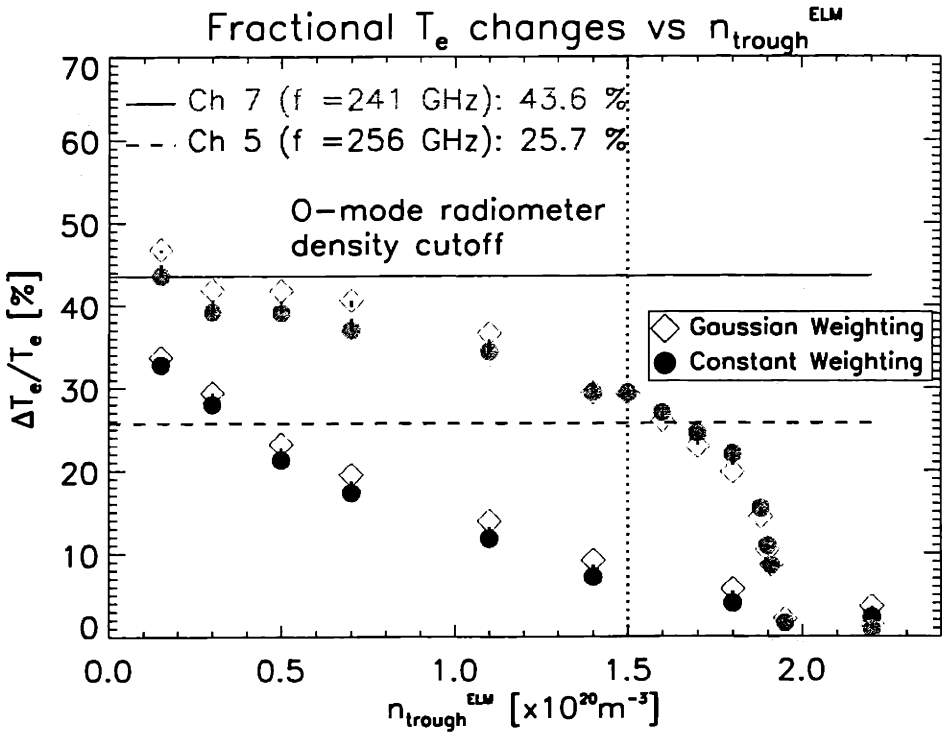

Figure 6.22: Fractional signal changes vs n_{trough}^{ELM} of a density perturbation model (dipped without edge bank case). Horizontal lines represent the experimentally observed fractional changes of Ch 5 and Ch 7 of GPC respectively. As the minimum density of an ELM model increases, the fractional T_e changes of Ch 5 decrease almost linearly but those of Ch 7 are not reduced much up to the O-mode radiometer cutoff density. On the other hand, as the n_{trough}^{ELM} increases further, the fractional changes of Ch 5 become negligible, while those of Ch 7 decrease nonlinearly down to insignificant levels. As a result, $0.5\times10^{20}m^{-3}$ was found to be the most likely local density at R = 0.89 m.

resonance layer can be reached or not. The variations between upper and lower angle cases are not insignificant. The electron temperature calculation for this plot is based on taking the middle angle for each position. This approximation is valid only when there are small variations between upper and lower angle rays. Thus, the details of the nonlinear decrease based on middle rays as shown in Figure 6.22 may be inaccurate; the essential behavior remains the same taking more rays.

Since there is negligible refraction for $n_{trough}^{ELM} \geq 2 \times 10^{20} m^{-3}$, varying modeled reference density over a range of 2.2 - 2.9 $\times 10^{20} m^{-3}$ at $R = 0.89m$ would give modest changes in signal. Since there was no edge density profile measurement in the discharge modeled, such range allows for the uncertainty of the reference density.

k_θ and Δr are coupled together to describe the poloidally elongated density loss. In other words, reducing one parameter and increasing the other by an equal amount cannot be distinguished in terms of the deviated angle ($\delta\theta$) calculated using refraction effects. Assuming δN is known and fixed (based on $n_{trough}^{ELM} = 0.5 \times 10^{20} m^{-3}$), Figures 6.23 and 6.24 illustrate schematically the ambiguity of determining the angular deviation. Suppose that Curve A represents the dip without edge bank model discussed above, with δz and δR defined in these figures. The deviated angle $(\delta\theta)_A$ at R = R1 can be determined from Equation 6.8. On the other hand, when the R and z dimensions of the perturbation are doubled as in Curve B, the deviated angle $(\delta\theta)_B$ at R = R2 will be the same as $(\delta\theta)_A$ at R = R1 because the increments in R and Z coordinates are the same (since $k_\theta \sim 1/\delta z$). Thus, the refraction effect alone cannot determine the structures without relying on other information. However, if one parameter can be estimated, the other parameter can be easily determined using the refraction effects. For example, Δr can, in principle, can be given from other edge diagnostics, such as the reflectometer. The k_θ could then be found using the refraction effects. Since no edge density profile was available for the rapidly varying ELM, a less reliable but reasonable estimate of Δr can be inferred from the O-mode radiometer. The inner channel at R=0.88 m, adjacent to the channels with signal spikes, suffered density cutoff continuously. The cutoff density of $1.7 \times 10^{20} m^{-3}$ is therefore the lower limit of the local density at $R \sim 0.88$m, which implies that Δr

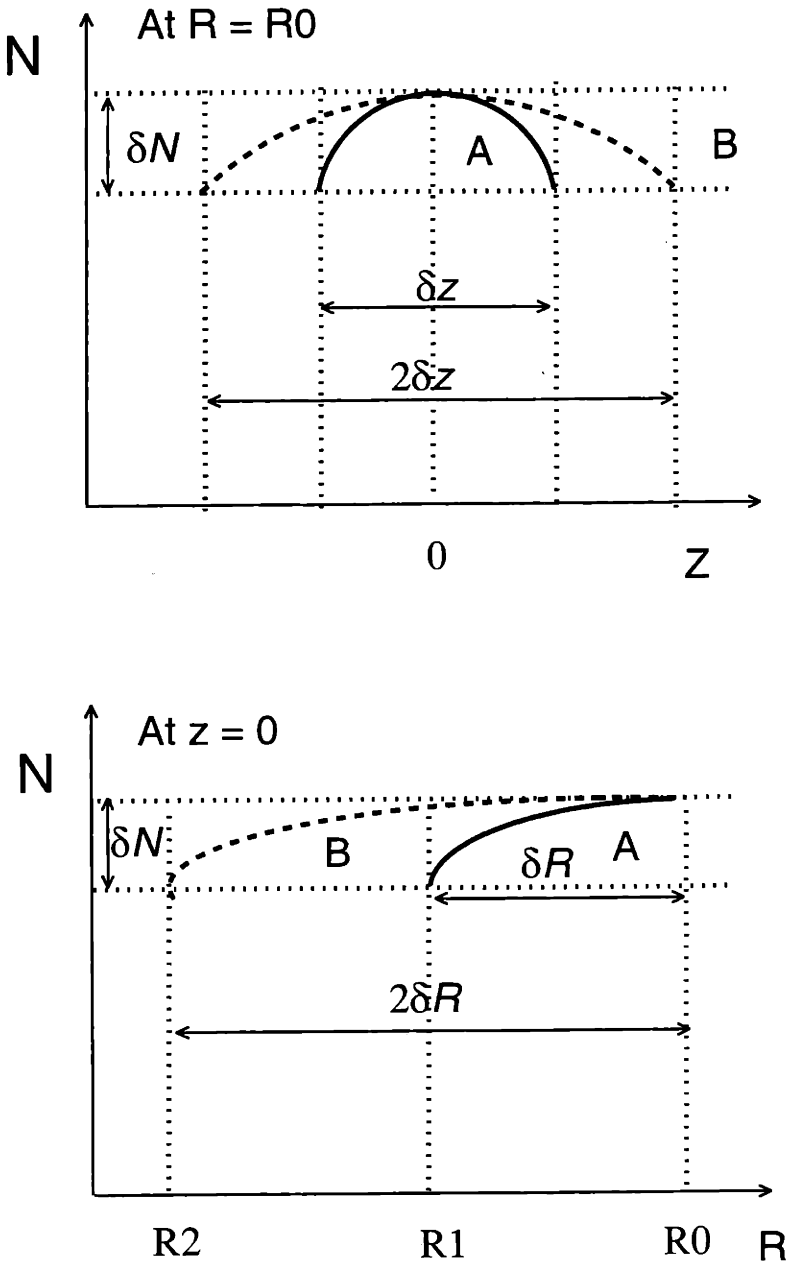

Figure 6.23: Ambiguity of refraction effects. The deviated angle at R=R1 based on a refractive index Curve A will be the same as that at R=R2 based on Curve B, as calculated in Equation 6.8.

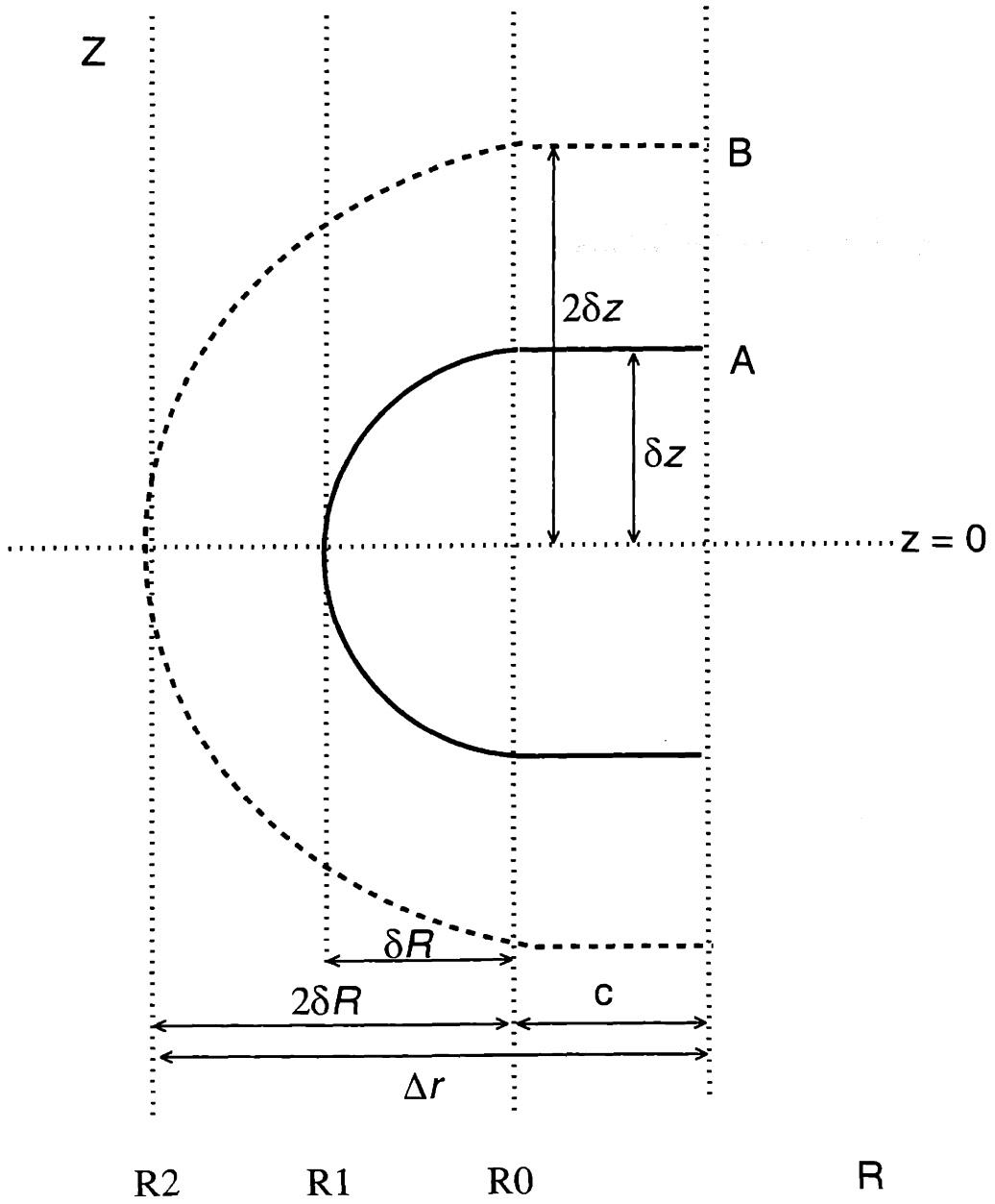

Figure 6.24: Enlarged view of the refractive index contour plot for edge parameter definitions. δz is $\kappa_{dip}\delta R$, which provides the poloidal wave number k_θ is $2\pi/\lambda_\theta = 2\pi/(2\delta R\kappa_{dip})$.

cannot be larger than 3 cm. Since the signal spikes are located 1 cm inside from the LCFS, the lower limit of Δr is 1 cm.

Assuming c=0 in Figure 6.24,

$$(k_\theta \Delta r) = \pi/\kappa_{dip} \tag{6.9}$$

where $k_\theta = 2\pi/\lambda_\theta = 2\pi/(2\delta R \kappa_{dip})$ and $\Delta r \sim \delta R$. Thus, the product of k_θ and Δr does not change as long as κ_{dip} is fixed. The sensitivity to the elongation

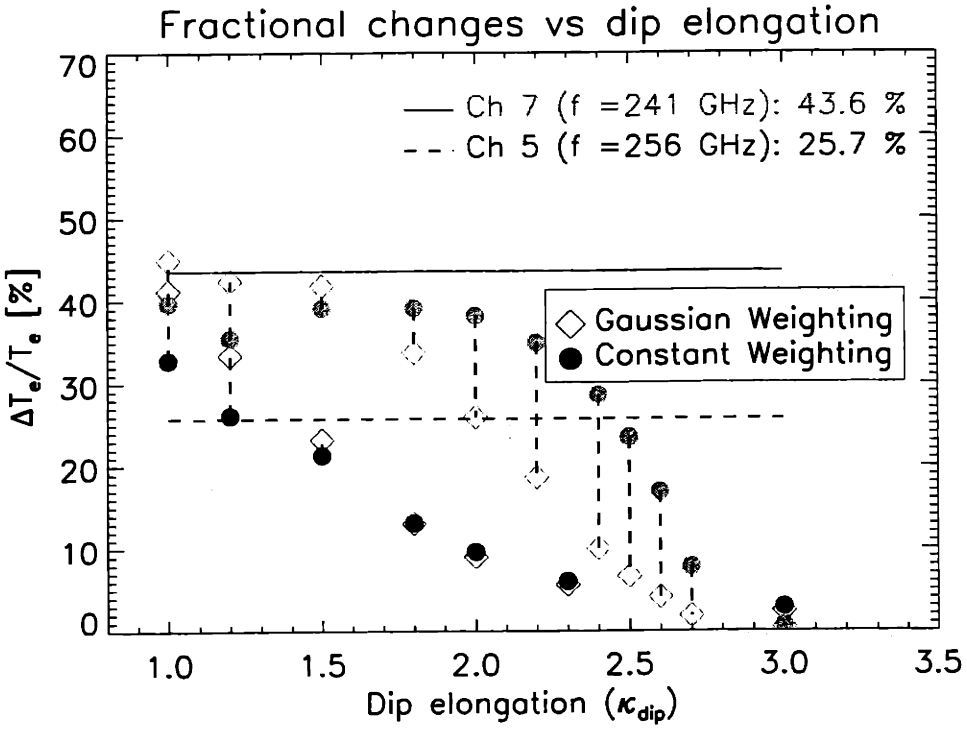

Figure 6.25: Fractional changes of T_e vs poloidal dip elongation in the dip without edge density bank model. Horizontal lines represent the experimentally observed fractional changes of Ch 5 and Ch 7 of GPC respectively. The fractional changes of Ch 5 are sensitive to the elongation, which varies linearly down to $\kappa_{dip} = 2.0$. In contrast, the changes of Ch 7 are insensitive for $\kappa_{dip} \leq 1.5$ and then drops rapidly, as κ_{dip} increases. As a result, κ_{dip}= 1.5 was found to be the closest to the experimental observations.

factor (κ_{dip}) has been studied. As shown in Figure 6.25, the elongation factor does significantly affect the refraction. As was found for varying density, the changes on Ch 7 are large and non-linear in the regime where some rays are refracted out of

the plasmas and thus contribute no emission. As the rays are refracted primarily due to poloidally varying refractive index, κ_{dip} of 1.5 is most consistent with the experimentally observed changes. However, the definition of Δr without considering non-zero c may be erroneous because the poloidal refractive index gradients in the region of width c outside the dip are critical to the deviated angle. For example, Figure 6.16, in which signal drops are consistent with experimental observations, shows δR= 1cm and c=1cm, in which Δr should be defined as δR+c=2cm, rather than δR alone. The associated poloidal wave number k_θ can be inferred as 2.1 $rad\ cm^{-1}$ because the poloidal wave length λ_θ is $\sim$ 3 cm.

A simple consistency check to see whether k_θ is reasonable or not may be made on the basis of magnetics and EFIT. As mentioned earlier, the toroidal mode number of ELM precursors was estimated to be $10 \sim 20$. Assuming ELMs are located between the q =3 and 4 rational surfaces at the edge (q_{95}=3.56 where q_{95} is the safety factor at the 95 % flux surface), the poloidal mode number would be $30 \sim 80$ (since $q = m/n$). Since the elongation from EFIT was 1.6, the circumference of the edge flux surfaces is of the order of $2\pi a\kappa \sim 2.2$ m Assuming the ELMs are equally distanced along a flux surface, the affected region for one poloidal ELM density perturbation covers about 2.8 to 7.4 cm, which can be interpreted as k_θ=$0.85 \sim 2.24$ rad cm^{-1}. Another way to get a rough estimate is to take k_θ=(m/r), where r is the minor radius. This gives the same order of magnitude, $k_\theta \sim$ 1.5 to 4.0 rad cm^{-1}, assuming r=20 cm. Both estimates indicate that the number (k_θ=2.1 rad cm^{-1}) above inferred from refraction effects is indeed reasonable. Since $(k_\theta \Delta r) \sim 4.1$ and the possible range of $\Delta r \approx 1 \sim 3cm$, k_θ may be in the range 1.4 - 4.1 rad cm^{-1}.

Keeping in mind the uncertainties and limits of refraction effects, information on free parameters can be summarized as follows.

For n_{trough}^{ELM}, the upper limit was found from the O-mode radiometer channels and the most likely local density was inferred as $\sim 0.5 \times 10^{20} m^{-3}$.

As discussed above, k_θ and Δr cannot be found separately using the density model because the signal drops of GPC reflect only line integrated density perturbation. However, assuming the $\delta n_e \sim 2.4 \times 10^{20} m^{-3}$ (associated with $n_{trough}^{ELM} = 0.5 \times 10^{20} m^{-3}$),

the elongation factor (κ_{dip}) was found to be 1.5. The Δr is 1$\sim$3 cm. This upper limit of Δr was found based on the location of the inner channel of O-mode radiometer, which is adjacent to the two channels with signal spikes but suffered density cutoff continuously, while the lower limit was inferred from the position of the channels with signal spikes. The case of Δr= 2cm predicted signal drops to be the closest to those observed for Ch 5 and 7 of GPC, while the other cases underestimated them. Within the limits of the models tried, Δr= 2cm was found to be the most likely. Geometrically, the width (b), as defined in Figure 6.9, is equivalent to the width of an affected region (Δr). At the same time, k_θ=2.1 rad cm^{-1} was found to be reasonable using refraction effects, and is in a range consistent with magnetics and EFIT. Probably, the best way to minimize possible uncertainties may be from direct measurement of Δr based on other edge diagnostics.

Although a single poloidal density perturbation was modeled consistent with the experimental observations so far, a question about whether or not it is necessary to model ELMs as sinusoidally continuous may remain. Since the aperture (3 cm) of the ECE collection optics is comparable to the poloidal wavelength, whether a poloidal wave number of the range of 2.1 rad cm^{-1} is sinusoidal or single poloidal perturbation at the midplane cannot be distinguished using the refraction effects because $k_\theta \times$(aperture size) $\sim O(1)$. In other words, it does not affect the previous results. For ($\kappa_{dip}\Delta r$) $\sim$ 3 cm, almost no change was ascertained between a single poloidal density perturbation model and sinusoidally continuous one as shown in Figure 6.1.

In addition, although the position of an ELM is likely to be in the vicinity of the locations of O-mode radiometer channels with signal spikes, the precise position is rather uncertain ($R \approx 88 \sim 90cm$). This uncertainty may also be removed by other recently installed edge diagnostics. Until then, the position, as well as the radial width (Δr), are rather uncertain.

Finally, it should be emphasized that the following inferred dimensions on the basis of the plausible model are reasonable but not unique; radial width (Δr) $\sim$ 1 to 3 cm, $\kappa_{dip} \sim 1.5$, $n_{trough}^{ELM} \sim 0.5 \times 10^{20} m^{-3}$ at the midplane 1cm inside from

the LCFS. It is for example possible that δN is up to 14 % higher or 30 % lower than assumed, in which case the inferred κ_{dip} would increase or decrease by an equal amount. The following section will show the inferred rotation angle in terms of signal time evolution.

6.3.1 Interpretation of signal changes

As shown in Figure 6.26, the precursors of Type III ELMs are observed on magnetics coherently prior to the ELM event (ie. $t < t_{ELM}$). However, in the midst of each ELM, the coherency of magnetic signals disappears, which implies that ELMs probably become stochastic. On ECE diagnostics, there is no apparent ELM precursor. However, during the ELM event, the ECE signals are observed to decrease almost linearly. Thus, two questions arise from the observation; i) why the signals on the GPC diagnostic evolve linearly and ii) what physical information can be obtained. A short answer to the first question is that the linearly decreasing signals on the GPC diagnostic are more likely to be due to a poloidally rotating density perturbation, rather than from a density loss varying in time. This is based on the following investigation. To simulate the poloidal rotation, the center position of an ELM has been specified to move up and down. As shown in Figure 6.27, as the ELM position moves poloidally away from the midplane, the fractional electron temperature changes drop almost linearly to zero for both low and high frequency channels. On the other hand, as shown in Figure 6.22, if the density were to decrease steadily in time, slowly below the level of the O-mode cutoff, the low frequency channel (Ch 7) is insensitive, while the high frequency channel (Ch 5) is linearly decreasing. This would not explain the linear change seen experimentally on both channels. As a result, the poloidally rotating density perturbation model is found to be most appropriate to explain the linearly decreasing T_e signals on all channels.

The question of physical significance may then be answered in the following way. Assuming that the rotation is purely poloidal, the rotation speed can be inferred. Considering that the poloidal length of the ECE collection optics is 3 cm and that the duration of the ELMs is $10 \sim 20$ μsec, the poloidal rotation speed can be found

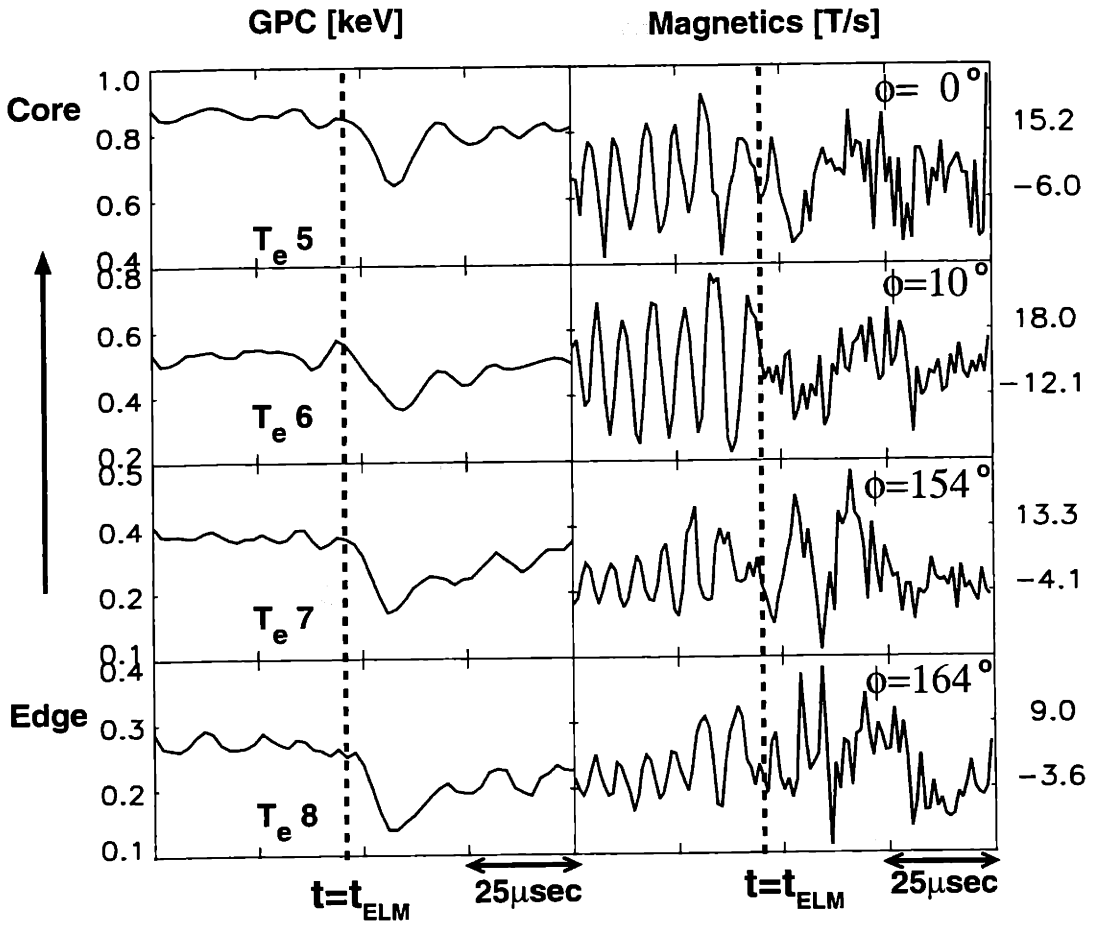

Figure 6.26: Time traces of GPC and magnetics near the ELM event. On GPC, there is no precursor, but during the ELM event, the signal drops almost linearly and recovers within 20 μsec in this case. On magnetics, there are coherent precursors at 160~200 kHz, which disappear in the midst of the ELM. The phases between toroidally adjacent coils change rapidly and the associated toroidal mode number is n~ 14.

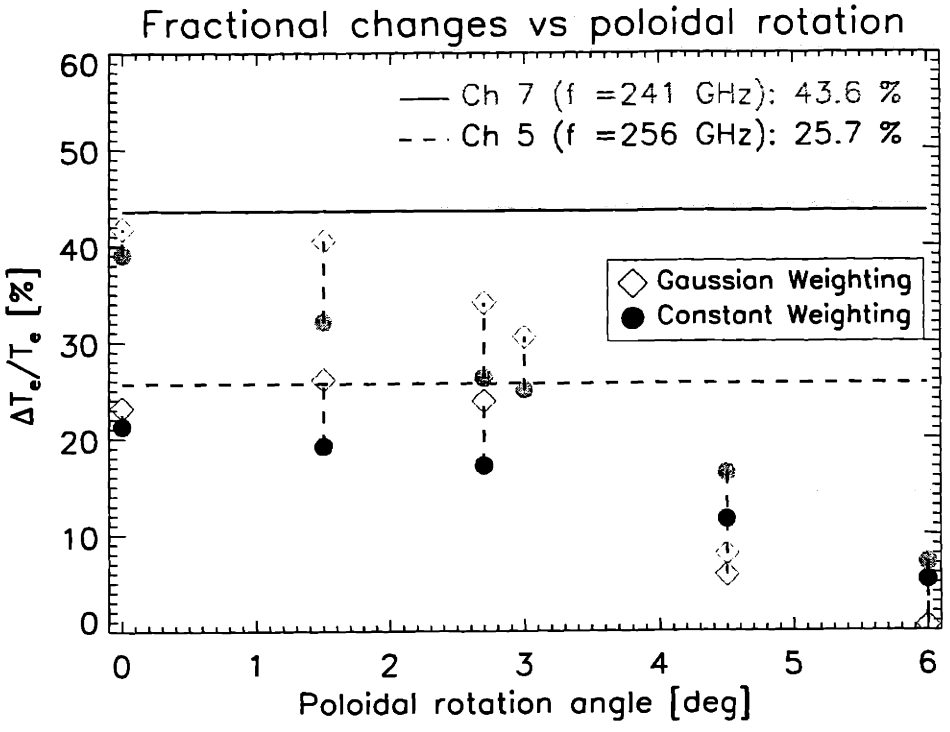

Figure 6.27: Fractional signal changes vs poloidal rotation angle of an ELM density perturbation model (dipped without edge bank case). Horizontal lines represent the experimentally observed fractional changes of Ch 5 and Ch 7 of GPC respectively. As the poloidal rotation angle increases, the signal changes of both Ch 5 and Ch 7 decrease nearly linearly. Here, the poloidal rotation angle is defined in Figure 6.9. The 6 degree is almost equivalent to 2.0 cm poloidal displacement of an ELM position.

to be 1.5~3 km/sec (=(3cm poloidal length of aperture)/(10 - 20 μsec duration)) probably in the electron diamagnetic drift direction (based on magnetic analysis). This poloidal speed is much slower than a typical edge phase velocity estimated from magnetics by a factor of 10, while it is in the same order of magnitude with the phase velocity (2~6 km/sec) inferred from phase contrast imaging (PCI). Here, the PCI diagnostic measures the line integrated density fluctuations, which are believed to be mostly from the edge region. Such discrepancy in measured edge poloidal rotation speed is an on-going issue in C-Mod.

6.3.2 Comparison with theoretical predictions

So far, there has been no definitive theoretical prediction about the ELM size. Nevertheless, some recent theoretical works imply that they can be calculated in a rather sophisticated manner. For example, Wilson [80] predicted an ELM width to be

$$\Delta r \propto \alpha_d^{-1/3} (\frac{\partial \omega^2}{\partial \alpha})^{-1/3} \frac{r}{n^{2/3}}, \tag{6.10}$$

where r is minor radius, n toroidal mode number, and $\alpha_d \equiv \frac{d\alpha}{dq}$. This radial width was predicted from Connor's formula [93], which is based on the edge ballooning theory. However, there are several caveats. First of all, their theoretical work is based on the limiter geometry, while C-Mod ELMs are observed in divertor geometry. Second, in order to calculate the theoretical width, it is necessary to run $S - \alpha$ ballooning code (eg. $\frac{\partial \omega^2}{\partial \alpha}$). Third, Type I ELMs are the main target of the theory, while Type III ELMs are studied in these C-Mod experiments. Fourth, the proportionality constant has not been determined yet. Furthermore, considering that a more likely mechanism is a combination of the ballooning mode (driven by pressure gradient) and the peeling mode (driven by current density), as discussed in Wilson's paper, this theoretical radial width will be modified accordingly. As a result, the inferred dimensions of Type III ELMs cannot be compared with any theoretical parameter yet.

6.4 Results and discussion

The radial and poloidal dimensions of n_e perturbation at Type III ELMs have been inferred on the basis of refraction effects on ECE diagnostics, combined with other available information. This indirect method to measure the ELM dimensions is a first approach to provide reasonable values. It opens the door to better understanding of the ELM physics. In particular, considering there is on-going research about ELMs, the inferred values will provide both diagnosticians and theorists with benchmark points.

Based on an edge density model, the ECE ray trajectories are found to be refracted enough to lead to reduced signals. In comparison with the experimental observations, a plausible ELM density profile was found, which allowed the author to infer the density perturbation and its geometry. Using this model, the number of the particles expelled from the main plasma can be estimated. In the cases of the analytically tractable density models (i.e. density hump and dip cases), when the second term of RHS of 6.4 is integrated with respect to $dxdy$ and the axisymmetric character of tokamak is considered (i.e. multiplied by $2\pi R$), the total number of particles draining from the main plasma can be predicted in a reasonable manner. For example, one poloidal perturbation in an ELM loses 1.6×10^{17} particles, while the total number of electron particles of the plasma is estimated to be 3.3×10^{20} (from $\bar{n_e}\times$(plasma volume)). On the other hand, the most likely ELM (density dip without bank case) cannot be integrated analytically but can be calculated numerically. Approximately 10 % additional loss is found for the most probable case in comparison with the density dip case. As mentioned above, this calculation was based on an ELM band in the toroidal direction, which may be the upper limit of the particle losses.

Since the poloidal mode number cannot be found directly from the magnetics due to the ballooning ELM characterized by the absence of the signals on the inboard magnetic pick up coils, only the toroidal mode number is known to be between 10 and 20. Assuming ELMs are located at the q =3 or 4 rational surface at the edge, the poloidal mode number may be $30 \sim 80$. Considering the ballooning character may

limit ELMs to the outboard only, their influence can be expected to be reduced by half. Thus, if the toroidal and poloidal mode numbers (m/n) associated with ELMs are considered, the total particle loss may be estimated as large as $m/2$ times the previous calculation (0.05 % of the whole particles for a single poloidal density perturbation). Therefore, the upper limit of the estimated total particle loss related to each Type III ELM is $0.7 \sim 2$ % even in the worst case. Typical repetition frequency of Type III ELMs is within a range of $1 \sim 3$ kHz, but those repetitive ELMs are observed to occur for no more than tens of milliseconds. Furthermore, considering that ELMs are observed in other tokamaks to be localized not only radially and poloidally, but also toroidally, the real impact of ELMs is expected to be much smaller than the above estimate.

Another type of phenomenon has been observed during high density (or β) plasmas on C-Mod which also causes signal drops on GPC. These ELM-like bursts were accompanied by fluctuating D_α on top of its enhanced baseline. Due to a low sampling frequency (eg. 20 kHz) and low-pass-filtering (roll-off frequency $\sim$ 15 kHz) of GPC, the signal drops might have been underestimated because the duration of such dips was no more than $20 \sim 30$ μsec. Since GPC has capability to increase the sampling frequency up to 500 kHz, this issue should be revisited later. Probably such signal drops may also be explained by refraction effects. It will be of interest to see whether they are consistent with a similar n_e perturbation to that for Type III ELMs. The developed approach based on refraction effects should be useful to address such questions in the future.

Chapter 7

Conclusions and future work

MHD activity has been analyzed primarily using ECE and magnetic diagnostics. Three key types have been examined in this thesis: resistive "multiple" tearing modes, ideal interchange modes and Type III ELMs. The first two types are summarized here together because both MHD modes were found during current ramp-up discharges. The third, Type III ELMs, has been explored in a new diagnostic approach.

The MHD activity during current ramp-up discharges was investigated in detail. Two types of MHD modes have been identified; **the resistive "multiple" tearing mode and the ideal interchange mode**. These modes were accompanied by hollow pressure and current profiles. The electron temperature fluctuations observed in experiments agreed well with the pressure fluctuations predicted in a resistive linear code (MARS). Although the resistive "multiple" tearing mode was rather benign in the case discussed here, other similar MHD fluctuations were observed to almost terminate the whole plasma. On the other hand, localized MHD fluctuations did not show any deleterious influence on the plasma in experiments. A third type of MHD activity (sawtooth-like crash) was sometimes observed, which might have been coupled with the localized MHD fluctuations. For the resistive "multiple" tearing mode, the predicted growth time ($\sim$ 0.44 msec) was in the typical range of tearing mode evolution times. For the ideal interchange mode, when kinetic effects were incorporated, the ideally unstable mode was predicted to be FLR stabilized. However,

noting that the thermal ion transit frequency was comparable to the ion diamagnetic frequency, ion Landau damping was found to act like ion viscosity and destabilize the local plasma. Such identification of a **FLR modified kinetic Mercier mode** is perhaps the first since the Mercier criterion was established in 1960.

Based on experimental observations, there was no correlation between current ramp-up rates and MHD occurrences. Instead, hollow electron temperature profile was found to give increased risk of MHD activity. When a hollow T_e profile with MHD fluctuations in the core region becomes monotonic, the associated MHD activity generally disappears. Nevertheless, many other MHD fluctuations can be observed even with monotonic T_e profile. In particular, most edge fluctuations are not affected by the core T_e peaking factor, probably because the edge T_e profile is almost always monotonic. Hollow temperature profile may, however, be a good indicator to predict core MHD activity experimentally. To get direct evidence of the hollowness of temperature (or pressure) on MHD activity, further investigation is necessary. For this purpose, q-profile measurement will be essential to eliminate the uncertainties of the q-values in the core region of a reconstructed equilibrium and separate the effects of hollow current and pressure profiles, both of which are likely correlated with $T_e(R)$. In the present C-Mod run campaign, an MSE diagnostic, which should be able to measure the q-profile, is being commissioned. Additionally, nonlinear MHD code development is desirable. For example, sawtooth-like crashes, which have not been analyzed here, are nonlinear phenomena and cannot be predicted in the theoretical frame of linear stability.

In a separate study, the geometrical dimensions of Type III ELMs have been inferred for the first time using refraction effects on ECE diagnostics. Considering that ELMs challenge present diagnostic spatiotemporal resolutions, such an indirect method will help to diagnose them more effectively. Starting from the observation of the ECE signal changes during Type III ELMs, various density perturbation models have been investigated in terms of refraction effects. To incorporate poloidal variations into the density models, a new ray tracing code, which can handle poloidal

variations, has been developed. It was shown that unusual signal dips on core ECE channels can be explained by refraction effects, using a model of the ELM density perturbation as a poloidally elongated edge density loss located just inside the LCFS, rather than density gain. As a result, the inferred geometrical dimensions are as follows; width of the affected region 1 - 3 cm, poloidal elongation $\sim$ 1.5, minimum density $0.5\times10^{20}m^{-3}$ at the midplane $\sim$ 1cm inside the LCFS. The uncertainties of the elongation factor (κ_{dip}) and local density were $\leq$ 30 %, while those of the position and the radial width were up to 50 %. Using this density model, the estimated particle loss in each poloidal perturbation at an ELM was found to be less than 0.05 % of the total particles in the main plasma. Under assumptions discussed in chapter 6, the upper limit of the total particle loss was expected to be 0.7 $\sim$ 2.0 %. Hence, this approach was found to plausibly characterize ELMs not only qualitatively but also quantitatively. Furthermore, the most probable model seems to be a poloidally rotating density perturbation. Although the inferred poloidal rotation speed (1.5 $\sim$ 3 km) is found to be slower than the phase velocity predicted from magnetics by a factor of 10, the rotation speed inferred from PCI measurements is of the same order of magnitude (2 $\sim$ 6 km/sec). The discrepancy between various diagnostics needs to be explained in future (eg. using new charge exchange recombination spectroscopy (CXRS) and beam emission spectroscopy (BES) diagnostics). The new method can also be applied in future to other types of ELMs, such as the small ELMs sometimes seen at high β in the EDA regimes, or Type I ELMs should they occur at higher power.

Bibliography

[1] J.G. Webster. *Wiley Encyclopedia of Electrical and Electronics Engineering.* John Wiley & Sons, Inc, 1999.

[2] Thomas H. Hsu. *The submillimeter wave electron cyclotron emission diagnostic for the Alcator C-Mod Tokamak.* PhD thesis, MIT, 1993.

[3] P.J. O'Shea. *Measurements of ICRF power deposition and thermal transport with an ECE grating polychromator on the Alcator C-Mod tokamak.* PhD thesis, MIT, 1997.

[4] G. Taylor et al. First measurement with a 19-channel ECE polychromator on C-Mod. In *Bull. Am. Phys. Soc.*, New Orleans, LO, November 1998. American Physical Society.

[5] J. Heard et al. Design of multichannel heterodyne electron cyclotron emission diagnostic for installation on Alcator C-Mod. In *Bull. Am. Phys. Soc.*, Pittsburgh, PA, November 1997. American Physical Society.

[6] D. Dimock et al. A compact Thomson scattering system. *Rev. Sci. Instrum.*, 2:2242, 1997.

[7] T. Luke. *Measurement of Particle Transport Coefficients on Alcator C-Mod.* PhD thesis, Massachusetts Institute of Technology, October 1994.

[8] M.E. Foord E.S. Marmar and J.L. Terry. Multichannel light detector system for visible continuum measurements on Alcator C. *Rev. Sci. Instrum.*, 53:1407, 1982.

[9] C. Christensen. *Particle transports on Alcator C-Mod tokamak.* PhD thesis, MIT, 1999.

[10] Paul C. Stek. *Reflectometry Measurements on Alcator C-Mod.* PhD thesis, MIT, 1997.

[11] Y. Lin et al. Upgrade of reflectometry profile and fluctuation measurements in Alcator C-Mod. *Rev. Sci. Instrum.*, 70:1078, 1999.

[12] B. LaBombard. Scaling and transport analysis of divertor conditions on the Alcator C-Mod tokamak. *Phys. Plasmas*, 2:2242, 1995.

[13] C. Fiore et al. *Rev. Sci. Instrum.*, 63(10):4530, 1992.

[14] J.E. Rice et al. *Rev. Sci. Instrum.*, 66:752, 1995.

[15] T.S. Petersen and R.S. Granetz. *Rev. Sci. Instrum.*, 2:2242, 1999.

[16] A. Mazurenko et al. New results from the phase contrast imaging on Alcator C-Mod. In *Bull. Am. Phys. Soc.*, volume 44, page 257, Seattle, WA, November 1999. American Physical Society.

[17] T. Taylor. *Plasma Phys. Control. Fusion*, 39:B47, 1997.

[18] C. Kessel J. Manickam G. Rewoldt and W.M. Tang. *Phys. Rev. Lett.*, 72:1212, 1994.

[19] F.M. Levinton et al. *Phys. Rev. Lett.*, 75:4417, 1995.

[20] E.J. Strait et al. *Phys. Rev. Lett.*, 75:4421, 1995.

[21] The JET Team. *Plasma Phys. Control. Fusion*, 39:B353, 1997.

[22] M. Porkolab et al. Proceedings of the 24th EPS Conf. on Contr. Fusion and Plas. Phys. volume Part II, page 569. European Physical Society, 1997.

[23] Y. In J.J. Ramos et al. n=1 resistive modes in reversed magnetic shear Alcator C-Mod plasmas (to appear in Nuclear Fusion). 2000.

[24] F. Wagner et al. *Phys. Rev. Lett.*, 53:1453, 1984.

[25] M. Greenwald et al. Multichannel light detector system for visible continuum measurements on Alcator C. *Phys. Plasmas*, 53:1407, 1998.

[26] I.H. Hutchinson et al. Proceedings of the 25th EPS Conf. on Contr. Fusion and Plas. Phys. volume Part II, page 569. European Physical Society, 1998.

[27] Y. In J.J. Ramos R.J. Hastie et al. Identification of Mercier instabilities in Alcator C-Mod plasmas (submitted to Phys. of Plasmas). 2000.

[28] F. Engelman and M. Curatolo. *Nucl. Fusion*, 13:497, 1973.

[29] M. Bornatici et al. Electron cyclotron emission and absorption in fusion plasmas. *Nucl. Fusion*, 23:1153, 1983.

[30] G. Bekefi. *Radiation Processes in Plasmas.* John Wiley & Sons, Inc, 1966.

[31] Ian H. Hutchinson. *Principles of Plasma Diagnostics.* Cambridge University Press, 1987.

[32] Thomas Howard Stix. *Waves in plasmas.* American Institute of Physics, 1992.

[33] B.A. Trubnikov and A.E. Bazhanova. *Plasma physics and the problem of controlled thermonuclear reactions*, volume 3. Pergamon Press, Oxford, UK, 1959.

[34] E. Hecht. *Optics.* Addison-Wesley, Menlo Park, CA, 1987.

[35] J.W. Connor and Liu Chen. *Phys. Fluids*, 28:2201, 1985.

[36] Jeffrey P. Freidberg. *Ideal Magnetohydrodynamics.* Plenum Press, 1987.

[37] S.I. Braginskii. Transport processes in a plasma. In M.A. Leontovich, editor, *Reviews of Plasma Physics*, page 205. Consultants Bureau, New York, 1965.

[38] L.L.Lao et al. *Nucl. Fusion*, 30:1035, 1990.

[39] P.H. Rutherford. Nonlinear growth of the tearing mode. *Phys. Fluids*, 16:1903, 1973.

[40] H.P. Furth P.H. Rutherford and H. Selberg. *Phys. Fluids*, 16:1054, 1973.

[41] M.N. Bussac et al. *Phys. Rev. Lett.*, 35:1638, 1975.

[42] Dieter Biskamp. *Nonlinear Magnetohydrodynamics.* Cambridge University Press, 1993.

[43] John Wesson. *Tokamaks 2nd Ed.* Oxford University Press, 1997.

[44] G. Bateman. *MHD instabilities.* MIT Press, 1978.

[45] A.H. Glasser J.M. Greene and J.L. Johnson. *Phys. Fluids*, 19:567, 1976.

[46] Sergio Ortolani and Dalton D. Schnack. *Magnetohydrodynamics of Plasma Relaxation.* World Scientific, 1993.

[47] M.S. Chu et al. *Phys. Rev. Lett.*, 77:2710, 1996.

[48] C.G. Gimblett and R.J. Hastie. Model of the sawtooth cycle. Technical report, UKAEA, 1994. AEA FUS 264.

[49] J.M. Greene and M.S. Chance. *Nucl. Fusion*, 21:453, 1981.

[50] A.D. Turnbull et al. *Phys. Rev. Lett.*, 74:718, 1995.

[51] R.J. LaHaye and R.J. Sauter. *Nucl. Fusion*, 38:987, 1998.

[52] R.B. White D.A. Monticello M.N. Rosenbluth and B.V. Waddell. In *Plasma Physics and Controlled Fusion Research*, volume 1, page 569. IAEA, 1977.

[53] B. Carreras H.R. Hicks and B.V. Waddell. *Nucl. Fusion*, 19:583, 1979.

[54] P.L. Pritchett Y.C. Lee and J.F. Drake. *Phys. Fluids*, 23:1368, 1980.

[55] Z. Chang et al. *Phys. Rev. Lett.*, 77:3553, 1996.

[56] S. Günter et al. *Nucl. Fusion, special issue*, 39:1793, 1999.

[57] A. Bondeson G. Vlad and H. Lütjens. *Phys. Fluids B*, 4:1889, 1992.

[58] C. Mercier. *Nucl. Fusion*, 1:47, 1960.

[59] J.N. Talmadge and W.A. Cooper. *Phys. Plasmas*, 3:3713, 1996.

[60] K. Ichiguchi. *Plasma Phys. Control. Fusion*, 39:1805, 1997.

[61] T. Ozeki M. Azumi S. Ishida and T. Fujita. *Plasma Phys. Control. Fusion*, 40:871, 1998.

[62] M.S. Chance C. Kessel and S.C. Jardin. *Plasma Phys. Control. Fusion*, 41:1379, 1999.

[63] T. Ozeki M. Azumi S. Ishida and T. Fujita. *Plasma Phys. Control. Fusion*, 41:1429, 1999.

[64] K.V. Roberts and J.B. Taylor. *Phys. Rev. Lett.*, 8:197, 1962.

[65] G. Ara B. Basu and B. Coppi. *Annals of Phys.*, 112:443, 1978.

[66] J.W. Connor W.M. Tang and L. Allen. *Nucl. Fusion*, 24:1023, 1984.

[67] W.M. Tang R.L. Dewar and J. Manickam. *Nucl. Fusion*, 22:1079, 1982.

[68] R.J. Hastie. private communication, 2000.

[69] C. Wahlberg. *Journal of Plas. Phys.*, 62:165, 1999.

[70] M.N. Rosenbluth N.A. Krall and N. Rostoker. *Nucl. Fusion Suppl.*, 1:143, 1962.

[71] F. Porcelli and S. Migliuolo. *Phys. Fluids*, 29:1741, 1986.

[72] V.P. Lakhin and A.B. Mikhailovskii. *Phys. Letts A.*, 191:162, 1994.

[73] A.B. Mikhailovskii S.V. Nazarenko and A.P. Churikov. *Sov. J. Plasma Physics*, 15:19, 1989.

[74] F. Romanelli L. Chen and R.B. White. *Nucl. Fusion*, 31:631, 1991.

[75] F. Zonca L. Chen and R.A. Santoro. *Plasma Phys. Control. Fusion*, 38:2011, 1996.

[76] J.E. Rice et al. *Nucl. Fusion*, 37:421, 1997.

[77] Y. B. Kim P. H. Diamond and R. J. Groebner. *Phys. Fluids B*, 3:2050, 1991.

[78] J.W. Connor. A review of models for ELMs. *Plasma Phys. Control. Fusion*, 40:191, 1998.

[79] H. Zohm. Edge localized modes (ELMs). *Plasma Phys. Control. Fusion*, 38:105, 1996.

[80] H.R. Wilson et al. Ideal magnetohydrodynamic stability of the tokamak high-confinement mode edge region. *Phys. Plasmas*, 6:1925, 1999.

[81] Y. Kamada et al. Growth of the edge pedestal in JT-60U ELMy H-mode. *Plasma Phys. Control. Fusion*, 41:1371, 1999.

[82] P. Breger et al. Plasma-edge gradients in L-mode and ELM-free H-mode JET plasmas. *Plasma Phys. Control. Fusion*, 40:347, 1998.

[83] R.J. Groebner and T.H. Osborne. Scaling studies of the high mode pedestal. *Phys. Plasmas*, 5:1800, 1998.

[84] W. Suttrop et al. Proceedings of the 26th EPS Conf. on Contr. Fusion and Plas. Phys. volume 23J, page 1405. European Physical Society, 1999.

[85] A.E. Hubbard et al. Measurement of the high confinement mode pedestal region on Alcator C-Mod. *Phys. Plasmas*, 5:1744, 1998.

[86] W. Suttrop et al. Characteristics of edge localized modes in ASDEX upgrade. *Plasma Phys. Control. Fusion*, 38:1407, 1996.

[87] Y. In et al. Core MHD activity and ELMy bursts observed on ECE diagnostics. In *Bull. Am. Phys. Soc.*, volume 43, page 1820, New Orleans, LO, November 1998. American Physical Society.

[88] D.B. Batchelor R.C. Goldfinger and H. Weitzner. Ray tracing near the electron cyclotron frequency with application to EBT. *IEEE Transactions on Plasma Science*, PS-8:78, 1980.

[89] T. Ozeki et al. Plasma shaping, edge ballooning stability and ELM behavior in DIII-D. *Nucl. Fusion*, 30:1425, 1990.

[90] A.E. Hubbard. private communication, 2000.

[91] M. Greenwald. private communication, 2000.

[92] Donald Barnhart. *Optica.* Wolfram Research Inc., 1995.

[93] J.W. Connor R.J. Hastie H.R. Wilson and R.L. Miller. Magnetohydrodynamic stability of tokamak edge plasmas. *Phys. Plasmas*, 5:2687, 1998.